Collected figures from HELIOPHYSICS I.
PLASMA PHYSICS OF THE LOCAL COSMOS

edited by
CAROLUS J. SCHRIJVER
Lockheed Martin Advanced Technology Center
and
GEORGE L. SISCOE
Boston University

This document contains the figures from the published volume of Helio-physics I as submitted to Cambridge University Press, prior to possible revisions in the graphics and captions during the copy editing process. This collection is intended only as an aid to students and teachers for use in, e.g., lectures and study sessions.

Contents

1
Prologue

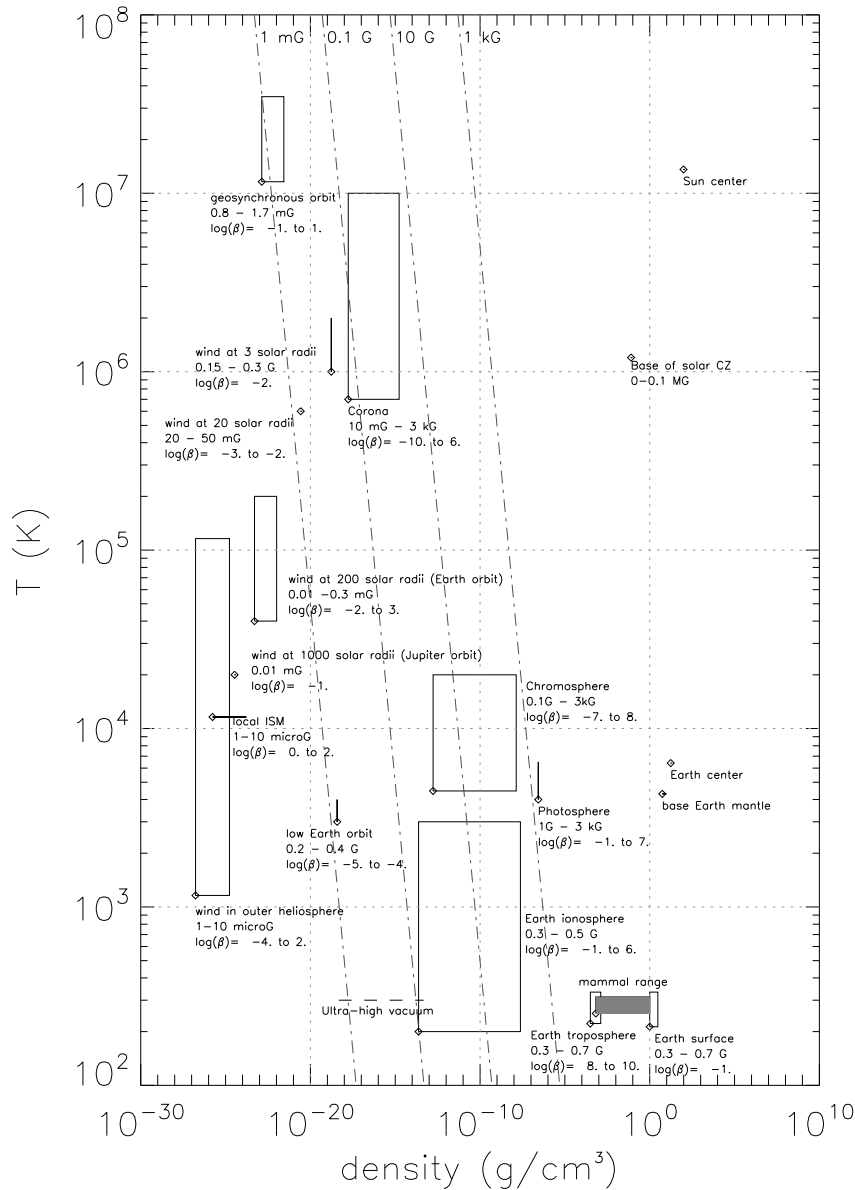*by Carolus J. Schrijver and George L. Siscoe*

Fig. 1.1. Temperature versus density for a variety of conditions within the local cos-
mos. Some typical ranges are indicated, and labeled with magnetic field strengths
(in Gauss) found in that domain, followed by estimated ranges of the plasma β,
i.e., the ratio of energy density in plasma over that in the magnetic field (Eq. 3.11).
This is but one of many diagrams that can be made to characterize the multidi-
mensional world of heliophysics; we could have made other figures that compare
collision rates, ionization states, scales of time, length, or velocity, but this one is
closest to our intuitive knowledge of the world around us. The reader is encouraged
to experiment with these other diagrams using numbers found throughout the three
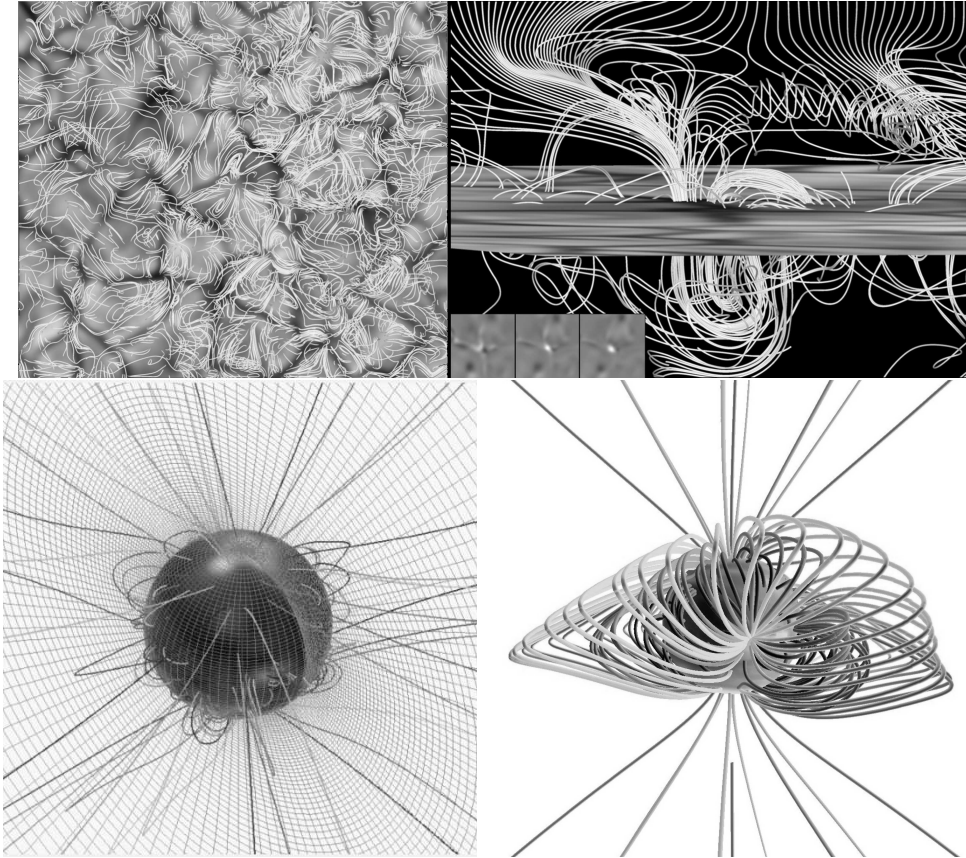Volumes of this series.

Fig. 1.2. Illustration of the multitude of scales in the solar magnetic field. The top panel shows a model computation of the magnetic field (by Abbett, 2007; see also Fig. 8.10) on the scale of the dominant convective motions at the solar surface, the 1000-km scale of the granulation (see also Fig. 8.2); the left panel is a top view of the solar surface with sample magnetic field lines (see Sect. 4.1) overplotted, while the right panel shows a vertical cut through one of the convection cells to illustrated how the field in this model threads the surface sometimes multiple times, evolving on a time scale of a few minutes. The lower two panels (from the Center for Integrated Space Weather Modeling) show models of the global solar field, tracing field lines up to the cusps of the streamers that outline the topologically distinct regions of closed field and the field that is open to the heliosphere; this global scale field evolves on time scales of months to a decade (see Chs. 4 and 9).
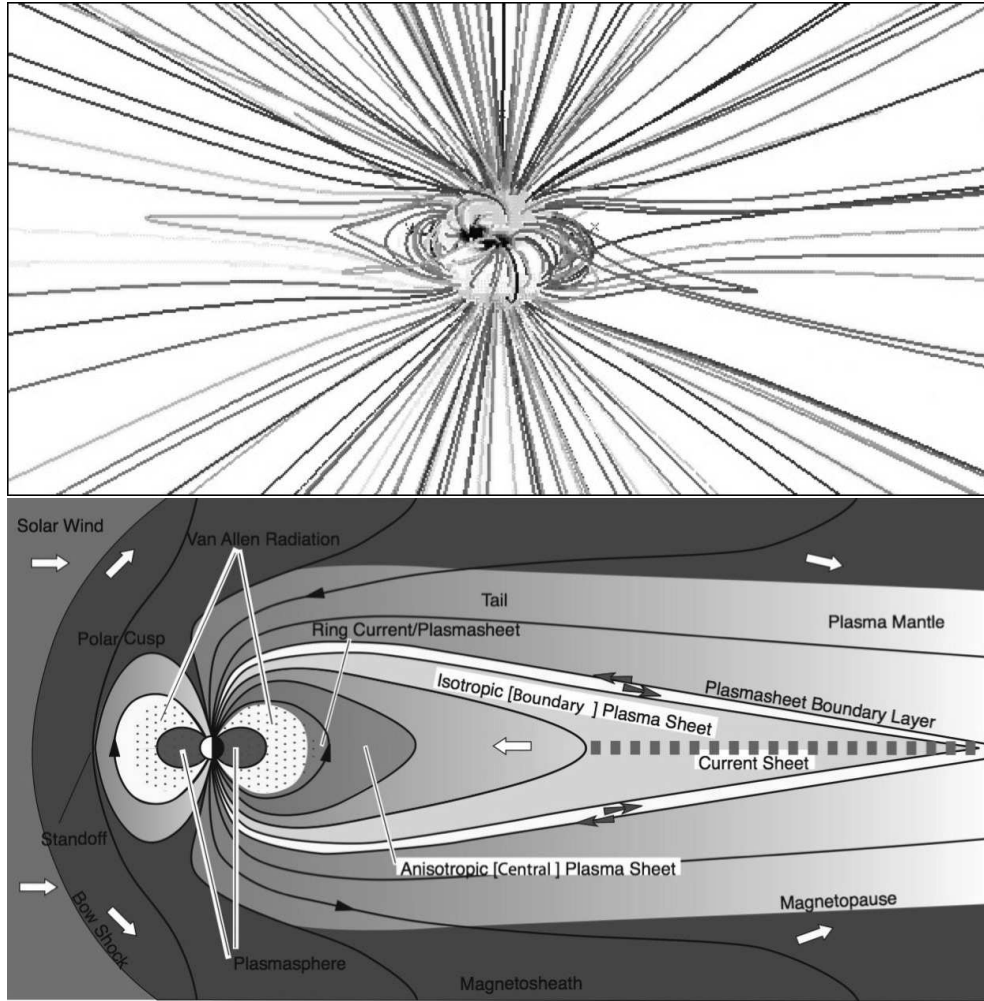
Fig. 1.3. *Top:* Magnetohydrodynamic model computation of a simplified solar magnetic field reaching into the heliosphere. The large-scale dipolar field of the Sun is blown open by the solar wind (Ch. 8), stretching out the relatively strong, closed field of the activity belt into "streamers" with cusps that lie at the base of the heliospheric current sheet. (Figure courtesy of P. Riley, SAIC) The stretching of magnetic field arcades into a cusp-and-sheet structure is one of the common features in space plasmas (compare, for example, Figs. 2.7, 5.1, 6.3, 10.1, and the bottom panel here). *Bottom:* Schematic illustration of the Earth's magnetic field and magnetospheric features. Earth provides the prototype magnetosphere produced by the interaction of the solar wind with the planet's internally-generated magnetic field. The boundary of the region dominated by the planet's magnetic field is the magnetopause. The supersonic solar wind is sharply slowed and deflected at the bow shock, flowing around the planet in a magnetosheath boundary layer. The solar wind pulls the magnetosphere back behind the planet into a long magnetotail with a current sheet and cusp structures. (Figure courtesy of T. W. Hill, Rice University)
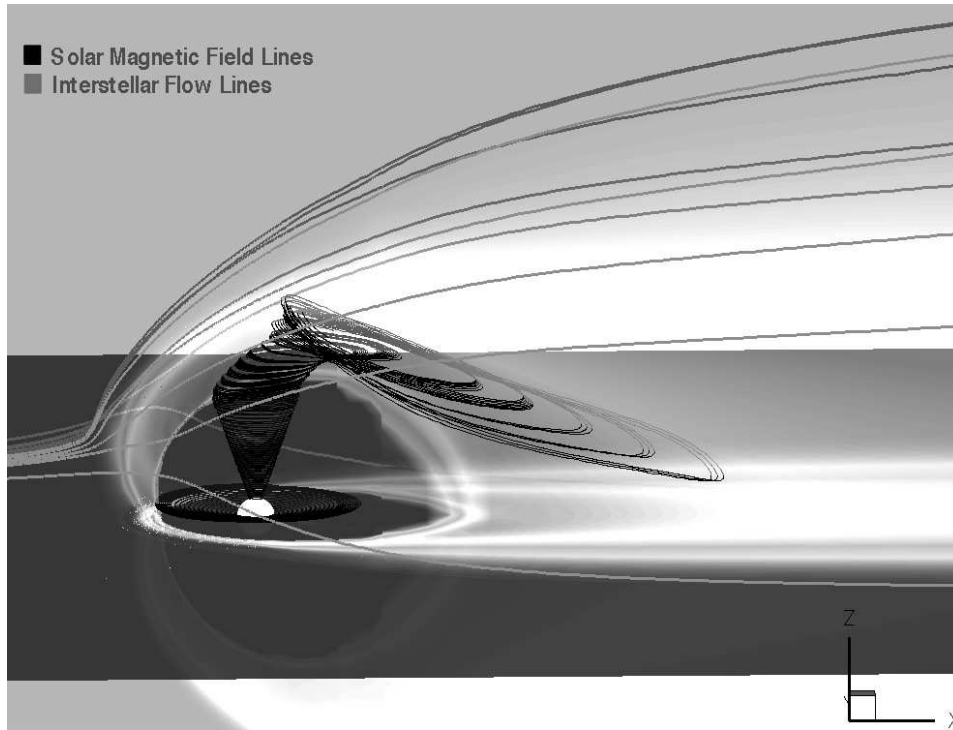
Fig. 1.4. Illustration of the heliospheric cavity in the interstellar medium. The interstellar medium (ISM) flows around the heliopause forming a cavity (or 'cell' - cf., Sect. 6.7) similar to that around the planets in the solar wind. Here, however, the ram pressure of the ISM is balanced largely by that of the solar wind, which carries the heliospheric magnetic field with it. A few sample field lines (black) show that the solar rotation underneath the outflowing wind leads to a tightly wound spiral field (with polar outflows blown into the heliospheric tail by the interaction with the ISM). (Figure courtesy of M. Opher, George Mason University)

2
Introduction to heliophysics
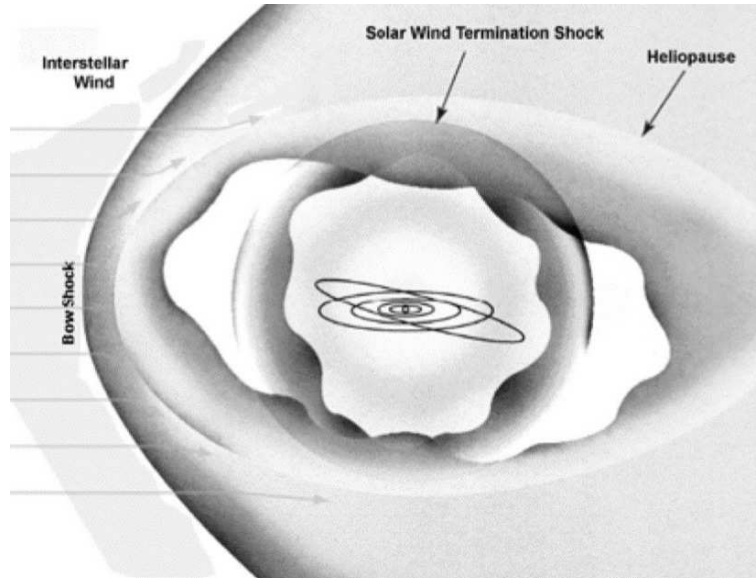
by Thomas J. Bogdan

Fig. 2.1. The heliosphere is the sphere of influence carved out by the Sun in the surrounding interstellar medium. The solar wind flows out incessantly in all directions, past the orbiting planets, and is finally halted at the termination shock (the innermost nested surface). The shocked solar wind material diffuses outward into the surrounding material forming the heliopause (the prolate spheroid that encloses the spherical termination shock). The Sun and the heliosphere have a peculiar motion with respect to the background interstellar medium pointing from right to left in this figure. This velocity is larger than the characteristic propagation speeds of waves supported by the interstellar medium and consequently a parabolic-shaped bow shock (the outer nested surface) forms around one side of the heliopause.
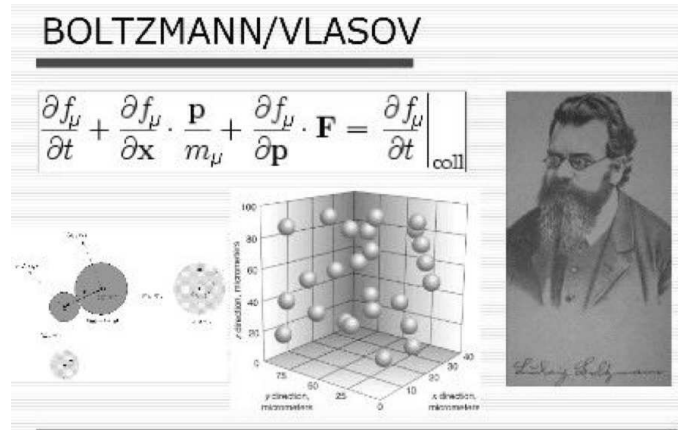
Fig. 2.2. The Boltzmann equation describes the evolution of the phase space density f, for particles of type μ, and mass m_μ, in the presence of a force-field $\mathbf{F}$. The independent variables are the time t, the location $\mathbf{x}$, and the momentum $\mathbf{p}$. When binary collisions between particles are ignorable, the collision term to the right of the equal sign can be dropped. The collisionless Boltzmann equation is often referred to as the Vlasov equation.
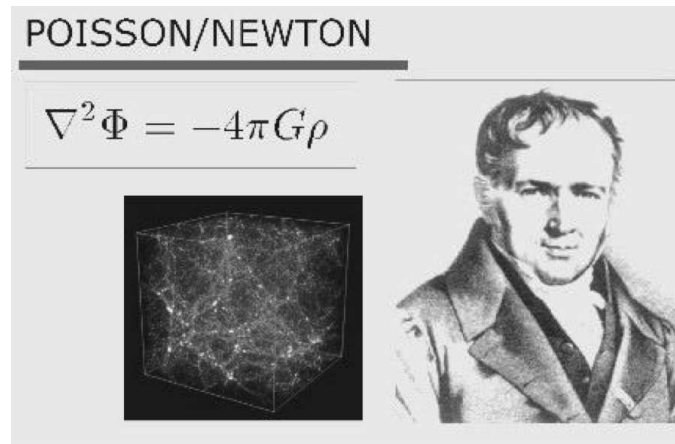
Fig. 2.3. Poisson's equation determines the gravitational potential Φ, in terms of the mass distribution prescribed by the density ρ. G denotes Newton's gravitational constant.

MAXWELL/FARADAY

MKS units	Gaussian units	
$\nabla \cdot \mathbf{D} = \rho$	$\nabla \cdot \mathbf{D} = 4\pi\rho$	
$\nabla \cdot \mathbf{B} = 0$	$\nabla \cdot \mathbf{B} = 0$	
$\nabla \times \mathbf{H} = \mathbf{J} + \frac{\partial \mathbf{D}}{\partial t}$	$\nabla \times \mathbf{H} = \frac{4\pi}{c}\mathbf{J} + \frac{1}{c}\frac{\partial \mathbf{D}}{\partial t}$	
$\nabla \times \mathbf{E} = -\frac{\partial \mathbf{B}}{\partial t}$	$\nabla \times \mathbf{E} = -\frac{1}{c}\frac{\partial \mathbf{B}}{\partial t}$	
$\mathbf{F} = q(\mathbf{E} + \mathbf{v} \times \mathbf{B})$	$\mathbf{F} = q\left(\mathbf{E} + \frac{1}{c}\mathbf{v} \times \mathbf{B}\right)$	Lorentz force law
$\mathbf{D} = \epsilon_0 \mathbf{E} + \mathbf{P}$	$\mathbf{D} = \mathbf{E} + 4\pi\mathbf{P}$	(general)
$\mathbf{D} = \epsilon_0 \mathbf{E}$	$\mathbf{D} = \mathbf{E}$	(free space)
$\mathbf{D} = \epsilon\mathbf{E}$	$\mathbf{D} = x\mathbf{E}$	(isotropic linear dielectric)
$\mathbf{B} = \mu_0(\mathbf{H} + \mathbf{M})$	$\mathbf{B} = \mathbf{H} + 4\pi\mathbf{M}$	(general)
$\mathbf{B} = \mu_0\mathbf{H}$	$\mathbf{B} = \mathbf{H}$	(free space)
$\mathbf{B} = \mu\mathbf{H}$	$\mathbf{B} = \mu\mathbf{H}$	(isotropic linear magnetic medium)

Maxwell's Equations Karaoke DVD

Produced and Performed by Lynda Williams
www.scienceswomen.com

Fig. 2.4. Maxwell's equations determine the electromagnetic fields **E** and **B** in terms of the electric current density **J**, and the charge density ρ. The two scalar equations were deduced by Gauss and Poisson. The induction equation (containing the curl of **E**) is associated with the contributions of Faraday. Maxwell's breakthrough was to append the displacement current to the right side of Ampere's Law, thereby accounting for electromagnetic radiation.

IDEAL MAGNETOHYDRODYNAMICS

$$\frac{\partial \rho}{\partial t} + \mathbf{\nabla} \cdot (\rho \boldsymbol{u}) = 0 \,,$$

$$\frac{\partial S}{\partial t} + \boldsymbol{u} \cdot \mathbf{\nabla} S = 0 \,,$$

$$\frac{\partial \boldsymbol{B}}{\partial t} - \mathbf{\nabla} \times (\boldsymbol{u} \times \boldsymbol{B}) = 0 \,,$$

$$\frac{\partial \boldsymbol{u}}{\partial t} + (\boldsymbol{u} \cdot \mathbf{\nabla})\boldsymbol{u} + \frac{1}{\rho}\nabla p = \frac{1}{4\pi\rho}(\mathbf{\nabla} \times \boldsymbol{B}) \times \boldsymbol{B} - g\hat{\boldsymbol{z}} \,,$$

$$e = \frac{1}{\gamma - 1}\frac{p}{\rho}, \quad S = c_v \log\left(p/\rho^\gamma\right) \,,$$

Fig. 2.5. Ideal magnetohydrodynamics (MHD) provides the simplest possible description of a heliophysical plasma. This closed system of equations may be derived directly from the kinetic equation of Boltzmann and the electromagnetic field equations of Maxwell under certain limiting assumptions that are often realized in many situations of interest present in the Sun-Earth system. The principal architects and expositors of MHD are Alfvén, Grad, Parker, Chandrasekhar, and Dungey.
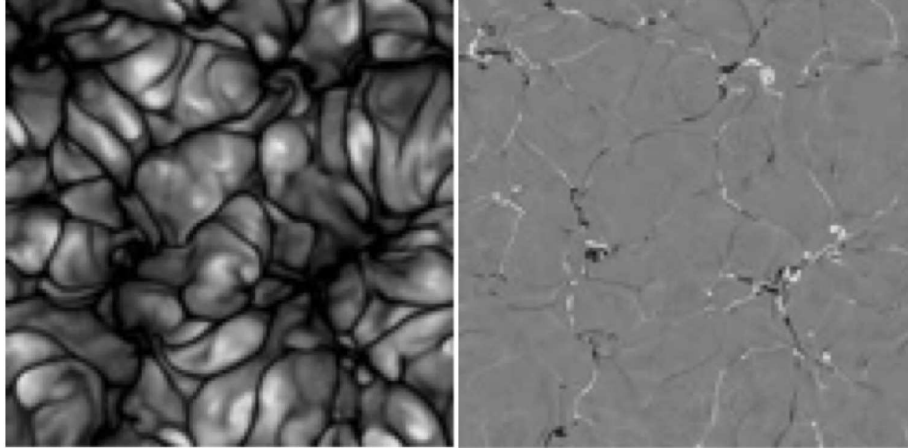
Fig. 2.6. Magnetic fields are carried about by fluid motions in highly conducting plasmas. Accordingly they accumulate where flows converge and are swept out of regions of diverging flow. The two panels of this figure illustrate this behavior for a numerical simulation of magneto-convection. In panel (a) we observe the vertical component of the flow close to the surface of the simulation. Lighter hues represent upwelling fluid and darker tones correspond to downflows. The network of downflows is fed by horizontal diverging flows (not seen in this image) associated with the upwellings that converge abruptly at the dark downflow lanes. In panel (b) we see the vertical component of the magnetic field at the same instant of time. Light hues denote positive polarity magnetic field and dark tones outline regions of opposite negative polarity. We see clearly that the magnetic field predominantly lives in the downflow network. Some vertical magnetic flux that has just emerged can be seen in a few of the granular upwellings; it will subsequently be swept to the network to join the remainder of the magnetic field. (See also Fig. 1.2)
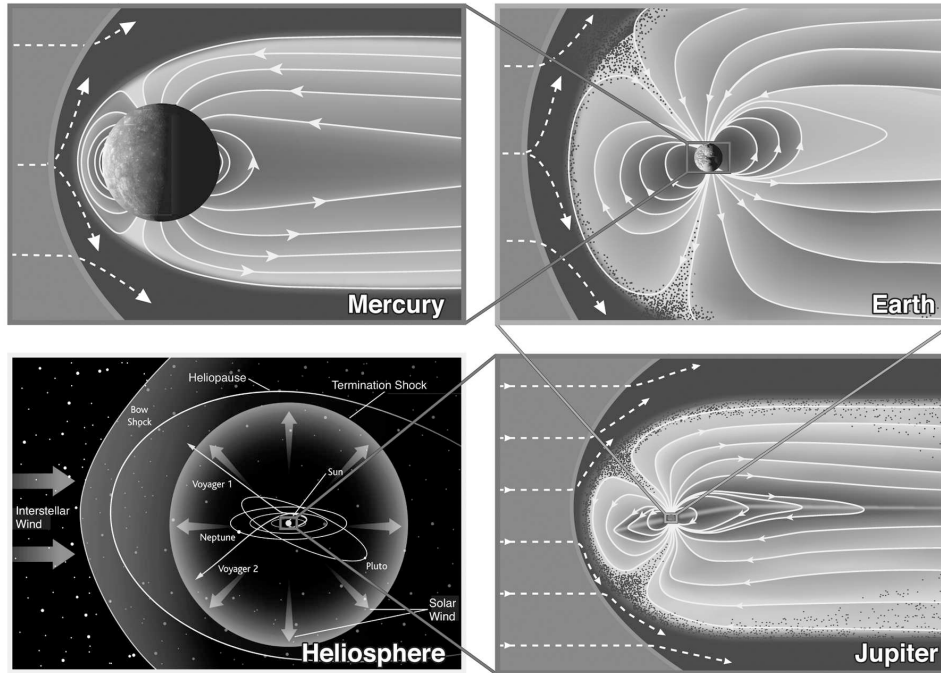
Fig. 2.7. Magnetospheres surround all planets with sensible magnetic fields. They are constantly stressed and sheared by the incoming solar wind and by the rotation of their planets. In some cases, even the satellites that orbit the planets can impact magnetospheric dynamics. All magnetospheres are enveloped in bow shocks that serve to slow and deflect the solar wind around the magnetosphere. A particularly fascinating aspect of magnetospheres is how they adapt and change their connectivity to the magnetic fields entrained in the solar wind. The first three panels of this figure (clockwise) nicely illustrate both the similarities and differences between three planetary magnetospheres of Mercury, Earth, and Jupiter. The final panel shows the entire heliosphere, a magnetosphere in its own right. The relative scales of the panels are indicated by the gray lines that connect one panel to an appropriately scaled outline of it in its neighboring panel.
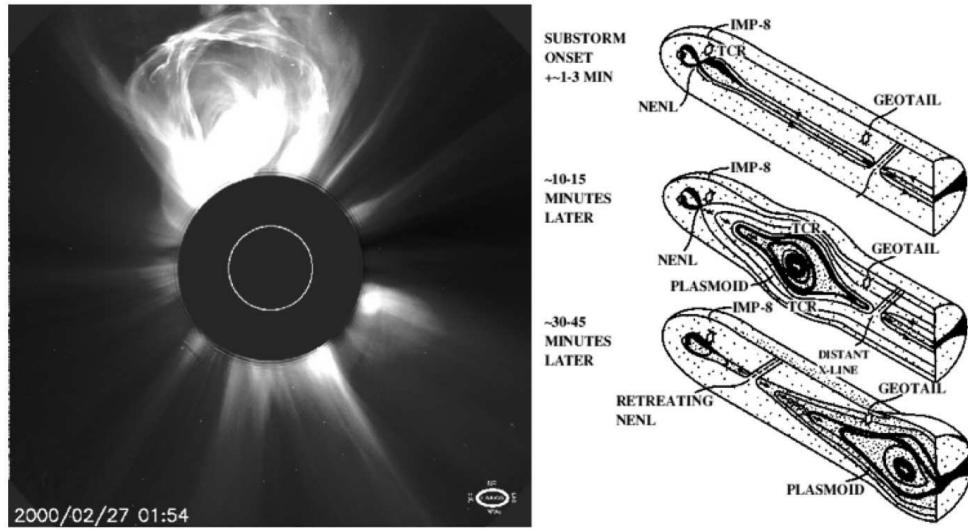
Fig. 2.8. Two examples of the explosive release of energy, mass, momentum, and magnetic field from (left) the solar corona and (right) the Earth's magnetosphere.
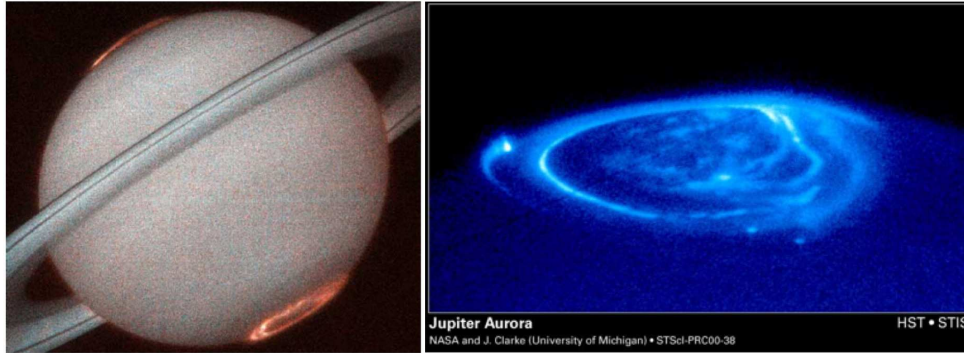
Fig. 2.9. Aurorae occur near the magnetic polar caps of planets. They result from the precipitation of energetic particles, usually electrons, along the conduits formed by the dipolar magnetic field lines. The magnetic field lines that emanate from the polar caps often change their connectivity between the planetary field anchored at the opposite antipode and the magnetic fields carried by the solar wind. Rotation and the orientation of the solar wind magnetic field often determine when topological changes in connectivity are required. Reconnection and current sheets are the agents responsible for these changes and they are also implicated in the acceleration of particles that give rise to the aurora in the ionosphere and thermosphere. The figure compares two similar but certainly distinct aurorae around (left) Saturn and (right) Jupiter (see Ch. 13; the association of the features in Jupiter's aurora with its magnetic field and satellites is shown in Fig. 13.7).

3

Creation and destruction of magnetic field
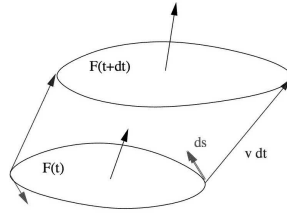
by Matthias Rempel

Fig. 3.1. The closed line $\mathrm{d}F$ is moving with the fluid ('frozen into the fluid'). The area elements $-\int_{F(t)} d\vec{f}$, $\int_{\mathrm{d}F} d\vec{s} \times \vec{v}\Delta t$ and $\int_{F(t+\Delta t)} d\vec{f}$ form a closed surface.
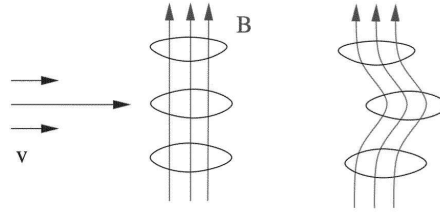
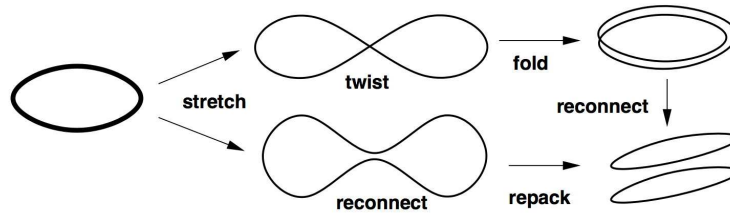Fig. 3.2. Shearing of a flux tube by a velocity field in ideal MHD

Fig. 3.3. Illustration of two possible flux-rope dynamos. In both cases the field amplification takes place during the stretch operation. The twist-fold (top) and reconnect-repack (bottom) steps are required to remap the amplified flux-rope into the original volume element so that the process can be repeated. Magnetic diffusivity is essential to allow for the topology change required to close the cycle. Each cycle increases the field strength by a factor of 2.
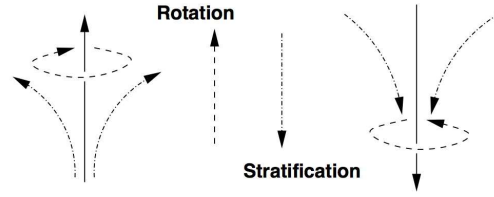
Fig. 3.4. Mean helicity as consequence of stratification and rotation. The stratification leads to a correlation between the horizontal divergence and the vertical velocity. The influence of the Coriolis-force on the horizontal flows causes a mean kinetic helicity.
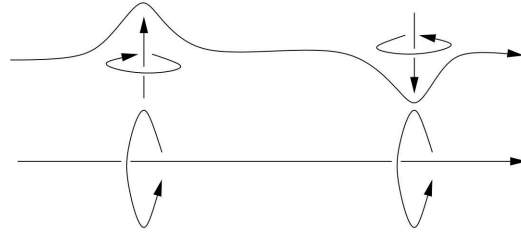
Fig. 3.5. Relation between kinetic helicity and α-effect. The assumed negative kinetic helicity (left hand screw) induces a poloidal field with a current parallel to the toroidal field, leading to a positive α-effect. A net helicity is required to have up- and downward motions contributing the same way.
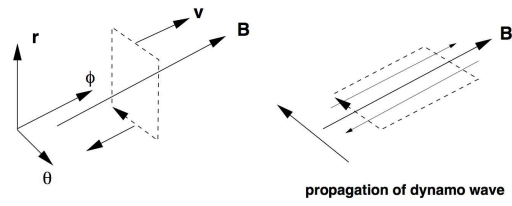
Fig. 3.6. Illustration of dynamo waves in an $\alpha\Omega$-dynamo. The poloidal field (dashed) produced by the α-effect is sheared by the velocity field. The resulting 'new' toroidal field amplifies the original toroidal field on the poleward side and weakens it on the equator ward side. As a result the toroidal field pattern moves poleward in the $-\theta$ direction.

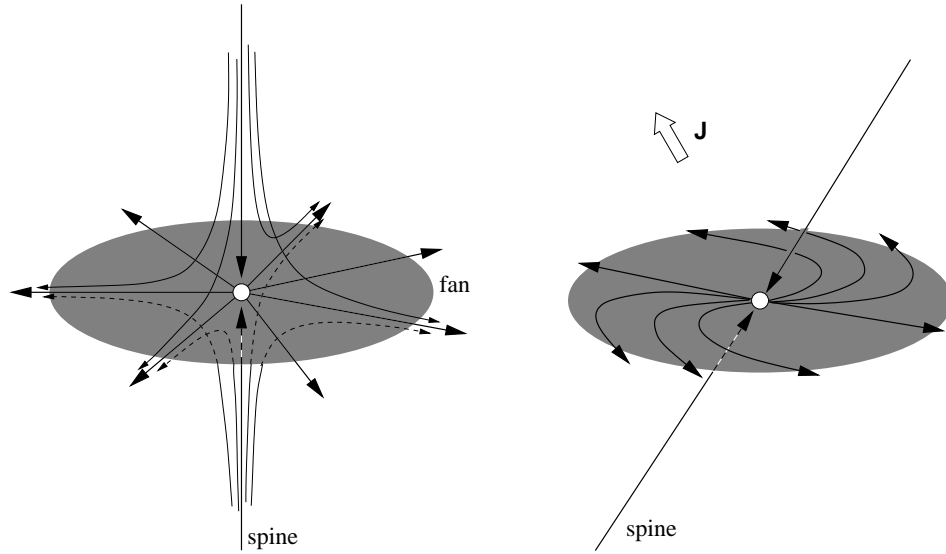# 4

Magnetic field topology

by Dana W. Longcope

Fig. 4.1. Schematic depictions of positive null points. Two *spine field lines* directed toward the *null point* (white circle) appear as dark lines with arrow heads next to the null. The central portion of the horizontal *fan surface* is colored grey, and contains fan field lines directed outward like spokes on a wheel. The left case is the simplest: a potential null point which is cylindrically symmetric (with two identical, real eigenvalues, $\lambda_2 = \lambda_3$). Thinner lines show a few of the field lines on either side of the fan surface. The right case is a non-potential null whose spines are not orthogonal to the fan surface. This is based on a non-force-free case from Parnell *et al.* (1996) with current (white arrow) at an angle to the spine. [Reproduced from Longcope 2005.]
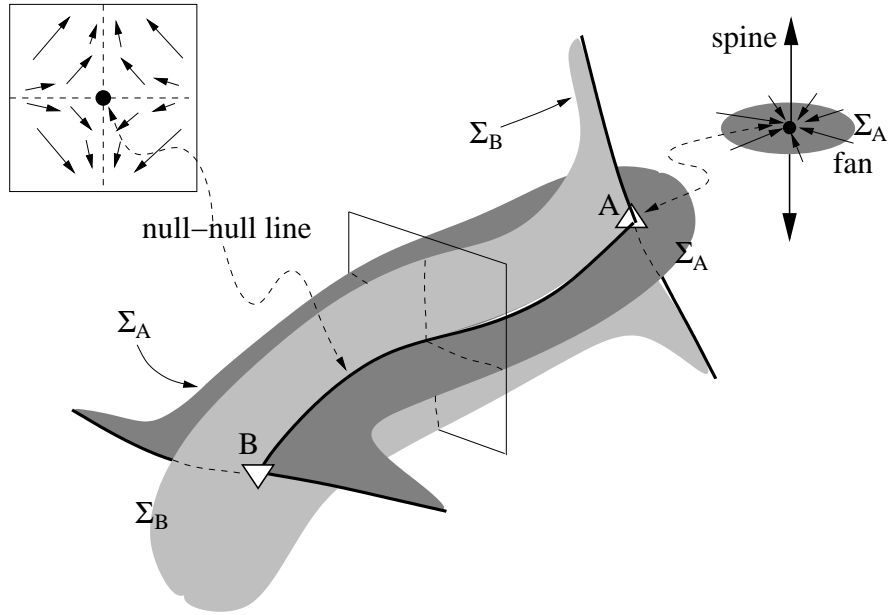
Fig. 4.2. The structure of a null-null line. Positive and negative null points B and A have fan surfaces Σ_B and Σ_A shown in light and dark shades of grey respectively. These intersect transversally along the null-null line shown as a thick black line. Surface Σ_B is then bounded by the two spines from null point A, and similarly for Σ_A and the spines from B. The neighborhood of the null-null line is illustrated by the inset. This shows the direction of **B** within a plane pierced normally by the null-null line at the dark circle. The fan surfaces cross the plane along the dotted lines. [Reproduced from Longcope 2005.]
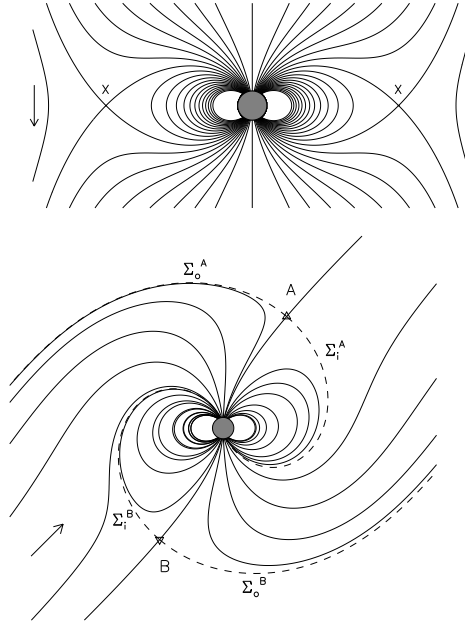
Fig. 4.3. The top panel shows field lines from a southward dipole (similar to that of Earth) immersed in a uniform southward surrounding field (like the interplanetary magnetic field in the absence of a solar wind; arrow), resulting in a special axisymmetric case, here plotted within the noon-midnight meridian. Field lines are rendered by contouring the flux function, $f(r, \theta)$ from Eq. (4.9). The ring of null points is labeled X. The bottom panel shows the case with a northward, tilted external field (arrow). A selection of field lines within the plane of the paper (equivalent to the noon-midnight meridian) are plotted. Fig. 4.4 shows the 3D structure of the fan surfaces. The symmetry is broken, of course, in case there is a plasma flow in the surrounding medium, like the solar wind around the Earth; compare Fig. 10.3.
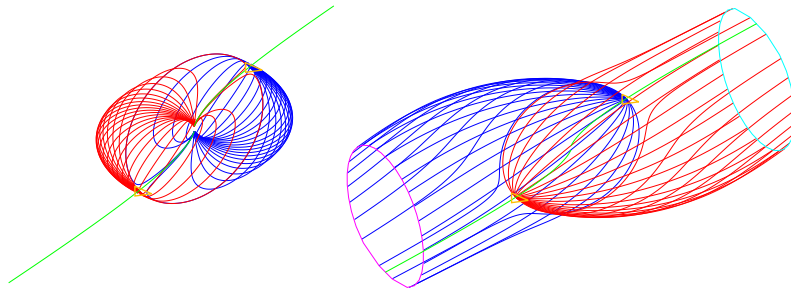

Fig. 4.4. Perspective views, from near the equator, of fan surfaces from the two null points for the field shown in the lower panel of Fig. 4.3. The left panel shows the inner portions of the fan surface from A and B. Dashed field lines labeled Σ_i^A in Σ_i^B in the lower panel of Fig. 4.3 are included in these. The right panel shows the outer portions. Here the surfaces are truncated at the faces of a viewing box. Each fan surface originates from a triangle.
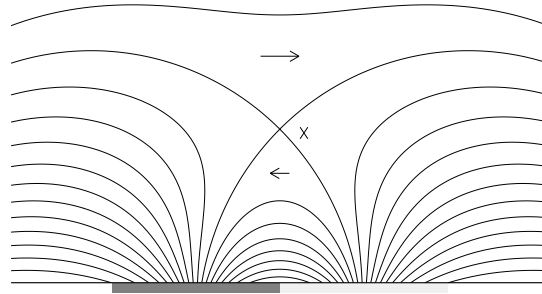
Fig. 4.5. A simple model of a solar coronal magnetic arcade. Field lines connect a positive region (light shade) to a negative region (dark shade). The overlying large-scale field is oppositely directly. It is separated from this by separatrices from a single null point (X).
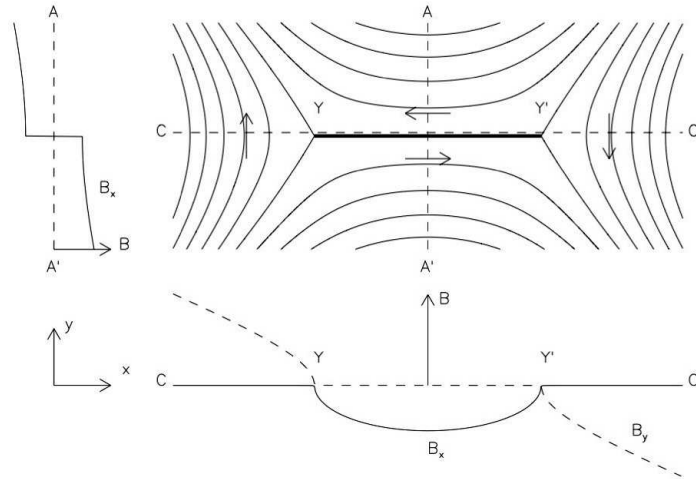
Fig. 4.6. A tangential magnetic discontinuity (TD) of the Green-Syrovatskii type in a two-dimensional magnetic field. The upper right panel shows magnetic field lines as solid curves, and indicates by arrows the direction of the field. The two Y-type nulls, labeled Y and Y', lie at either end of the current sheet (thick black line). Two dashed lines, labeled A–A' and C–C', are cuts along which the magnetic field is plotted to the left and below the field, respectively. Along the vertical cut (A–A', left), the horizontal magnetic field, B_x (solid), suffers a discontinuity at the current sheet ($y = 0$). The vertical field, B_y, is zero over the entire cut. The horizontal cut, (C–C', bottom) passes just above the current sheet, Y–Y'. The horizontal field, B_x (solid), is negative between the tips and vanishes outside the sheet. The vertical field, B_y (dashed), vanishes everywhere along the sheet (it is a TD) and is non-zero outside it. Note that both components vanish at the null points Y and Y'.
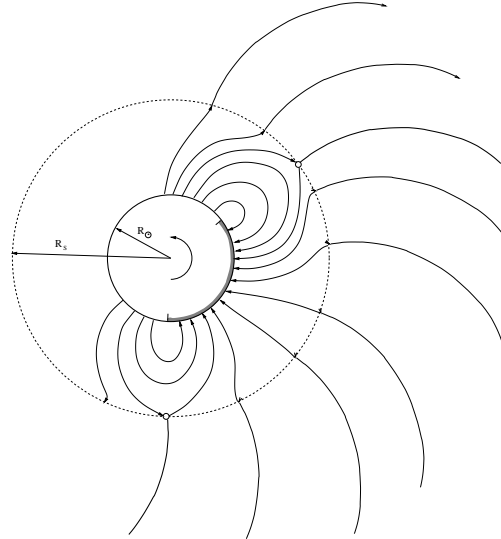
Fig. 4.7. A schematic depiction of a potential-field source-surface (PFSS) model as viewed from above the Sun's North pole (the sense of rotation is indicated by a semi-circular arrow). A dashed circle shows the source surface at $r = R_{\mathrm{S}}$. The field is made purely radial at this surface by setting $B_\theta = B_\phi = 0$. Between the source surface and the solar surface, $r = R_\odot$, the magnetic field is potential: $\mathbf{B} = -\nabla\chi$. Field lines are anchored to the photosphere in a negative region (shaded segment) and in positive regions. Outside the source surface the field is swept back in a spiral by the solar rotation. Two null points (X-points, actually lines of null points) are shown as circles on the source surface. The upward and downward separatrices are shown extending from these circles. The sector boundaries between heliospheric fields of opposite radial polarity are shown as darker curves.
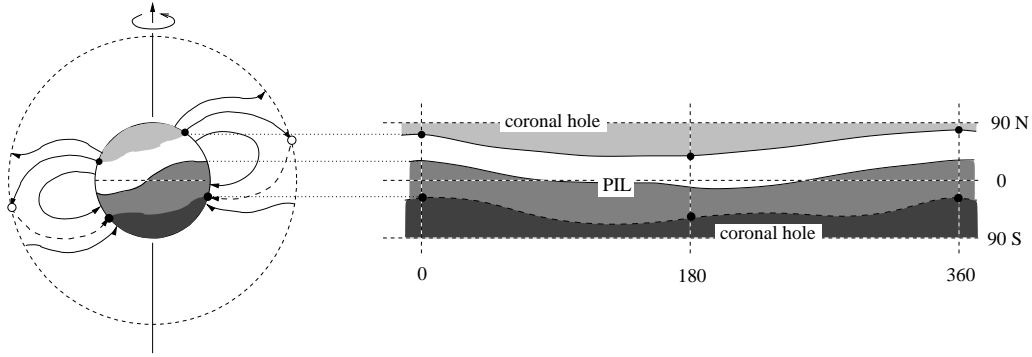
Fig. 4.8. A schematic depiction of coronal hole boundaries defined by the source surface model. The left panel is a meridional cut, and the right panel shows the full solar surface $(r = R_\odot)$ plotted as sine of latitude versus longitude. The dark curves are the footprints of the upward and downward separatrices respectively; the black curve is the polarity-inversion line, or PIL. The shaded regions are (from top to bottom) the outward coronal hole (light grey), positive closed flux (white), negative closed flux (grey) and inward coronal hole (dark grey). The same shading in the left-hand panel indicates how these regions might appear on the disk. [Reproduced from Longcope 2005.]
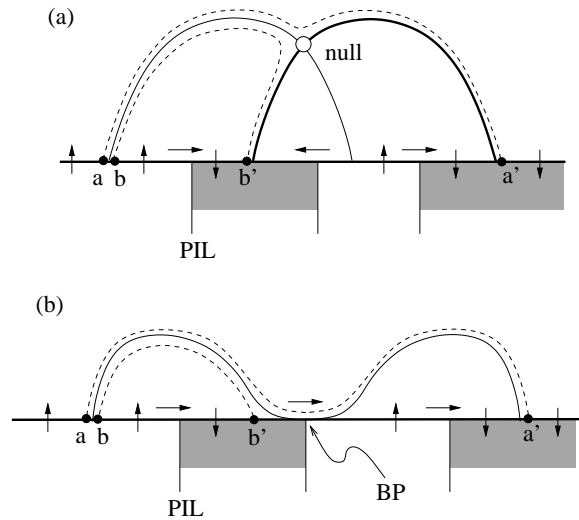
Fig. 4.9. Two-dimensional illustrations of field line mappings exhibiting the two possible types of mapping discontinuities. In each case neighboring footpoints a and b map to points a' and b' separated by considerable distance. Each time the photospheric field is quadrupolar with 3 polarity-inversion lines (PILs) indicated by vertical lines. The negative (downward) photospheric regions are shaded, and vertical and horizontal arrows show the sense of the photospheric field. (a) A field with a coronal null point. Although it is a 2-dimensional illustration we take the null to be negative, with spines indicated by dark solid lines and fan field lines by thinner solid lines. Footpoints a and b map from opposite sides of the fan surface to points near each of the spine field footpoints. (b) A bald patch where a coronal field line (solid) grazes the photospheric surface, crossing in the inverse sense, from negative to positive, as indicated by the horizontal arrow. [Reproduced from Longcope 2005.]
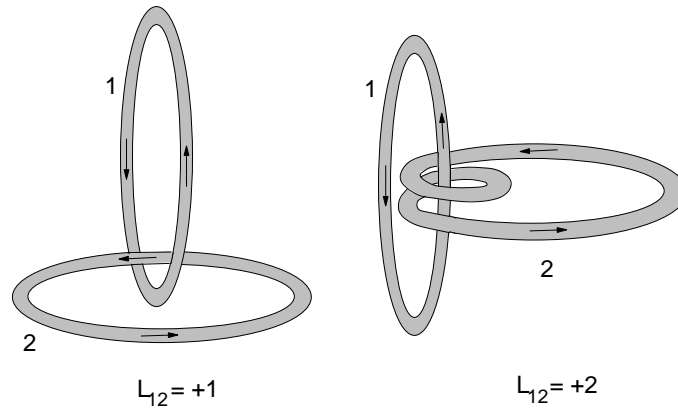
$L_{12} = +1$ $L_{12} = +2$

Fig. 4.10. Illustrations of the linking number between a pair of closed curves, labeled 1 and 2. For clarity the curves are shown with finite width. Each curve is traversed in the direction indicated by the arrow. The pair on the left are linked with linking number $L_{21} = +1$; the pair on the right with $L_{12} = +2$.
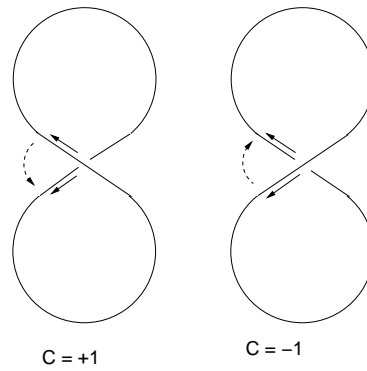
Fig. 4.11. Illustration of crossing number for a closed curve. The curve on the left has one positive crossing. The dashed arc shows how the upper segment must be rotated to align it with the lower one: in the positive (counter-clockwise) direction. The left curve has $C = -1$.
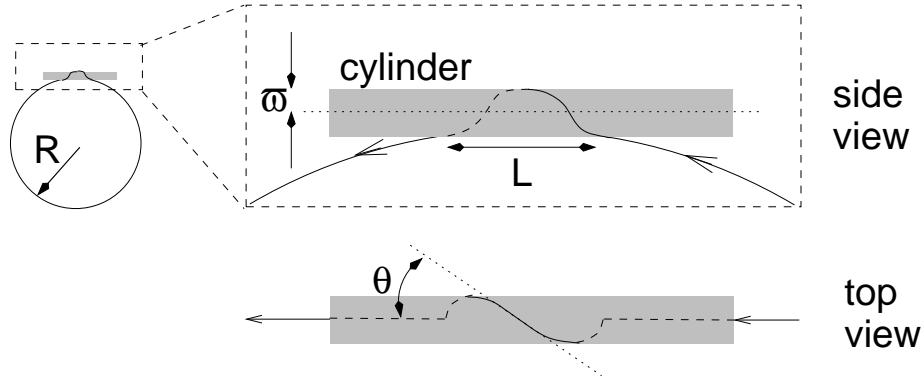
Fig. 4.12. A simplified model of an active region flux tube deformed by emergence and Coriolis effects. The deformed section wraps around a cylinder of radius, ϖ (shaded).
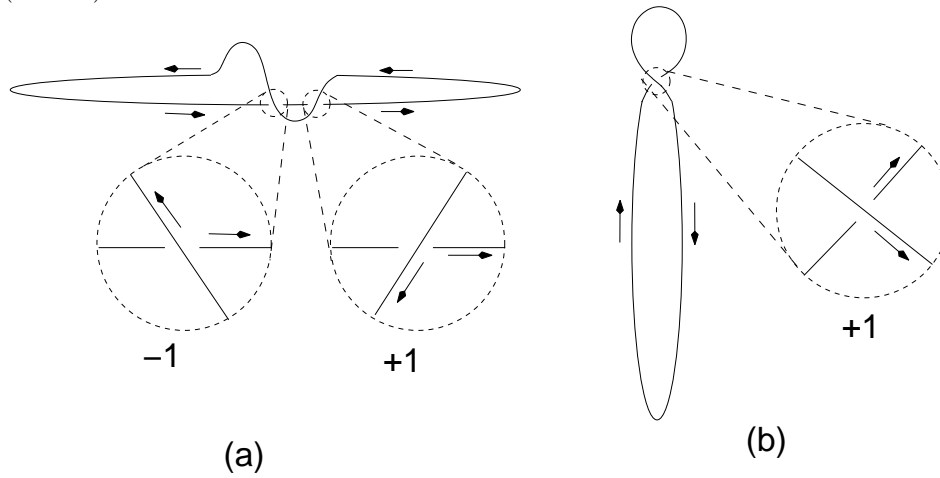

(a)

(b)

Fig. 4.13. The curve from Fig. 4.12 viewed from two different angles. The entire curve is shown and the cylindrical deformation is exaggerated for clarity. (a) A view slightly different from "top view". Two crossings are enhanced as insets to show they are of opposite signs. (b) A view very close to the axis of the cylinder. Only one crossing (positive) occurs, also enhanced as an inset.
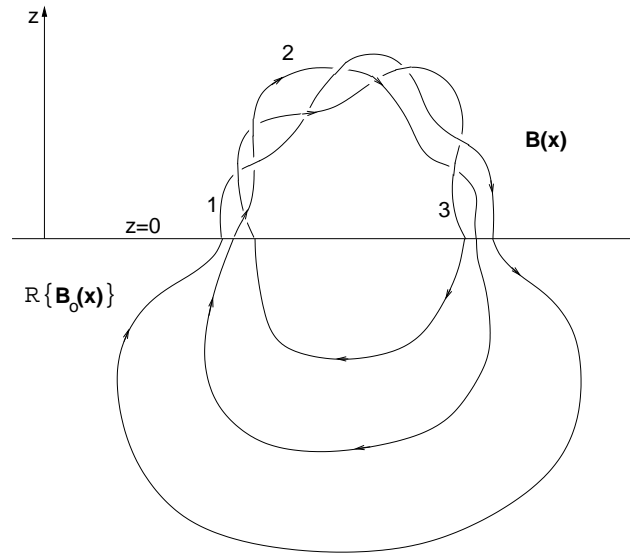
Fig. 4.14. An illustration of how a reference field defines a topological helicity: the relative helicity. The field, $\mathbf{B}(\mathbf{x})$ is defined in the corona ($z > 0$) but its field lines have footpoints in the photosphere ($z = 0$). Applying the mirror-reflection operator, $\mathcal{R}$, to the reference field, $\mathbf{B}_0(\mathbf{x})$, gives a field with which to continue field lines below the photosphere ($z < 0$). This permits field lines to form closed curves for which topological quantities such as linking are well defined. In this figure $L_{13} = -1$.

5

Magnetic reconnection

by Terry G. Forbes
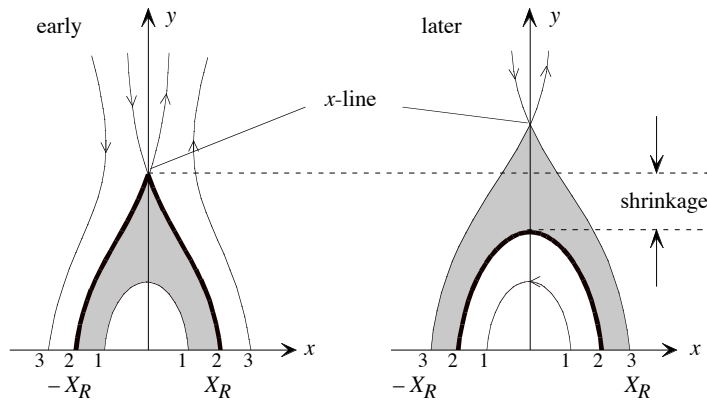
Fig. 5.1. Schematic diagram illustrating the magnetic field line topology in the reconnection model of flare loops at two different times. The shaded area is the X-ray loop system, while the numbers at the base mark the footpoints of individual field lines. The outermost edges of the flare ribbons are located at X_R and $-X_R$.
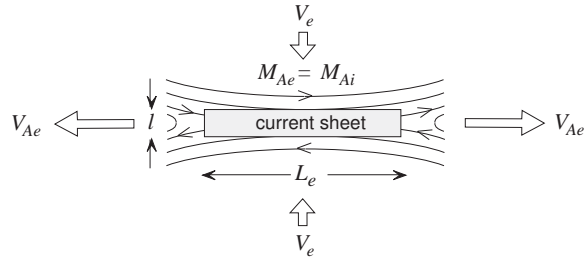
V_e

$M_{Ae} = M_{Ai}$

V_{Ae} l current sheet V_{Ae}

L_e

V_e

Fig. 5.2. The Sweet-Parker field configuration. Plasma flows into the upper and lower sides of a current sheet of length $L_{\rm e}$, but must exit through the narrow tips of the sheet of width l. Because the field is assumed to be uniform in the inflow region, the external *Alfvén Mach number*, $M_{\rm Ae} = v_{\rm e}/v_{\rm Ae}$, at large distance is the same as the internal Alfvén Mach number, M_{Ai}, at the midpoint edge of the current sheet.
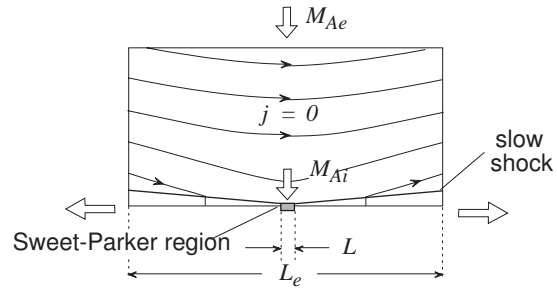
Fig. 5.3. Petschek's field configuration. Here the length, L, of the Sweet-Parker current sheet is much shorter than the global scale length, $L_{\rm e}$, and the magnetic field in the inflow is nonuniform. Two pairs of standing slow-mode shocks extend outwards from the central current sheet. Petschek's model assumes that the current density in the inflow region is zero and that there are no external sources of field at large distance.
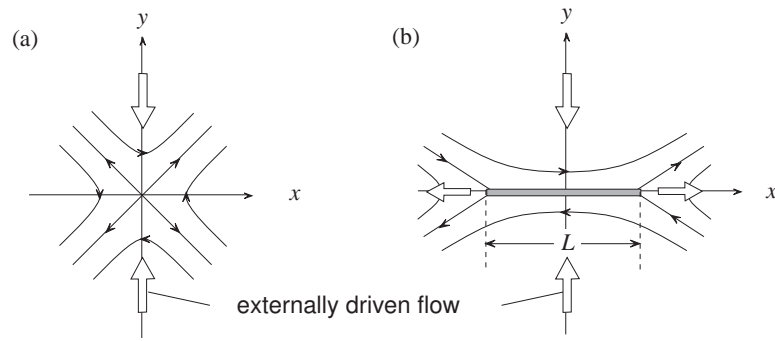
Fig. 5.4. Syrovatskii's field configuration. Unlike Petschek's configuration, this one has external sources which produce an x-type configuration even when local sources of current are absent. The application of external driving creates a current sheet whose length, L, depends on the temporal history of the driving and the rate at which reconnection operates. The fastest reconnection rate occurs when L is equal to the external scale length, L_{e}.
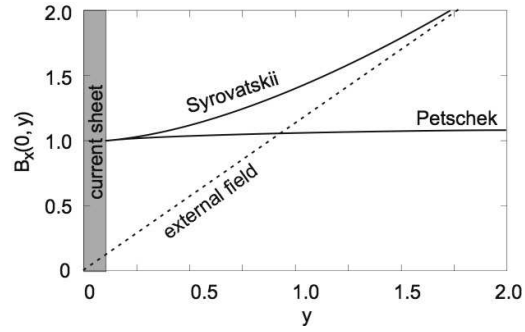
Fig. 5.5. The variation of the magnetic field in the inflow region of Petschek's and Syrovatskii's models along the axis of symmetry (y axis). At large distance the variation in Syrovatskii's model is determined by external field sources at infinity. The magnetic fields are normalized to their values at the edge of the current sheet, and the distance y is normalized to the length L of the current sheet. For the Petschek curve, $M_{Ae} = 0.02$, $l = 0.1L$, and $L_e = 2L$.
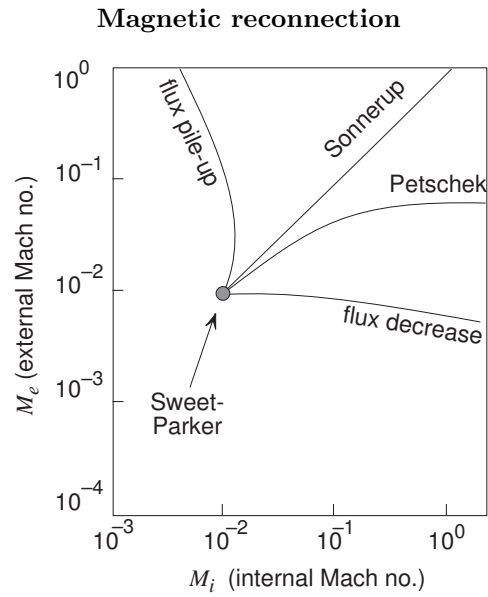
Fig. 5.6. External Alfvén Mach number, M_{Ae}, versus the internal Alfvén Mach number, M_{Ai}, for the family of solutions obtained by Priest and Forbes (1986). These solutions are obtained by an expansion in terms of the inflow Alfvén Mach number for small variations of the field around the uniform inflow field assumed in the Sweet-Parker model. Solutions with the labeled characteristics are obtained for different choices of the parameters describing the distant boundary conditions.
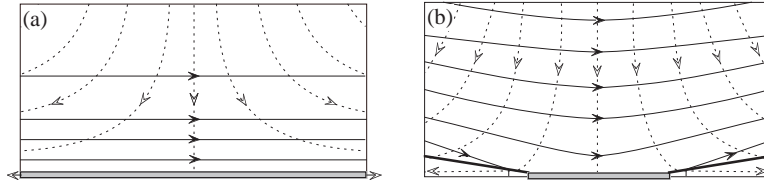
Fig. 5.7. The stagnation-point-flow solution (a) obtained by Parker (1973) for magnetic field annihilation at a current sheet, and the closely related flux-pile-up solution (b) obtained by Priest and Forbes (1986).
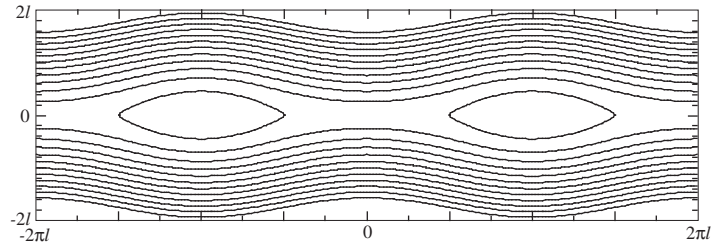
Fig. 5.8. Typical magnetic island structure resulting from tearing instability of a plane current sheet. The contour lines show magnetic flux surfaces of the magnetic field (Forbes 2006).
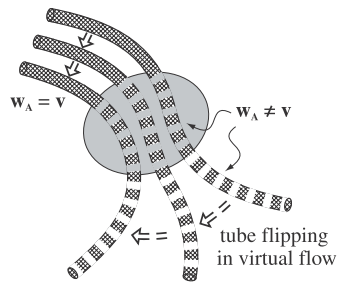
Fig. 5.9. Schematic diagram illustrating the ambiguity that occurs in the definition of field line velocity in three dimensions. The dashed lines indicate the projection of magnetic flux tubes onto the two-dimensional plane (from Priest et al. 2003).
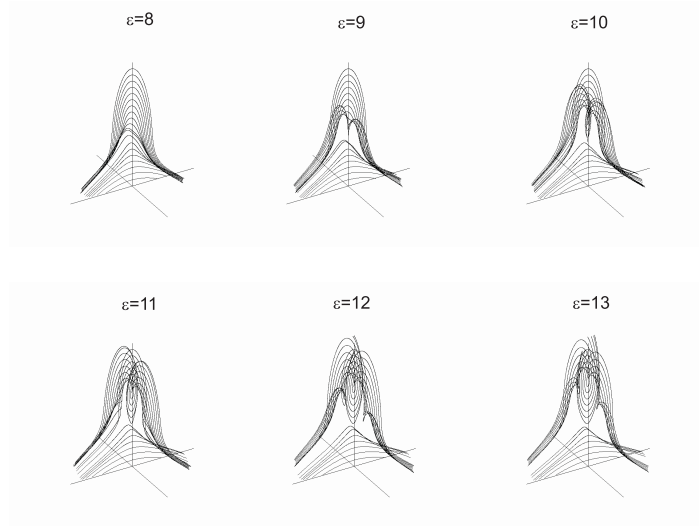
Fig. 5.10. Evolution of the magnetic field in the Hesse et al. (2005) model for line-tied reconnection in the corona.
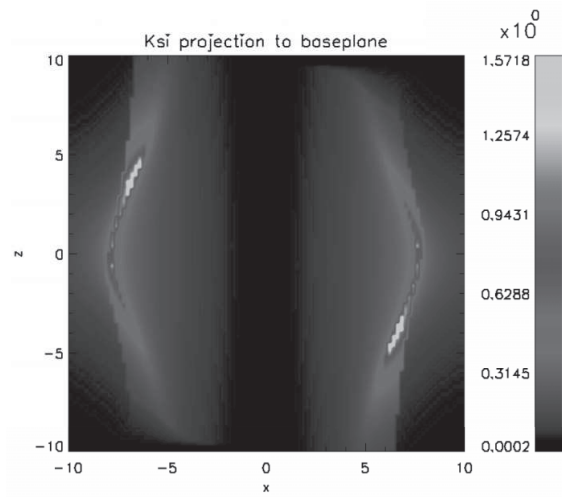
Fig. 5.11. The mapping onto the $z = 0$ surface of the net potential electric field produced by induction in the Hesse et al. (2005) model for $\epsilon = 10$ in Eq. (5.28).
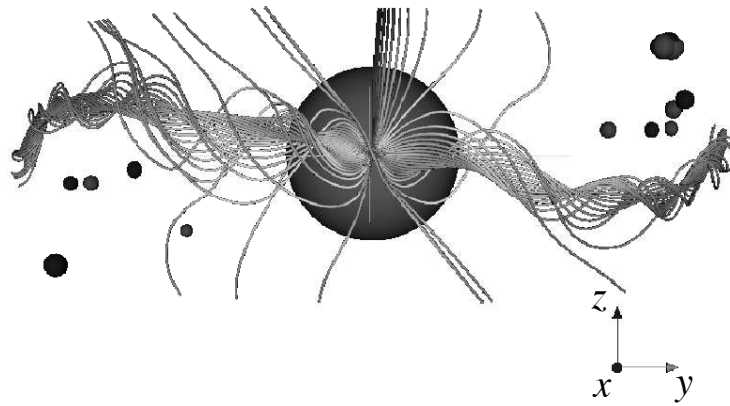
Fig. 5.12. Global MHD modeling of Earth's magnetosphere. This figure shows a view from the Sun of the dayside magnetopause from a global MHD simulation of the terrestrial magnetosphere. For this figure the interplanetary magnetic field is oriented southward, and there is a long flux rope at the sub-solar region of the magnetopause. The small spheres show the location of the multiple neutral points that form (Dorelli et al. 2007).
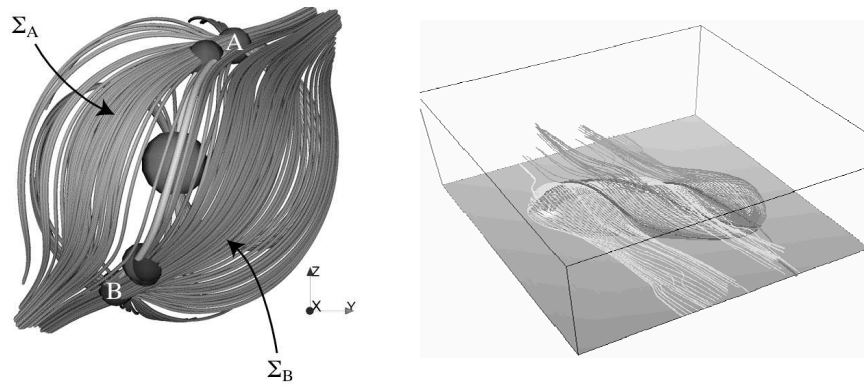
Fig. 5.13. MHD simulations of separator reconnection. Left: A view from the Sun of the Earth's dayside magnetopause for a case of a purely northward IMF, with the Earth's dipole tilted in the GSE $y-z$ plane by 45° (compare with the bottom panel in Fig. 4.3 for a potential field model in case the Earth's dipole field is aligned with the z axis). A separator line (see Fig. 4.2 for the detailed geometry of such a null-null line) extends across the magnetopause and terminates in the polar cusp neutral points that are indicated by the small spheres (from Dorelli et al. 2007). Right: A simulated solar coronal magnetic skeleton. Two separatrix surfaces intersect to form three separator lines (from Maclean et al. 2006).

6

Structures of the magnetic field

by Mark B. Moldwin, George L. Siscoe, and Carolus J. Schrijver
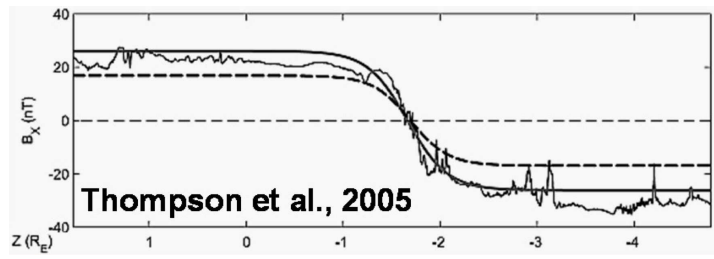
Fig. 6.1. Fits of the Harris current sheet formula to a crossing of the Cluster space-craft of a quiet current sheet in Earth's magnetotail. Two curves result from taking either the field or the current as the independent variable.
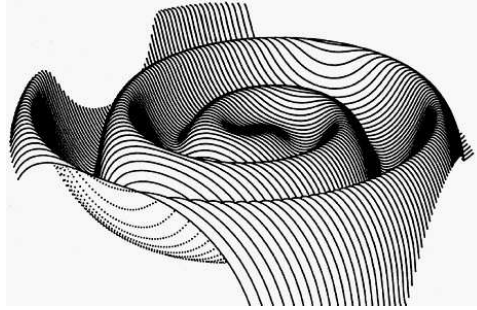
Fig. 6.2. The heliospheric current sheet modeled for a 15° tilt of the solar magnetic equator. For a slow wind at 400 km/s, the figure is 25 AU across, extending to beyond Saturn's orbit; for a fast wind at 800 km/s, the figure is 12.5 AU across, extending only to just beyond Jupiter's orbit (see Ch. 8 for the properties of the solar wind and the details of the "Parker spiral" of which this figure shows one aspect). (Fig. from Jokipii and Thomas, 1981)
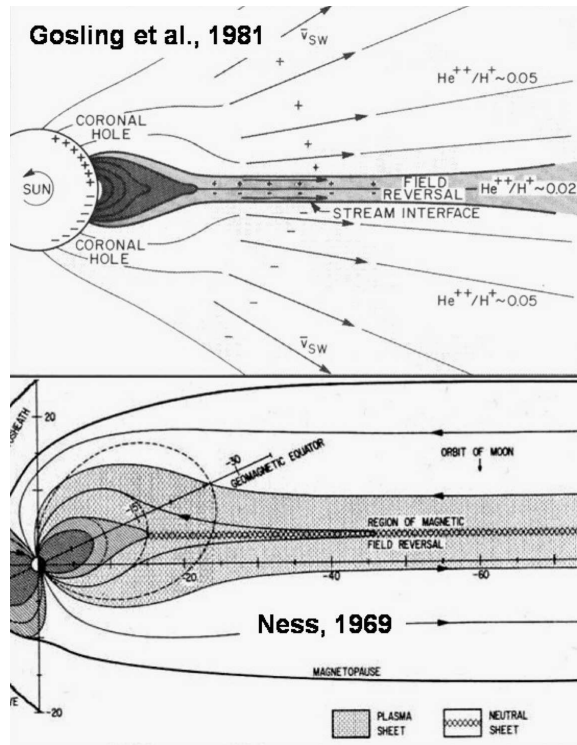
Fig. 6.3. A comparison of the heliospheric current sheet (labeled 'field reversal' in this figure) and its plasma sheet (top) and the magnetospheric current sheet (here 'neutral sheet') and its plasma sheet (bottom).
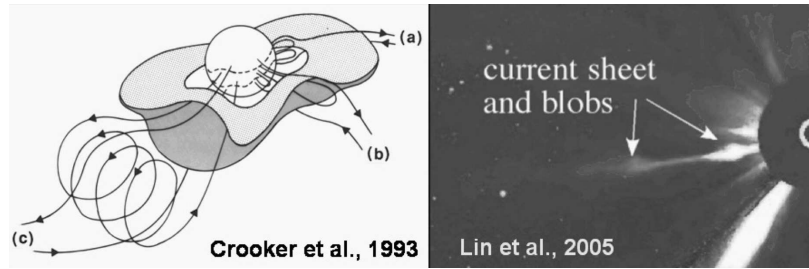
Fig. 6.4. The relation between a CME flux tube (c) and the heliospheric current sheet (HCS; left) and an image of the smaller kind of coronal ejection known as 'blobs' (right).
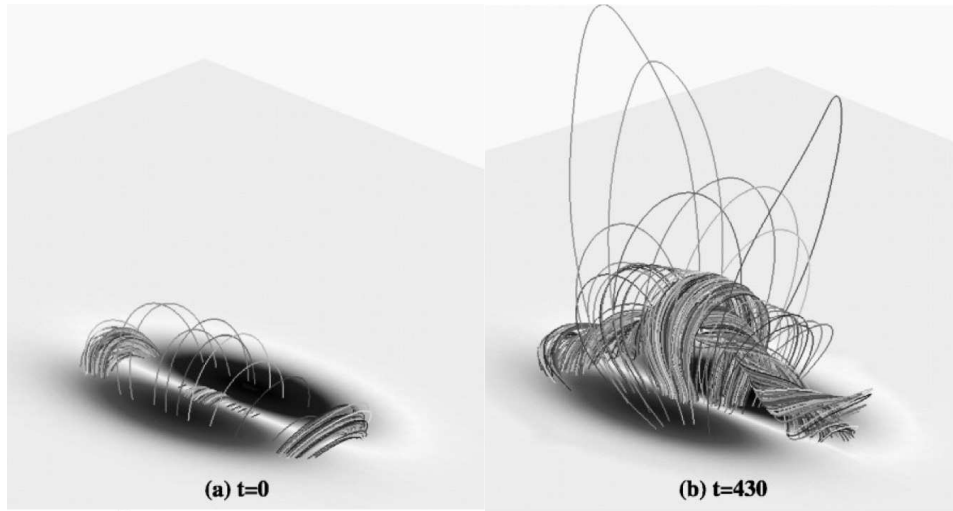
Fig. 6.5. Model results of the formation of a twisted flux rope from magnetic flux eruption from the solar surface. (Fig. from Amari et al., 2000)
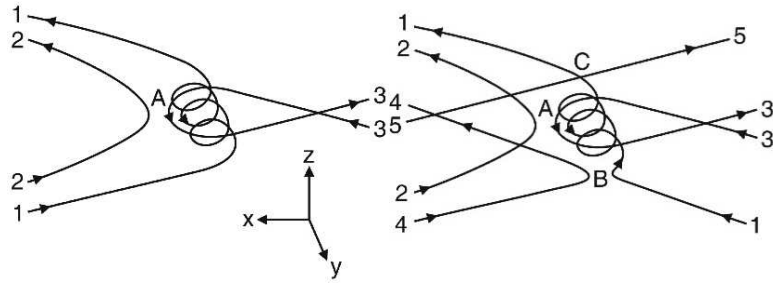
Fig. 6.6. Reconnection of plasma-sheet field lines with a B_y component leads to the formation and subsequent ejection of a twisted flux tube or flux rope (Hughes and Sibeck, 1987).
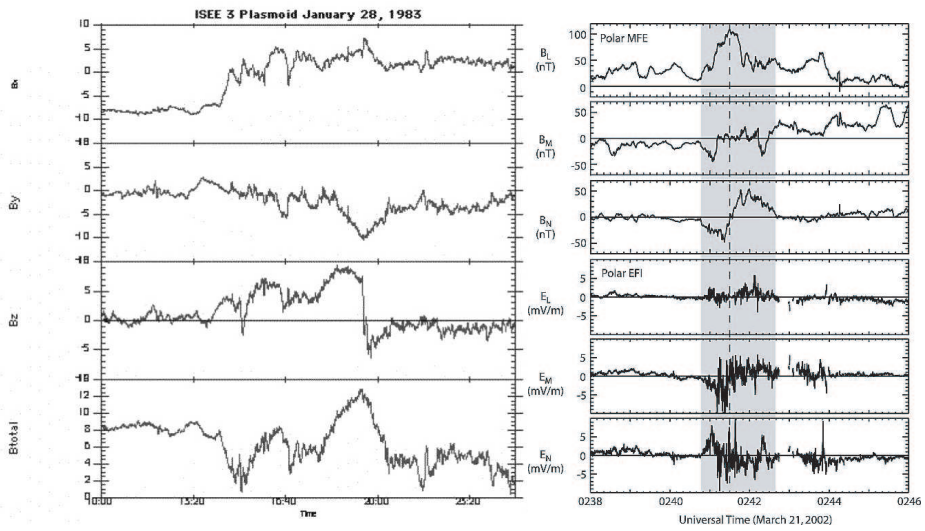
Fig. 6.7. *Left:* The magnetic field observed by ISEE-3 deep in the Earth's magnetotail showing the presence of the a magnetic flux rope plasmoid. *Right:* Polar magnetic and electric field observations for a flux transfer event or FTE. (From Le et al., 2008)
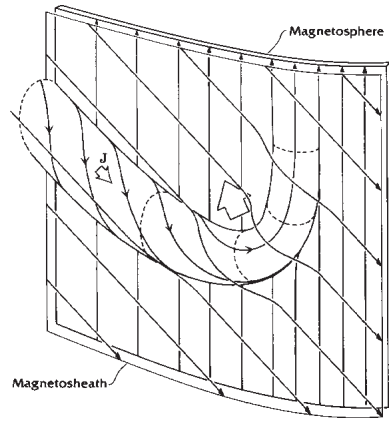
Fig. 6.8. A flux transfer event at the Earth's magnetopause (from Russel and Elphic 1979).
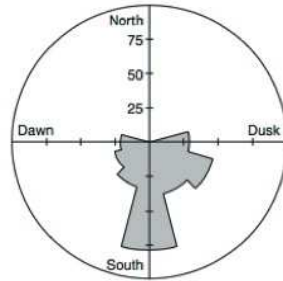
Fig. 6.9. The occurrence frequency of flux-transfer events as a function of the angle of the interplanetary magnetic field in the $y - z$ GSM plane. (Fig. from Berchem and Russell, 1984)
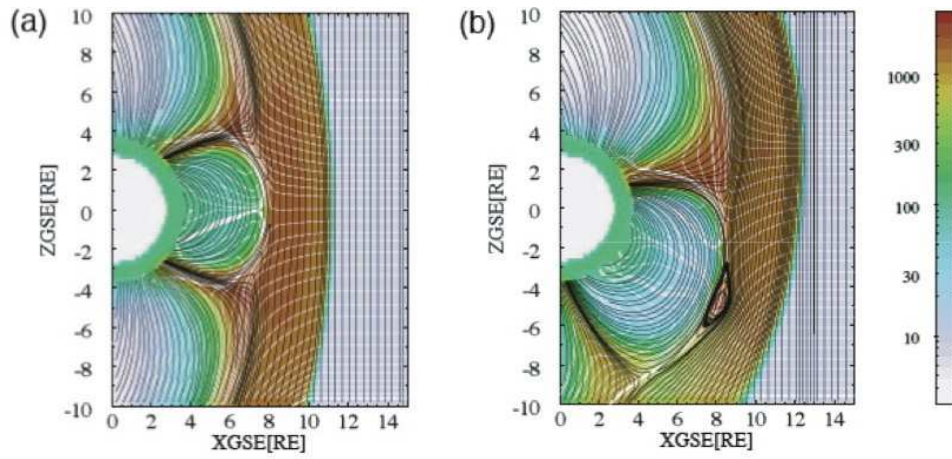
Fig. 6.10. Illustration of the role that dipole tilt plays in the formation of flux-transfer events (from Raeder, 2006). The colors represent the plasma pressure.
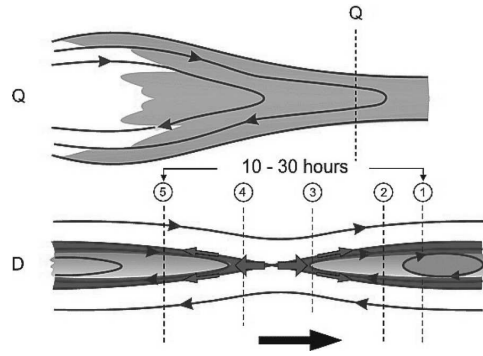
Fig. 6.11. A schematic of the configuration of the Jovian magnetotail for quiet (Q) and disturbed (D) times. The numbered lines indicate different field and flow observations that have been observed with the Galileo spacecraft during disturbed intervals (from Kronberg *et al.*, 2005).
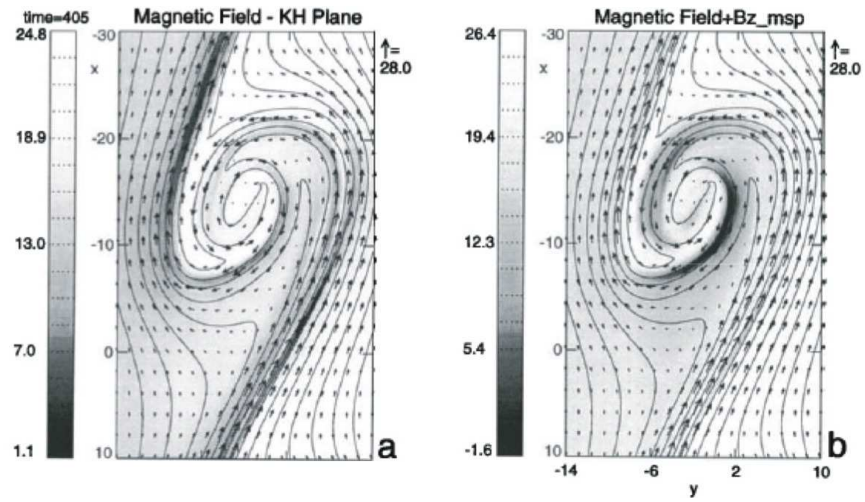
Fig. 6.12. Magnetic field lines and vectors of Kelvin-Hemlholtz vortices produced on the magnetopause in a 2-D MHD simulation. The grey scale shows the B_z component *(a)* in the simulation plane and *(b)* projected into magnetospheric coordinates. (from Otto and Fairfield, 2006)
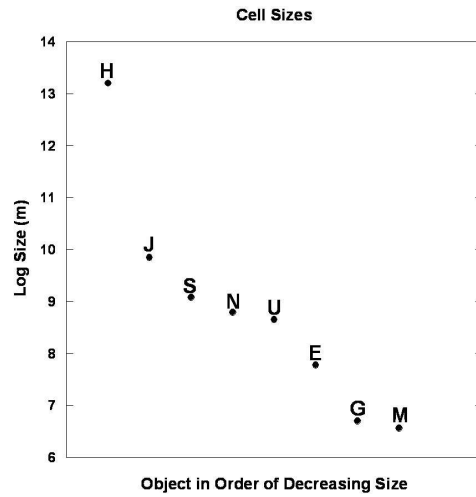
Fig. 6.13. Estimates of scale sizes of heliophysical examples of magnetic cells, ordered by magnitude (taken from Chs. 10 and 13): H, heliosphere; J, Jupiter; S, Saturn; N, Neptune; U, Uranus; E, Earth; G, Ganymede; M, Mercury.).

7

Turbulence in space plasmas
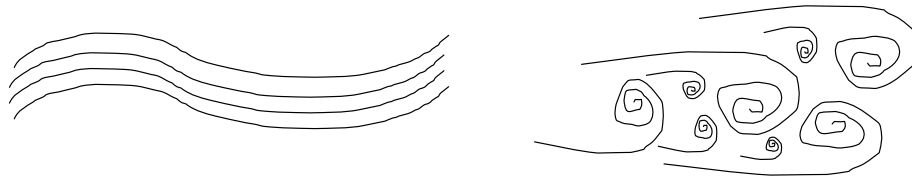
by Charles W. Smith

Fig. 7.1. (left) Schematic illustration of laminar fluid flow. The behavior is orderly and predictable. (right) Schematic of turbulent flow downstream of generating grid (off image to left). The flow is disordered and composed of many circulation patterns of varying scale.

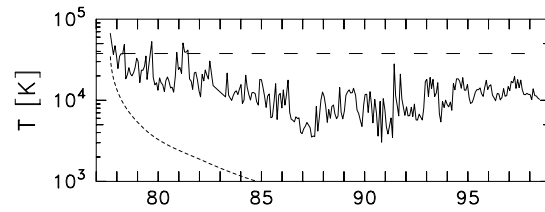| Velocity Range	γ
[km/s]	$0.3 - 1\,$AU
< 300	1.331 ± 0.129
300 to 400	1.223 ± 0.087
400 to 500	1.033 ± 0.095
500 to 600	0.826 ± 0.099
600 to 700	0.762 ± 0.092
700 to 800	0.808 ± 0.169

Fig. 7.2. (left) Radial dependence of thermal proton temperatures $T_p \sim R^{-\gamma}$ from 0.3 to 1 AU shown as a function of wind speed. Variations shallower than $R^{-4/3}$ imply in situ heating. Reproduced from **?** (**?**). More recent analyses indicate that in situ acceleration of the slow wind implies the radial dependence of slow wind temperatures is more shallow than shown. (right) Proton temperatures observed by Voyager 2 (solid) from 1 to 70 AU. Average 1 AU temperature represented by horizontal dashed line. Adiabatic expansion from 1 AU is shown by the descending short-dashed line. Reproduced from **?** (**?**).
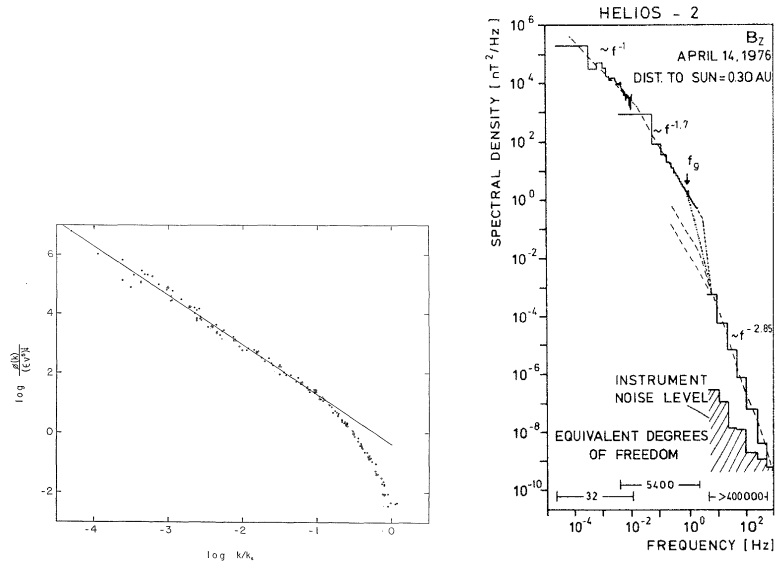
Fig. 7.3. (left) Inertial and dissipation range spectrum for hydrodynamic turbulence. Reproduced from **?** (**?**) as augmentation of the **?** (**?**) result. (right) Spectrum of IMF measured at 0.3 AU by Helios spacecraft showing inertial and dissipation range spectra. The latter extends to 200 Hz, which is the limit of the measurement. Reproduced from **?** (**?**).
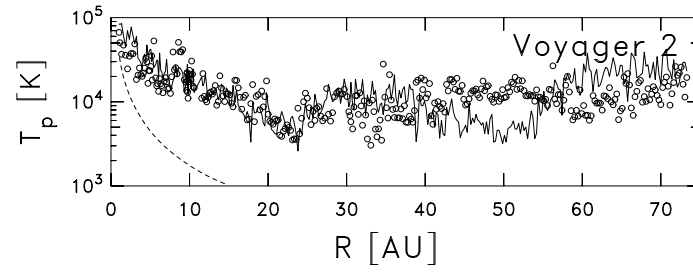
Fig. 7.4. Solar rotation averages of Voyager 2 proton temperatures (circles) and turbulence theory prediction (line) derived from Omnitape 1 AU boundary condition. Adiabatic expansion from 1 AU is also shown (dashed line).
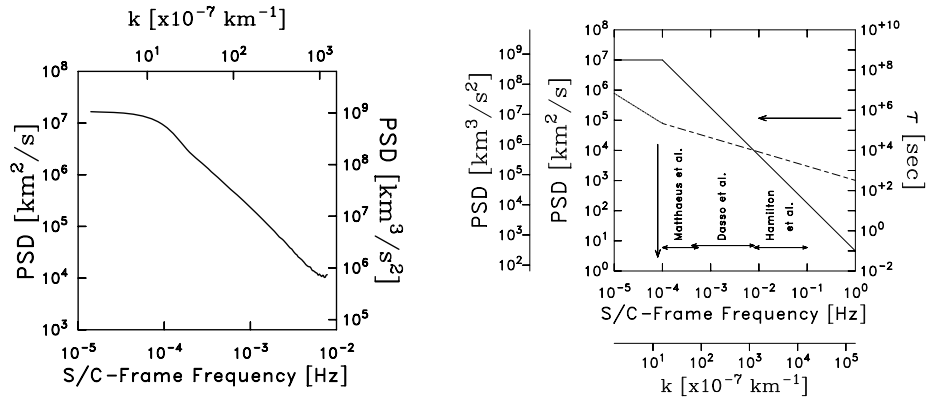
Fig. 7.5. (left) Computed spectrum of total power for ACE observations from 1998 through 2004. Figure taken from **?** (**?**). (right) Representation of total power spectrum (solid curve) and computed eddy turnover time (lifetime) as a function of scale. Horizontal arrow marks average convection time from Sun to 1 AU. Frequency intervals representing the **?** (**?**) and **?** (**?**) analyses are shown. Figure taken from **?** (**?**).
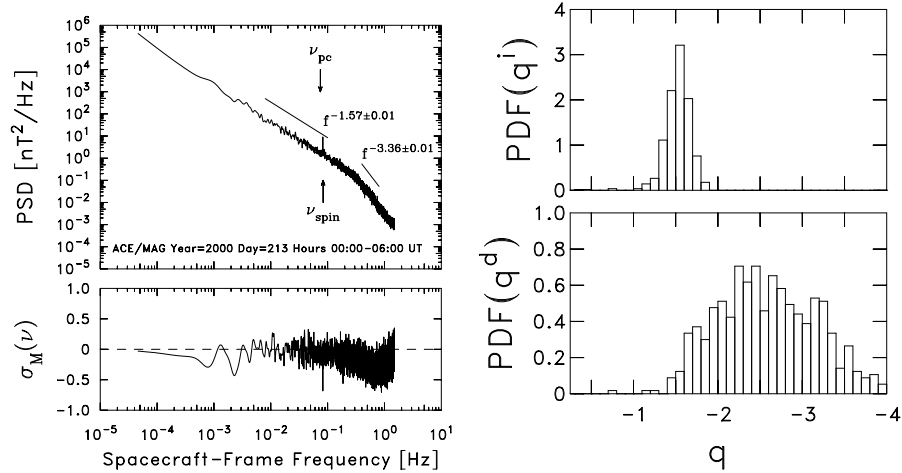
Fig. 7.6. (left) Spectrum of ACE magnetic field interval for time shown. Inertial range spectral slope is -1.57, midway between $-5/3$ and $-3/2$ expected values. (right) Distribution of inertial range spectral indices (top) and dissipation range spectral indices (bottom) from ACE study. Both the normalized magnetic helicity (bottom left) and dissipation range spectral indices (bottom right) are discussed in Sect. 7.6.3. Both figures taken from **?** (**?**).
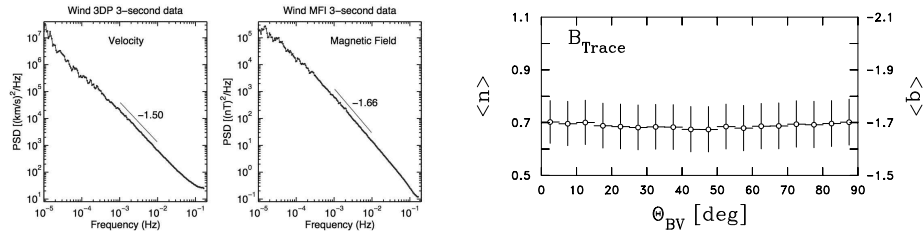
Fig. 7.7. (left) Trace spectrum of velocity fluctuations showing a $-3/2$ fit. (center) Trace spectrum of magnetic fluctuations showing a $-5/3$ fit. Both figures taken from **?** (**?**). (right) Average spectral index of magnetic fluctuation trace spectrum using nine years of ACE data from 1998-2006. (J. A. Tessein, private communication, 2007.)

L [lag x10^5 km]

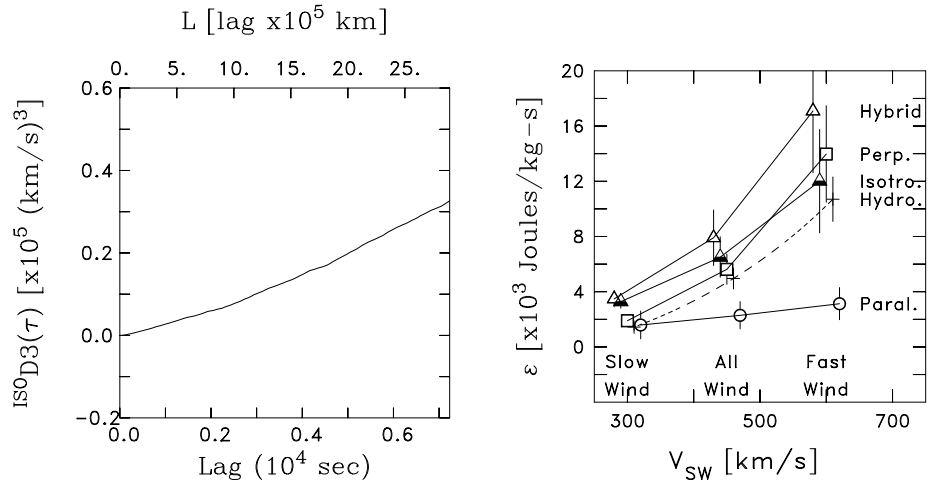Fig. 7.8. (left) Plot of $D_3^{\pm}$ analysis in the isotropic formalism using ACE data for the 7 years surrounding solar maximum. The curve is for energy cascade of total power. (right) Summary plot of hybrid D_3 analysis at 1 AU using ACE observations showing strongest cascade in the perpendicular direction. Both panels reproduced from **?** (**?**).

8

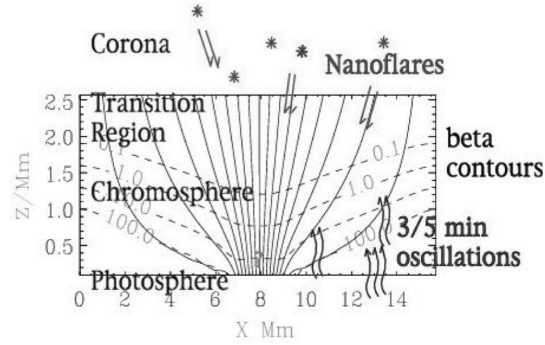# The solar atmosphere

by Viggo H. Hansteen

Fig. 8.1. Schematic view of the structure of the solar atmosphere (outside of sunspots): In the photosphere the gas pressure is larger than the magnetic pressure and photospheric motions are driven by convection — a mainly hydrodynamic phenomenon that brings up new magnetic flux, buffets, shreds, and reorganizes existing field. Oscillations of somewhat higher frequency than the photospherically dominant 5 minute oscillations propagate into the chromosphere. Upon reaching the level where the exponentially decreasing gas pressure equals the magnetic pressure ($\beta = 1$), the surviving sound waves may be converted into other wave modes. It is likely that the processes heating the corona and magnetic chromosphere are episodic; this will likely induce large temperature differences, flows, and other non-steady phenomena that produce other wave modes.
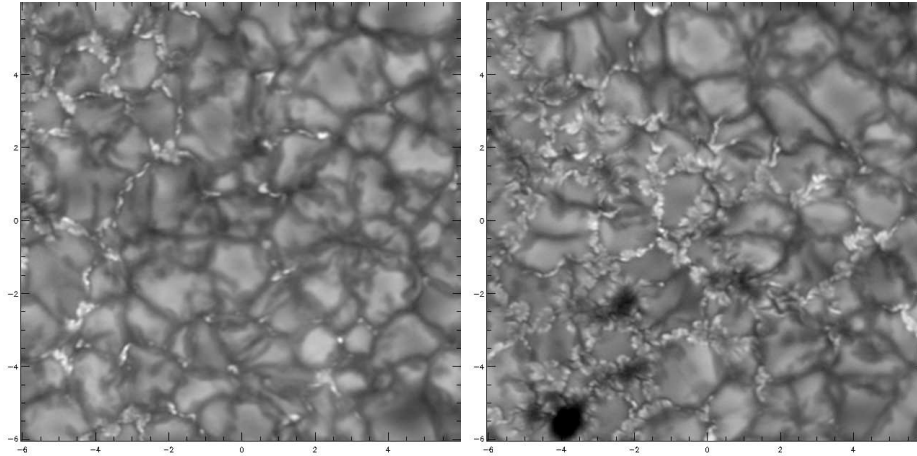
Fig. 8.2. The image on the left shows a typical quiet photospheric region observed in the G-band with the Swedish 1-meter Solar Telescope. The image on the right shows a plage region where the total amount of magnetic flux penetrating the photosphere is larger. The axes of both panels are numbered in arcseconds measured on the Sun; 1 arcsec is approximately 725 km. The G-band near 430 nm contains several spectral lines, notably the lines of the CH-molecule, and is formed near the solar surface (the height where $\tau_{500 \text{ nm}} = 1$); the granulation and intergranular lanes some 100 km above this height, bright points some 200 km below — as explained in the text. Bright points are regions of enhanced magnetic field concentrated and contained by the granular motions. Notice also that bright points are pulled into ribbons and may fill the entire intergranular lane. The image on the right shows a photospheric plage region. Notice the large number of phenomena showing complex structure; ribbons, "flowers", micropores, as well as isolated and seemingly simple bright points. The magnetic field in this image is in places strong enough to perturb granulation dynamics and the granules appear "abnormal" while displaying a slower evolution than in the quieter photosphere.
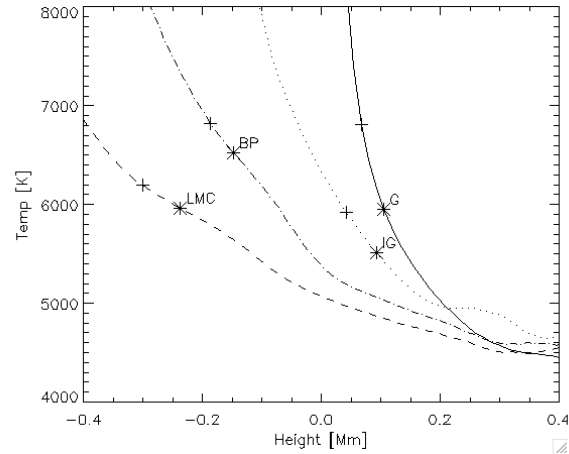
Fig. 8.3. The gas temperature as a function of height for four positions in the model
of Carlsson et al. (2004): The curves marked 'G' and 'IG' represent positions in
a typical granule center and intergranular lane. The asterisk show the formation
height where the G-band is formed; emergent radiation from the granule center is
formed at a higher temperature and thus appears brighter than the intergranular
lane. The curves marked 'BP' and 'LMC' represent a bright point and the region of
greatest magnetic flux concentration; the bright point appears bright as the opacity
is low enough to sample gas as great depths, even though at any geometric point in
the simulation the temperature is higher in both granules and intergranular lanes.
The same is also true for the region of greatest magnetic flux, strong enough to
hinder convection and at the same time large enough in horizontal size to hinder
radiative heating from the 'walls' of the flux tube. Height is measured relative to the
solar surface ($\tau_{500\ \text{nm}} = 1$). The effective temperature of the Sun is $T_{\text{eff}} = 5780$ K.
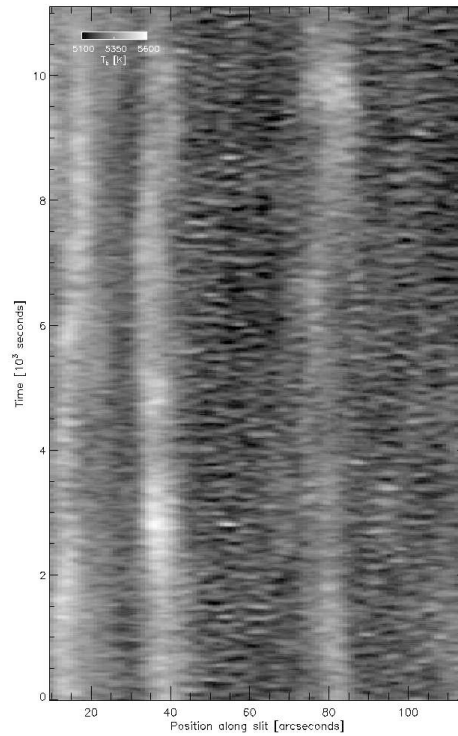
Fig. 8.4. Chromospheric oscillations as seen in the "brightness temperature" of the C continuum formed near 104 nm at a height roughly 1100 km above the photosphere (the brightness temperature is the temperature the radiating material would have if it were in local thermodynamic equilibrium). This observation is made by pointing the SUMER slit at a given, quiet sun, location of the Sun and making an exposure every 20 s or so. The image composite is made by displaying consecutive exposures of the slit vertically. The persistent brighter vertical bands represent areas of enhanced magnetic field. The horizontal structures most clearly visible between the bright vertical bands can be explained by upwardly propagating 5 mHz oscillations. (**?**).
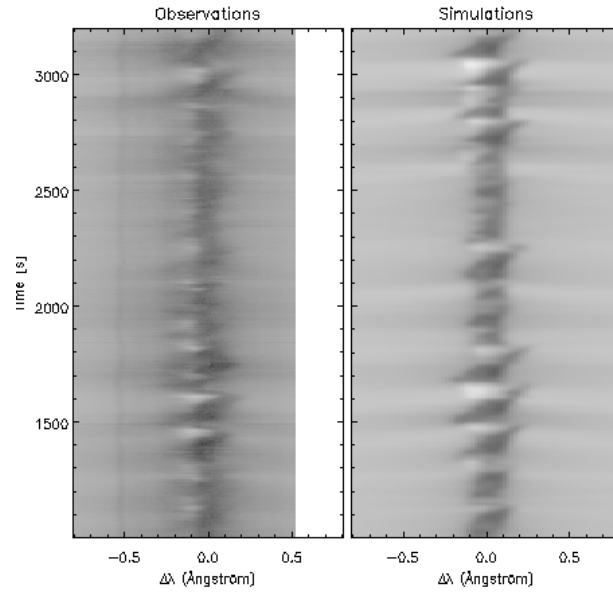
Fig. 8.5. The Ca II H-line profile as a function of time. Multiple repeated exposures are made with a slit fixed at a given position on the Sun. The observed line profile in a quiet, internetwork, position is shown in the left panel. A 1d radiation-hydrodynamic model due to Carlsson and Stein (1995), containing upwardly propagating acoustic waves driven by a piston computed from the doppler shift measured in an Fe I line in the blue wing, results in the Ca II H-line profiles shown in the right panel. Waves appear first in the line wings and propagate towards line center as the acoustic wave moves upward in the atmosphere. A peak brightening on the violet side of the line core, formed some 1000 km above the photosphere, indicates that the wave amplitude has grown and that the wave is non-linear, i.e., has turned into a shock wave.
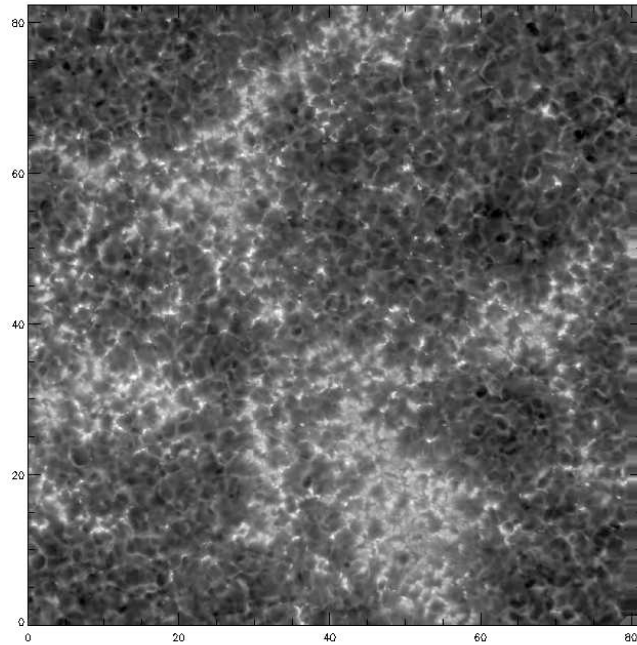
Fig. 8.6. The chromospheric network as observed with the Swedish 1-meter Solar Telescope in the Ca II H-line band in a region covering roughly 80×80 arcsec^2 (60×60 Mm^2). Most emission in this image is formed some hundreds of kilometers above the photosphere. We see inverse granulation, an image of the 'overshoot' of vertical granular flow with horizontal scales identical to that of regular granulation. The brighter magnetic elements (bright points) are advected with the granular flow and are transported to the chromospheric network which forms a honeycomb-like pattern with horizontal size scales of $20\,000$ km or so.
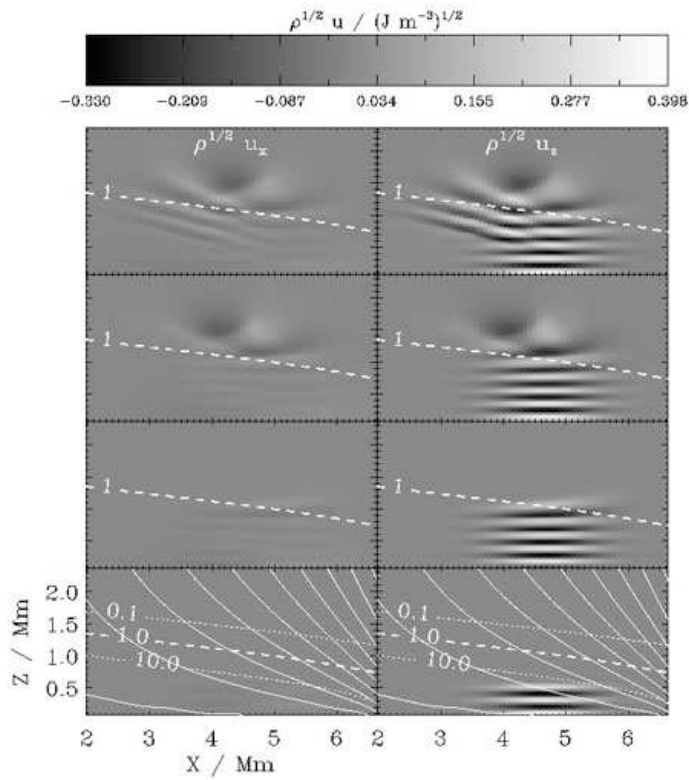
Fig. 8.7. Model results for of the horizontal (left panels) and vertical (right panels) velocities, scaled with the square root of the density. In this model, the atmosphere is a schematic isothermal chromosphere with magnetic field structure shown by the solid lines; plasma β contours are shown by the dashed lines in the lower panels. A fast mode (acoustic) wave is excited at the lower boundary by a vertically moving piston; its propagation is shown at four times, from bottom to top. The fast mode wave interacts with the magnetic field near $\beta = 1$ such that the wave is refracted and essentially reflected back into the photosphere and towards regions of high plasma β. See Rosenthal et al. (2002), and Bogdan et al. (2003).
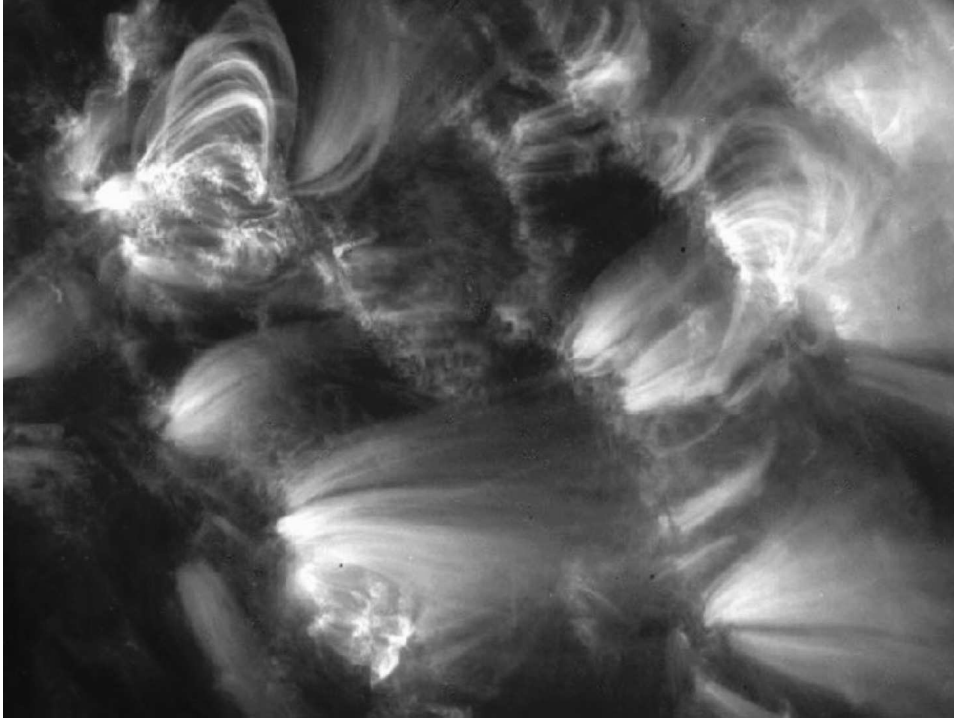
Fig. 8.8. The corona as seen by the TRACE telescope (TRACE is a satellite of the Stanford Lockheed Institute for Space Research, and part of the NASA Small Explorer program) in the 171 Å bandpass. The image shows plasma around 1 MK.
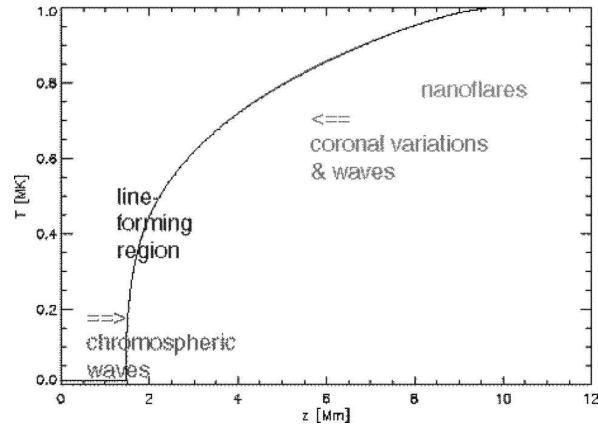
Fig. 8.9. Schematic stratification of the transition region between chromosphere and corona: A persisting conductive flux from the corona ensures that the temperature gradient must steadily increase with decreasing temperatures until other terms (*e.g.*, radiative losses) in the energy balance become significant. Optically thin spectral lines are formed over a relatively limited range in temperature and can therefore give good diagnostics of how the transition region responds to waves and other dynamic phenomena in the chromosphere below or the corona above.
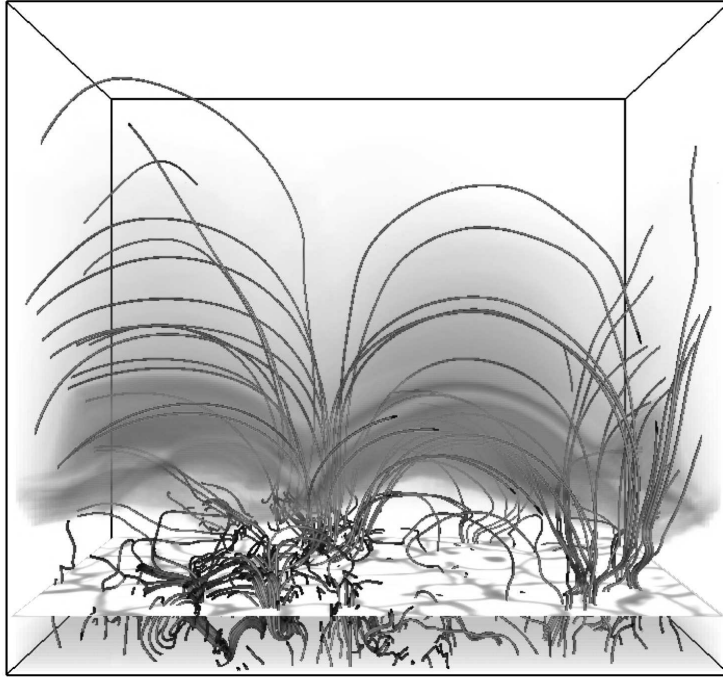
Fig. 8.10. The thermal structure and magnetic field of a 3D model as it has developed after an hour solar time evolution in a box of dimensions $16 \times 8 \times 16$ Mm. A horizontal slice of the temperature is shown near the photosphere, the shaded surface shows regions where the temperature is in the range 15 kK – 400 kK. Selected magnetic field lines are plotted. Convection zone and photospheric motions have deformed the originally quite simple potential field during the simulated hour. In the photosphere, the field is quickly concentrated in inter-granular lanes. In the middle to upper chromosphere β decreases below unity and the field expands to fill all space, constrained by its photospheric foot-points, forming loop-like structures. Note also that the field lines below the photosphere rarely breach the surface, rather they become quite tangled as a result of convective buffeting (see also the top panels in Fig. 1.2).
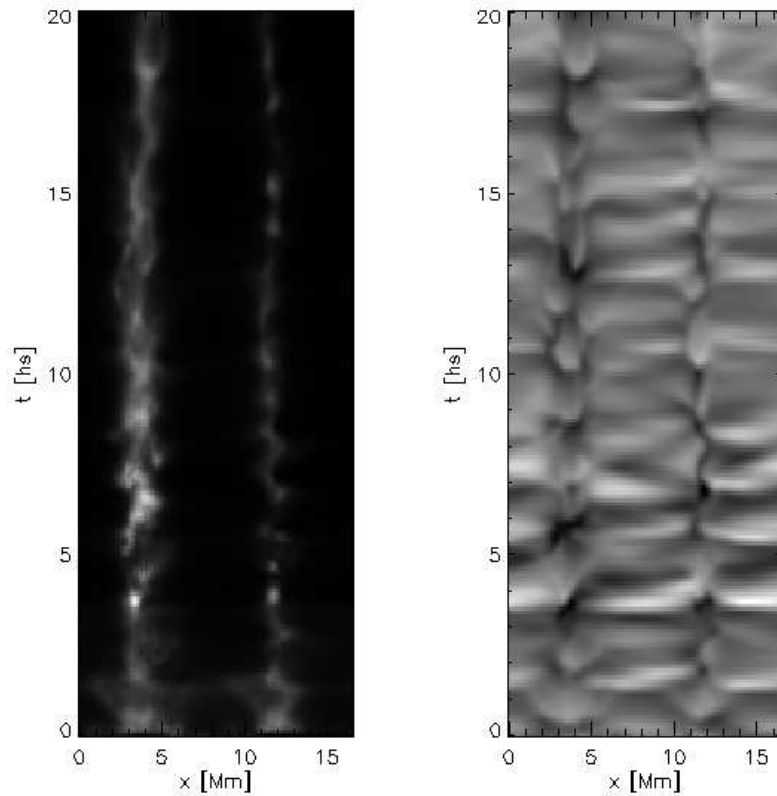
Fig. 8.11. Simulated observations of the O VI 103.2 nm line formed in regions where the temperature is roughly 300 kK. The left panel shows the total intensity in the line, the right panel shows the average Doppler shift. These simulated observations are based on a 2d MHD model spanning a region 16 Mm×10 Mm covering the convection to lower corona. The magnetic topology in this model is similar to that shown in Fig. 8.10: a "loop" with footpoints close to $x = 4$ Mm and $x = 12$ Mm. The periodic oscillations visible are mainly due to upward propagating waves generated in or below the photosphere.

9

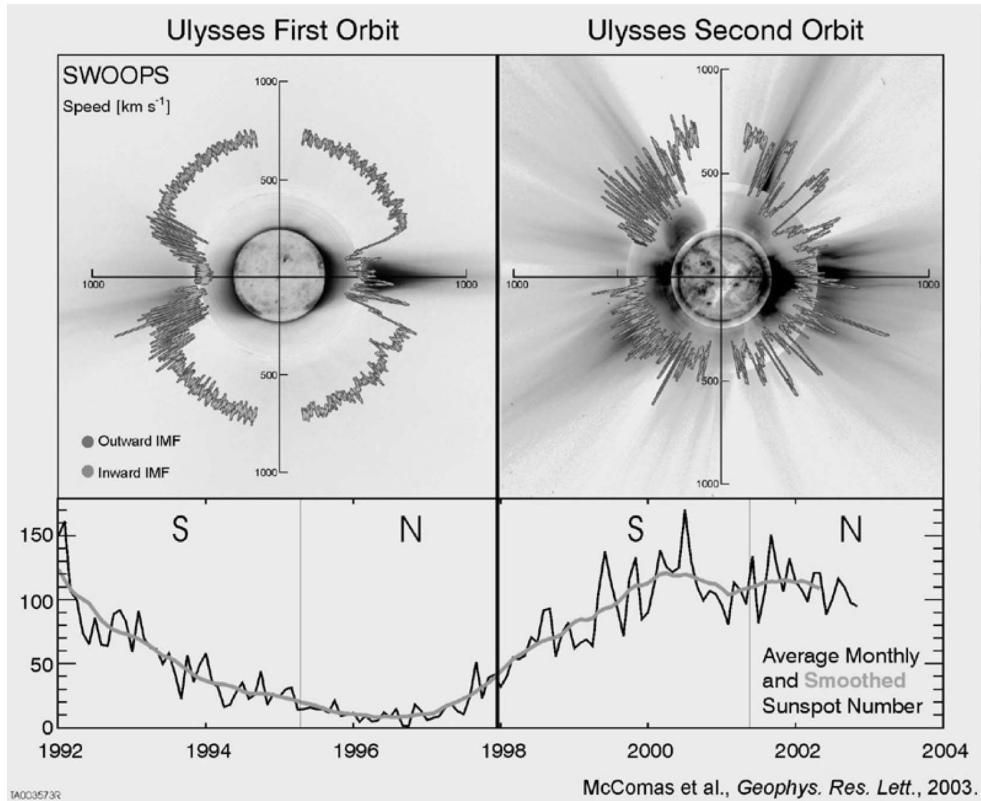# Stellar winds and magnetic fields

by Viggo H. Hansteen

Fig. 9.1. Polar plots of solar wind speed as a function of latitude for Ulysses' first two orbits. The solar wind speed data was obtained by the SWOOPS instrument (Solar Wind Observations Over the Poles of the Sun). The bottom panel shows the sunspot number over the period 1992–2003. The first orbit occurred through the solar cycle declining phase and minimum while the second orbit spanned solar maximum. (Taken from McComas *et al.*, **?**.)
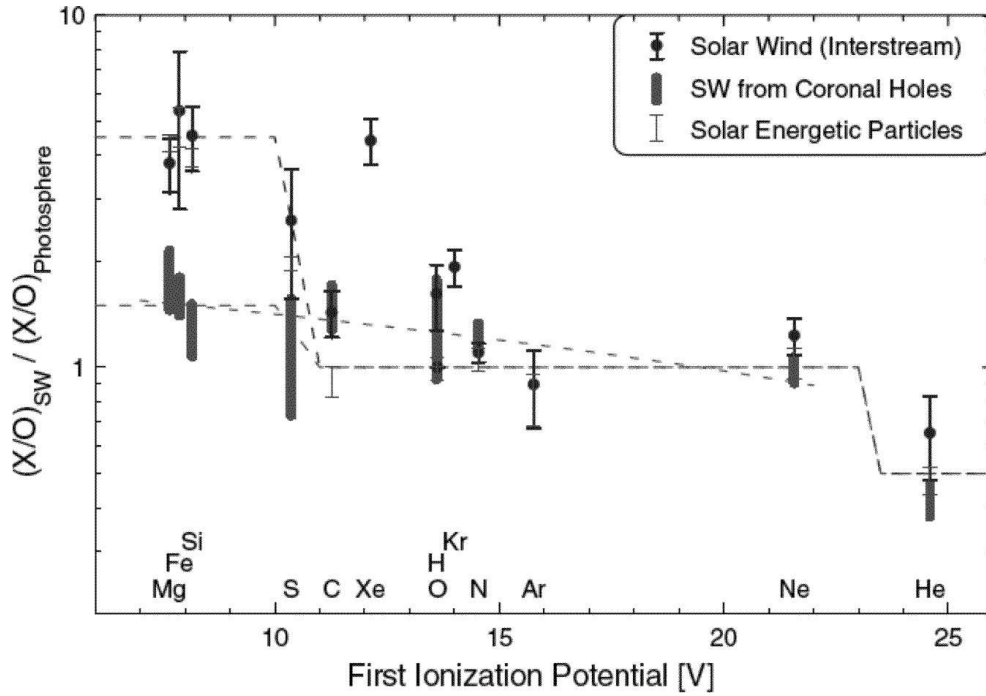
Fig. 9.2. Abundances of elements (relative oxygen) measured in the solar wind relative to their photospheric abundances (relative oxygen) as function of the elements first ionization potential (FIP). The dotted data points represent values typical of the slow solar wind (here called 'interstream' wind), the thick vertical lines represent values from the fast wind originating in coronal holes. The thin vertical lines represent data from solar energetic particles arising in flares and coronal mass ejections. Figure from Von Steiger and Murdin (**?**).
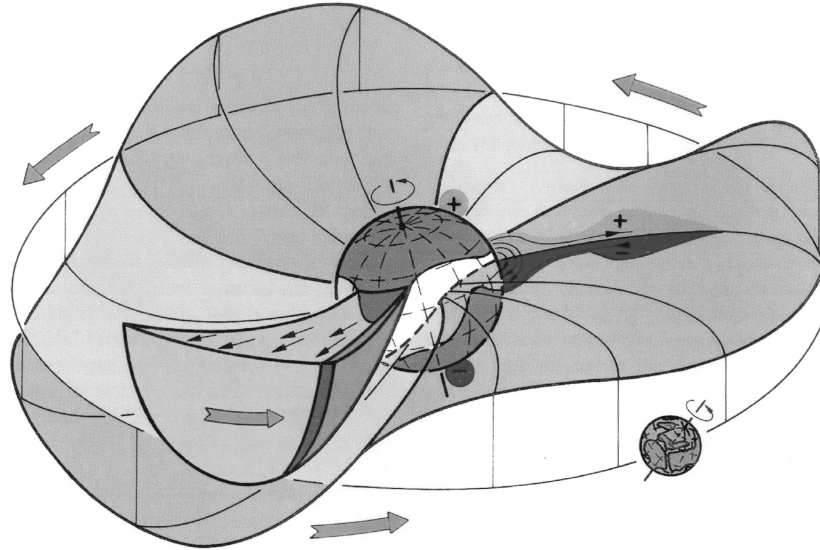
Fig. 9.3. The heliospheric current sheet forms a warped, undulating structure extending from the top ridge of the helmet streamer belt (cf., Figs. 1.3 [top] and 8.1) that sweeps by the Earth as the Sun rotates once per 27 days (synodic period). The magnetic field changes direction across the current sheet. (From Alfvén, 1977)
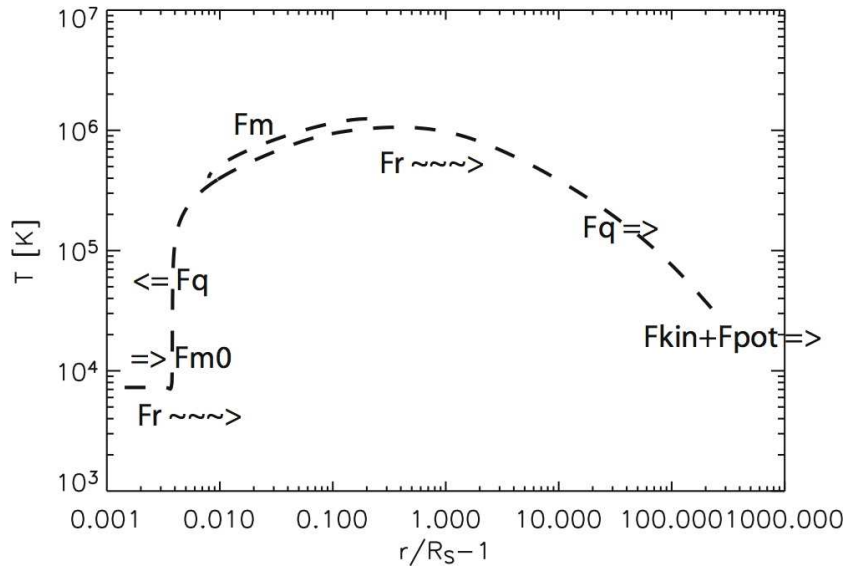
Fig. 9.4. Illustration of the solar wind energy budget from chromosphere to 1 AU. An input mechanical energy flux F_{m0} is introduced at the bottom boundary and is dissipated in the lower corona and out to some $r = 1.3\ R_S$. Some of this energy is conducted (F_q) back to the chromosphere, where it is radiated away (F_r), some is conducted outward and goes into the wind's kinetic and potential energy ($F_{kin} + F_{pot}$).
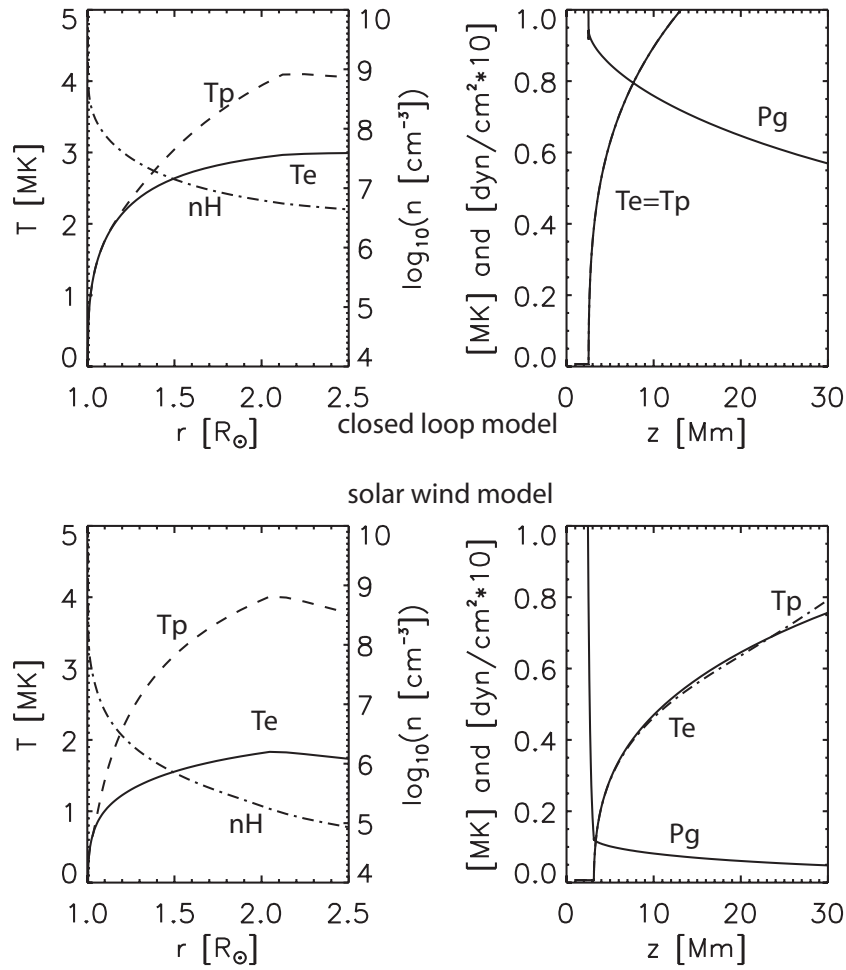
Fig. 9.5. Illustrative models for open and closed coronal field for heating at $2\,R_\odot$ with $H_{\rm m} = 0.1 R_\odot$. In the upper panels, the results of the closed model are shown: the left panel shows the proton temperature (dashed), the electron temperature (solid) and the total hydrogen density, *i.e.* neutral plus ionized (dash dotted). The right panel shows transition region details of the electron (solid) and proton (dashed) temperatures as well as the gas pressure p_g. The lower panels show the same variables for the open model.
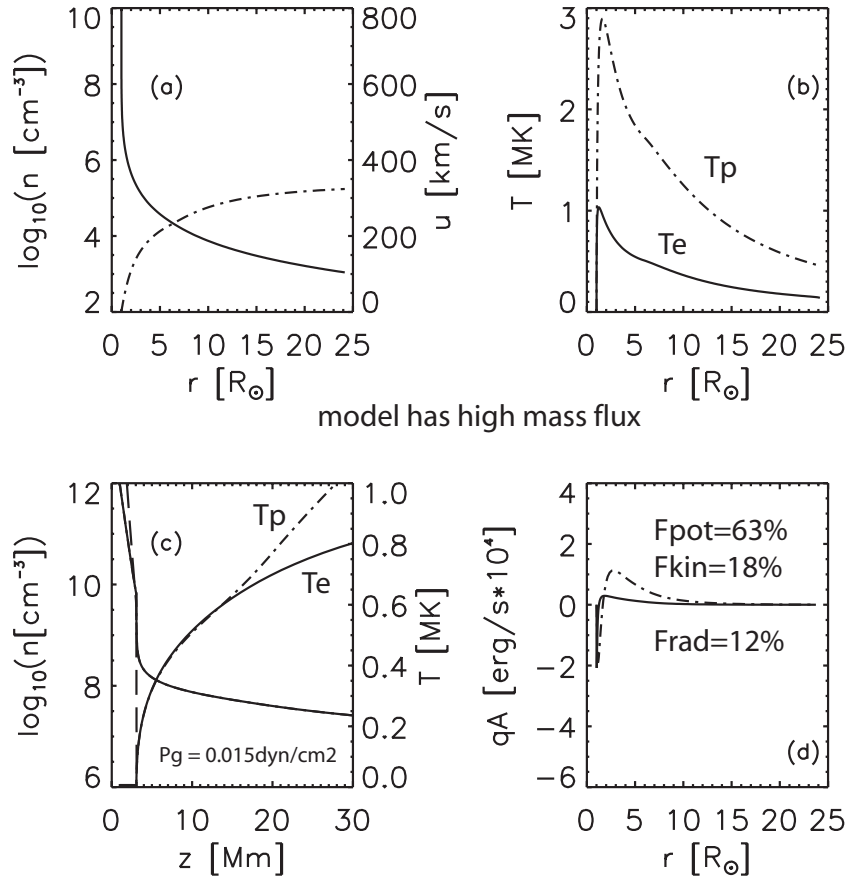
Fig. 9.6. Proton-electron solar wind model with heating close to the coronal base, roughly at $r_m = 1.1\ R_S$ and $H_m = 0.5\ R_\odot$. The top left panel shows the particle density (solid) and flow velocity (dash dotted), the top right panel shows the proton (dashed) and electron (solid) temperatures, the bottom left panel shows details of the neutral hydrogen (long dashed) and proton (solid) densities, as well as the electron (solid) and proton (dash dotted) temperatures in the upper chromosphere and transition region.
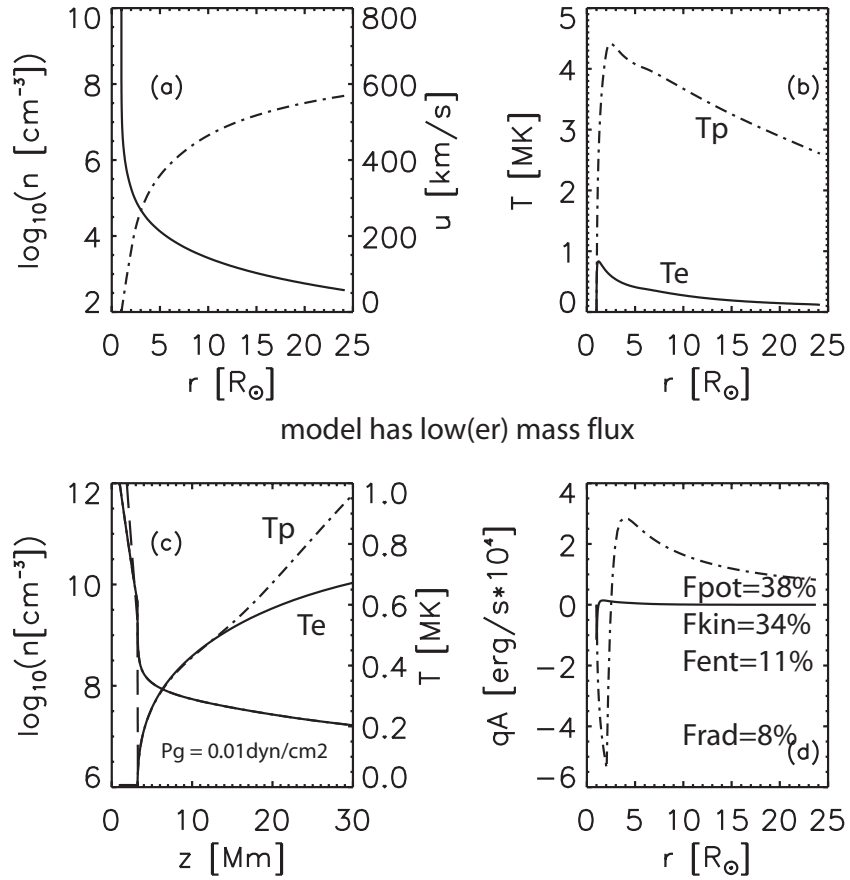
Fig. 9.7. Proton-electron solar wind model with heating far from the coronal base, roughly at $r_m = 2$ R_S and $H_m = 0.5$ $R_\odot$. The plots show the same variables as shown in Fig. 9.6.
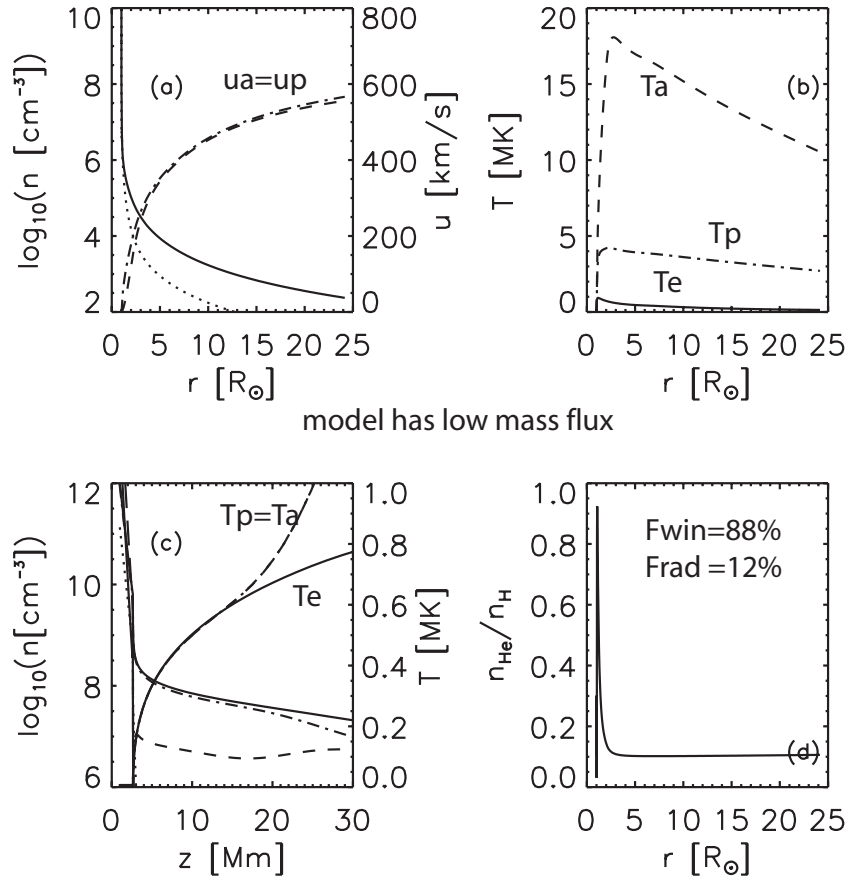
Fig. 9.8. Helium-hydrogen-electron solar wind model. The heating parameters are the same as those for the model shown in Fig. 9.7, but here 60% goes into heating the protons and 40% into heating α-particles, the energy is deposited roughly at $r_{\rm m} = 2\,R_{\rm S}$. The top left panel shows the total hydrogen (solid) and helium (dotted) densities and well as the proton (dash dotted) and α-particle (dashed) velocities, top right shows the electron (solid), proton (dash dotted) and α-particle (dashed) temperatures. The bottom left panel shows detail of the neutral hydrogen (long dashed), neutral helium (dotted), electron (solid), proton (dash dotted), and α-particle densities as well as the electron, proton and α-particle temperatures in the transition region and lower corona. The bottom right panel shows the helium abundance $n_{\rm He}/n_{\rm H}$ in the model.
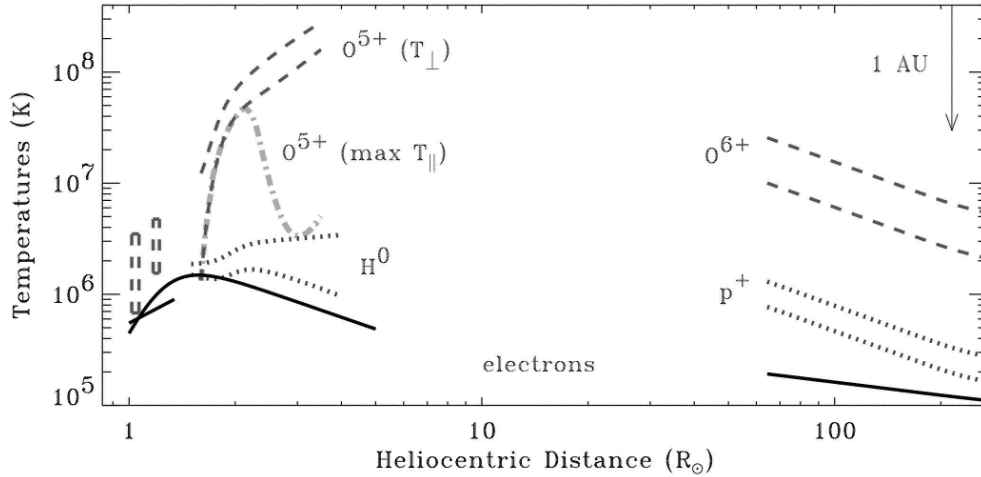
Fig. 9.9. Summary of the radial dependence of temperature in polar coronal holes and the fast wind at solar minimum: electron temperatures (solid), neutral hydrogen and proton temperatures (dotted), and ionized oxygen temperatures (dashed and dot-dashed). Paired sets of curves in the extended corona denote different empirical models derived from UVCS emission line properties. Dashed regions in the low corona ($r < 1.5R_S$) correspond to lower and upper limits on the O VI kinetic temperature from SUMER line widths. Figure from Kohl *et al.* (**?**).
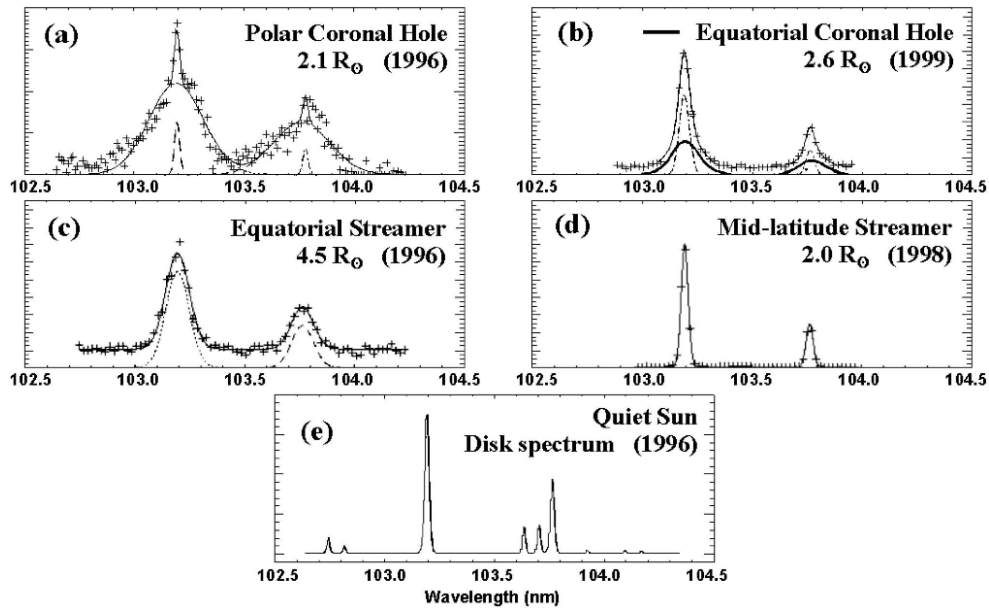
Fig. 9.10. (a)-(d) UVCS/SOHO observations of the O VI 103.2, 103.7 nm doublet in four types of coronal structure. (e) SUMER/SOHO observations of the quiet solar disk in the same range of the spectrum. Figure from Kohl *et al.* (**?**).
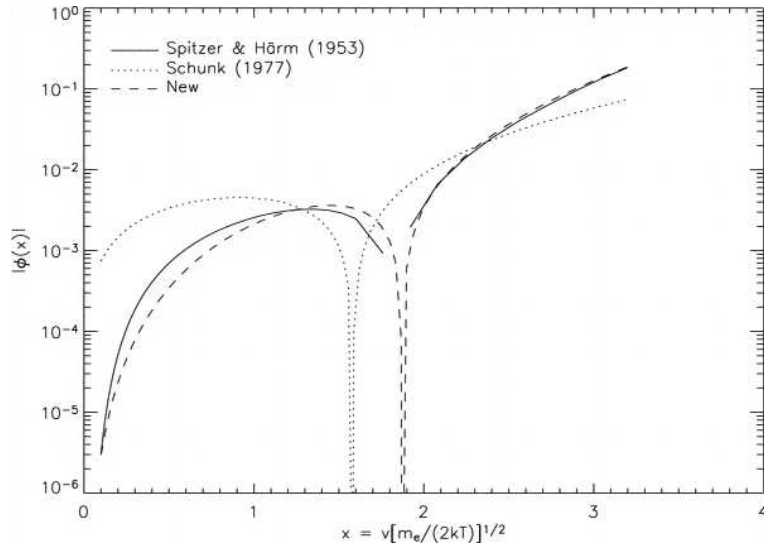
Fig. 9.11. Absolute value of the departure $\phi(x)$ (Eq. 9.51) from the Maxwellian for electrons as a function of velocity measured in units of $m_e/(2kT)^{1/2}$, such that the distribution function is written $f_s = f_{s0}(1 - \phi(u))$ where f_{s0} is the Maxwellian distribution. The solid line shows numerical solution produced by Spitzer and Härm (**?**) for electrons, the dotted line the commonly used solution derived by Schunk (**?**). The dashed line shows the result derived by Killie *et al.* (**?**), whence this figure is taken.

10

Fundamentals of planetary magnetospheres
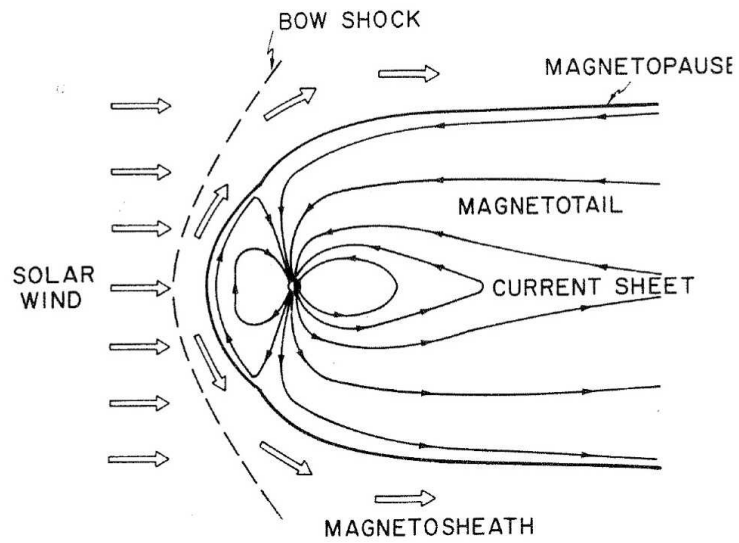
by Vytenis M. Vasyliūnas

Fig. 10.1. Schematic view of a magnetically closed magnetosphere, cut in the noon-midnight meridian plane. Open arrows: solar wind bulk flow. Solid lines within magnetosphere: magnetic field lines (direction appropriate for Earth).
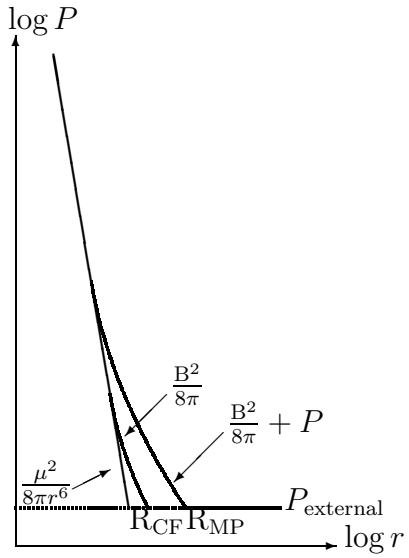
$\log P$

$\frac{B^2}{8\pi}$

$\frac{B^2}{8\pi} + P$

$\frac{\mu^2}{8\pi r^6}$

P_{external}

R_{CF} R_{MP}

$\log r$

Fig. 10.2. Variation of total pressure (magnetic plus plasma) with distance from the planet and its relation to the radial distance of the sub-solar magnetopause. Compared are the relationship in Eq. (10.1) to a schematic representation of a more realistic plasma-filled, non-dipolar planetary magnetic field.
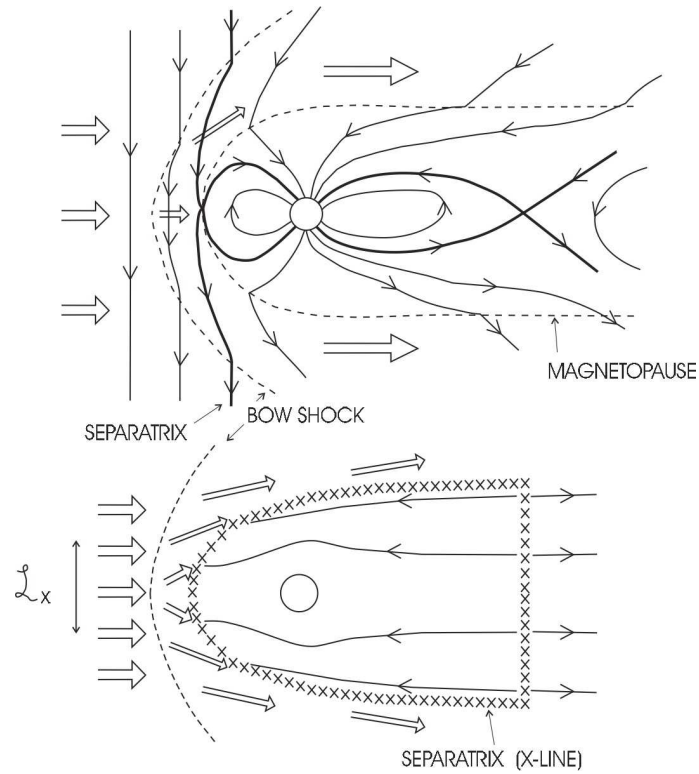
Fig. 10.3. Schematic representation of a magnetically open magnetosphere. Top: cut in noon-midnight meridian plane; thick lines are magnetic field lines within the separatrix surfaces separating open from closed or open from interplanetary field lines; other conventions same as in Fig. 10.1. Bottom: cut in equatorial plan; a line of × symbols represents intersection with the two branches of the separatrix (compare with Fig. 4.3 for the hypothetical case with zero wind speed); solid lines are streamlines of magnetospheric plasma flow, and $\mathcal{L}_X$ represents the projection of the dayside magnetic reconnection region along streamlines into the solar wind (see Sect. 10.4.3).
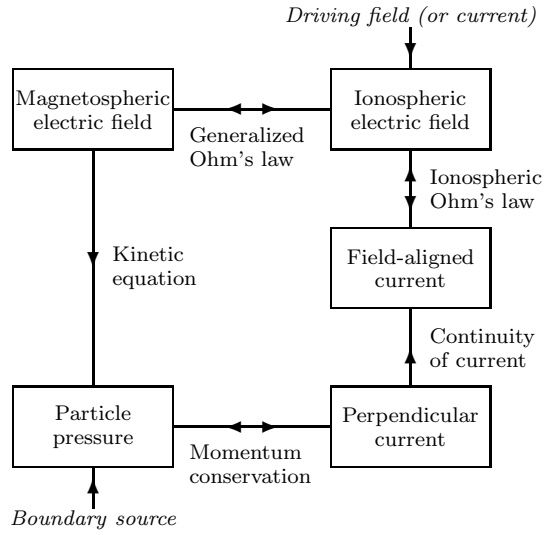
Driving field (or current)

```
┌─────────────────┐              ┌─────────────────┐
│  Magnetospheric │ ←────────→   │   Ionospheric   │
│  electric field │              │  electric field │
└─────────────────┘  Generalized └─────────────────┘
                     Ohm's law
                                         Ionospheric
        Kinetic                          Ohm's law
        equation                  ┌─────────────────┐
                                  │  Field-aligned  │
                                  │     current     │
                                  └─────────────────┘

                                         Continuity
                                         of current
┌─────────────────┐              ┌─────────────────┐
│    Particle     │ ←────────→   │  Perpendicular  │
│    pressure     │              │     current     │
└─────────────────┘  Momentum    └─────────────────┘
                     conservation
```

Boundary source

Fig. 10.4. Schematic diagram of magnetosphere-ionosphere coupling calculations (after **?**, **?**).
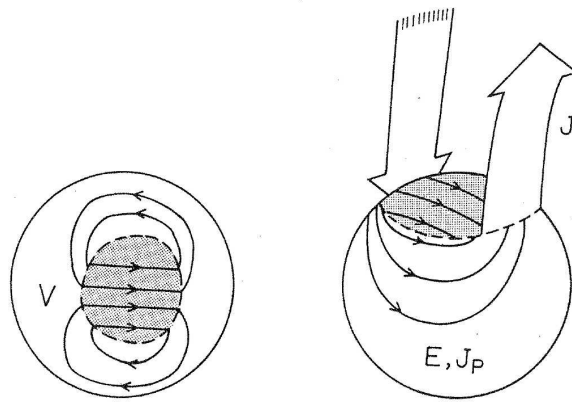
Fig. 10.5. Schematic diagram of magnetospheric convection over the Earth's north polar region (after **?**, **?**). Left: streamlines of the plasma bulk flow (the Sun is towards the left). Right: Electric field lines and associated Pedersen currents, and sketch of the magnetic-field aligned (a.k.a. Birkeland) current (large arrows). See Section 10.4.3 for a detailed description and Sect. 11.6 and Fig. 11.9 for corresponding MHD model results for the electric potential. For a schematic representation of magnetospheric convection throughout the magnetosphere, see Fig. 13.4.
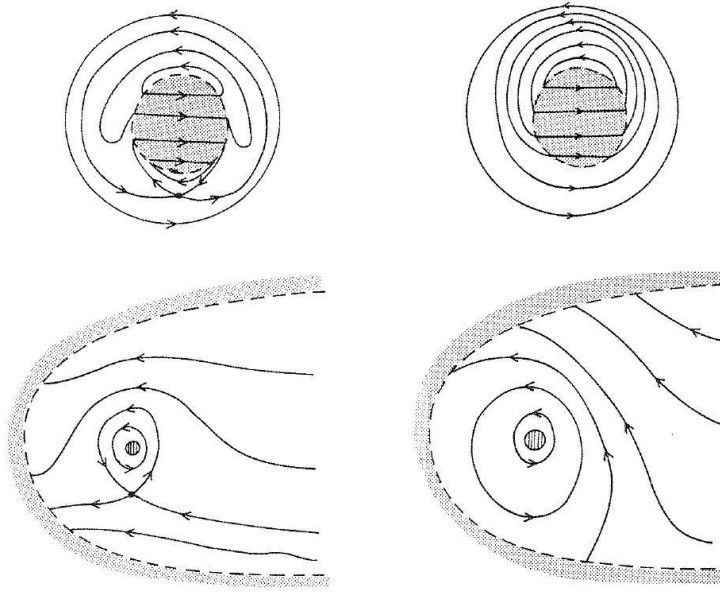
Fig. 10.6. Streamlines of plasma flow in a magnetosphere: (top) looking down on the topside ionosphere, and (bottom) projected along magnetic field lines to the equatorial plane of the magnetosphere. Left: magnetospheric convection dominant. Right: corotation dominant (after **?**, **?**; compare with the observation-based model for Jupiter's magnetospheric field in Fig. 13.6).
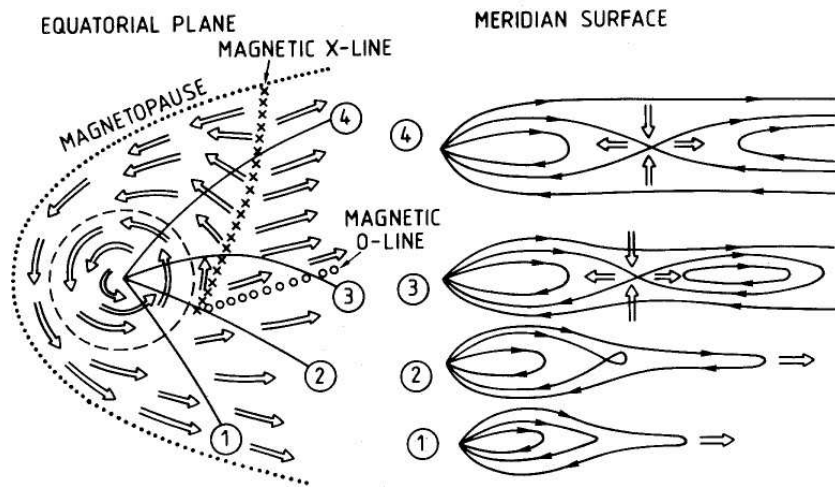
Fig. 10.7. Sketch of planetary wind flow and magnetic topology (after **?**, **?**).
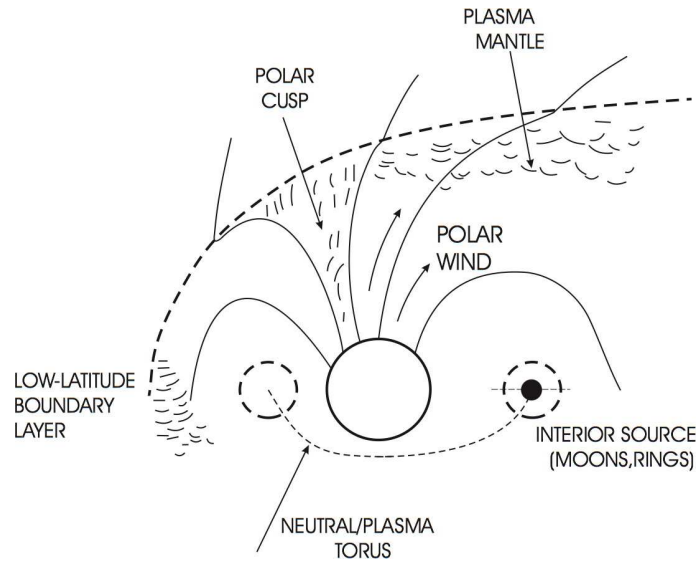
Fig. 10.8. Sketch of magnetospheric plasma source locations (not to scale, schematic, only northern hemisphere shown). See Fig. 13.3 for a diagram for Earth's magnetosphere in particular.

$S/\left(\pi\rho_{\mathrm{sw}}\,v_{\mathrm{sw}}\,\mathrm{R_{MP}}^{2}\right)$
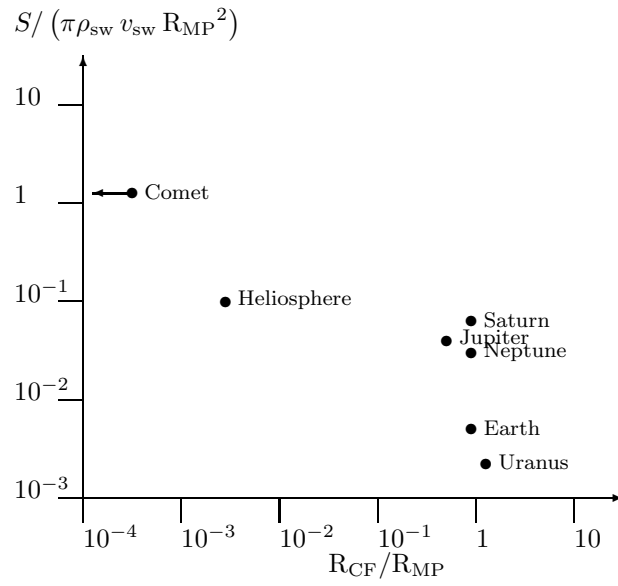
Fig. 10.9. Normalized interior mass source vs. $R_{\mathrm{CF}}/R_{\mathrm{MP}}$. Parameter values mostly taken from Ch. 13. Values for a comet and for the heliosphere are only very rough estimates. R_{CF} for the Sun (admittedly a somewhat artificial concept) calculated by balancing a dipole field with 1 Gauss at the solar surface against an interstellar pressure that stops the solar wind at ~ 100 AU.

11

Solar-wind magnetosphere coupling: an MHD perpective

by Frank R. Toffoletto and George L. Siscoe
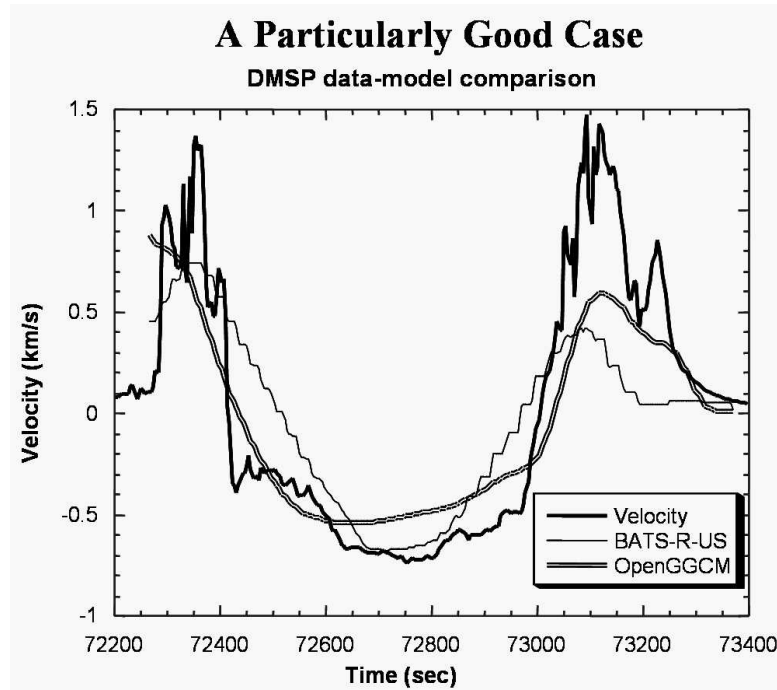
Fig. 11.1. A comparison between measured (DMSP) and computed (BATS-R-US and OpenGGCM) ionospheric plasma velocities over the polar cap prepared as part of a space-weather metrics campaign.
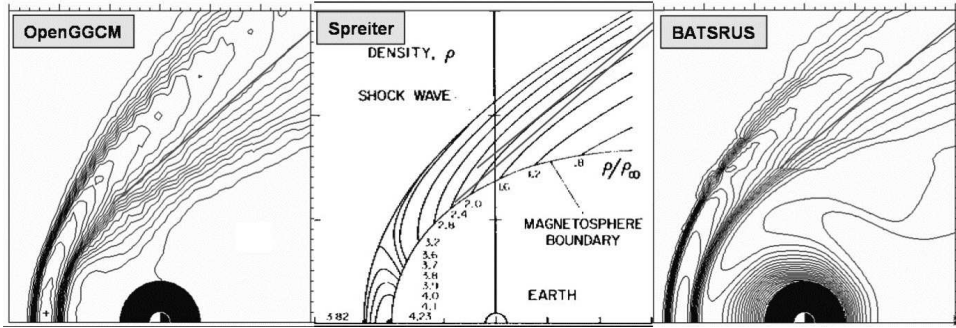
Fig. 11.2. A comparison of the density contours between the two MHD simulation codes and the Spreiter analytic model. Upstream solar wind conditions are the same for the simulations (solar wind speed 400 km/s, density 5 protons/cm^3, temperature 232100 K, IMF 0 nT) and similar to those used to make the Spreiter contours. The straight line segments lie parallel to the x2 density contour which marks where the density in the magnetosheath is twice that in the solar wind.
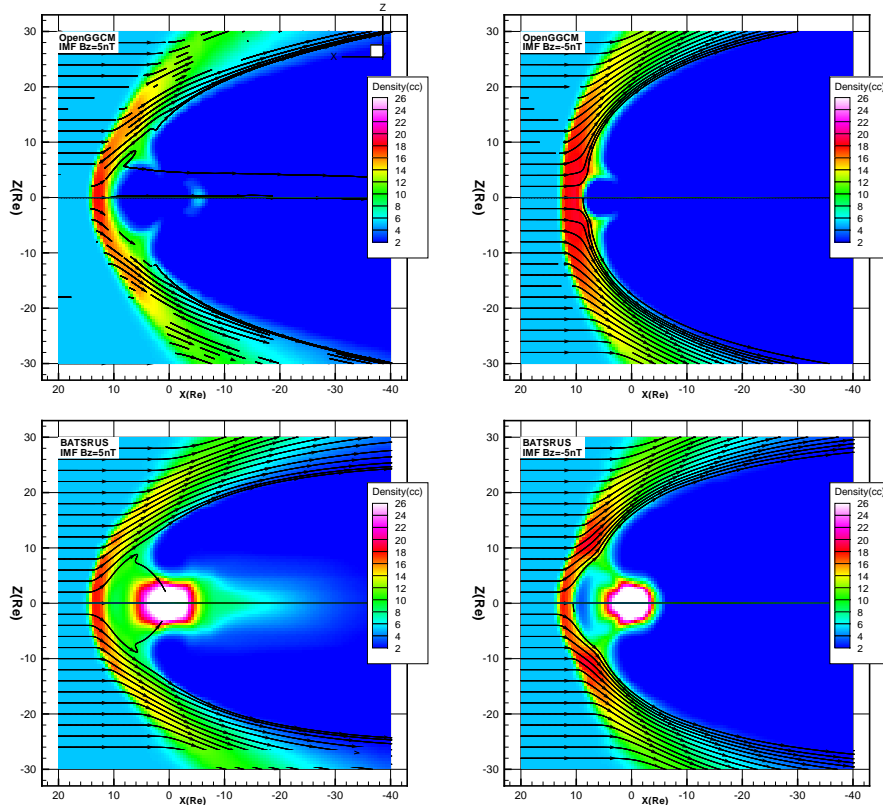
Fig. 11.3. The computed densities and flow streamlines in the noon-midnight plane obtained from from the OpenGGCM (top) and the BATS-R-US (bottom) global MHD codes for the cases when the IMF B_z is 5nT northward (left) and B_z is 5 nT southward. The black lines represent flow streamlines.
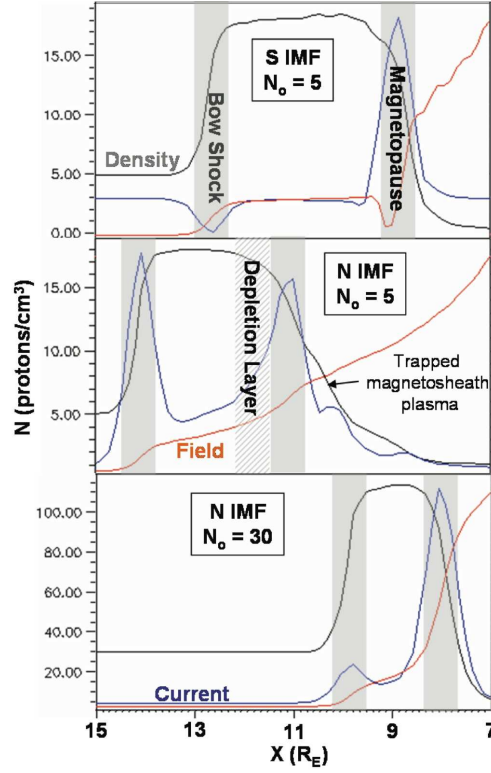
Fig. 11.4. Plots of number density (black), magnetic field strength (red), and electric current (y-component) (blue) along the stagnation streamline for (IMF, N_O)= (S,5), (N,5), and (N,30), respectively, where N, and S stand for northward, southward, and N_0 for the upstream density (cm^{-3}), respectively. The solar wind speed is 400 km/s, the temperature 232100 K in each case. Solid shadings identify the bow shock and magnetopause; striped shading, the depletion layer. (OpenGGCM)
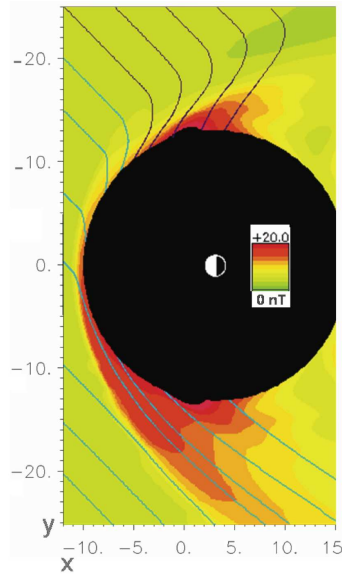
Fig. 11.5. Field strength and field lines in the equatorial magnetosheath for a Parker-spiral interplanetary magnetic field (BATSRUS) seen from above the Earth's north pole with the Sun to the left.
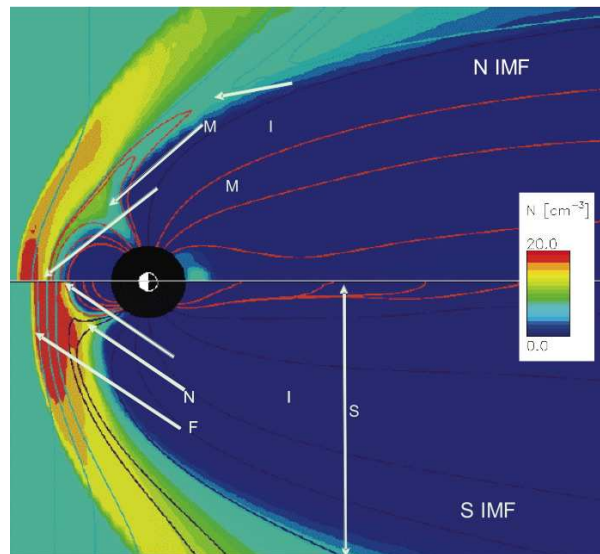
Fig. 11.6. The basic structural elements of the magnetosphere as depicted in global (OpenGGCM) MHD simulations can be seen here outlined in density contours and magnetic field lines: bow shock, magnetosheath, magnetopause, dayside cusps, closed field lines (top), open field lines (bottom), and magnetotail. The figure identifies contrasts between the magnetosphere as shaped under northward (top) and southward (bottom) IMF conditions. Solar wind conditions are the same in both halves of the figure except for the IMF direction.
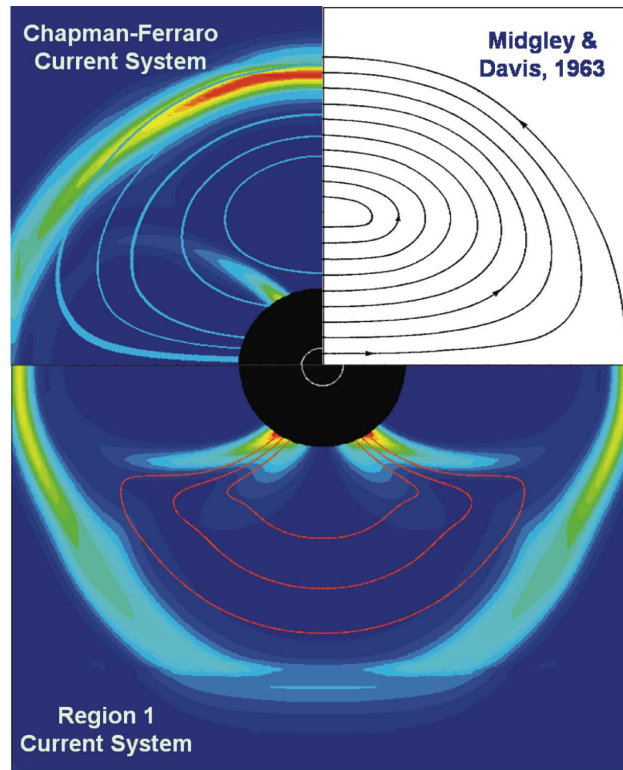
Fig. 11.7. MHD simulations (BATSRUS) showing color contours in the $x = 0$ plane (which contains the terminator) of current density and current streamlines of the Chapman-Ferraro current system (zero IMF) (top half) and the region-1 current system (95 nT southward IMF) (bottom half). Chapman-Ferraro current streamlines from the analytical calculation of **?, ?** shown for comparison. Solar wind speed is $400 \, \text{km/s}$, density $5 \, \text{cm}^{-3}$, and temperature $232 \, 100 \, \text{K}$.
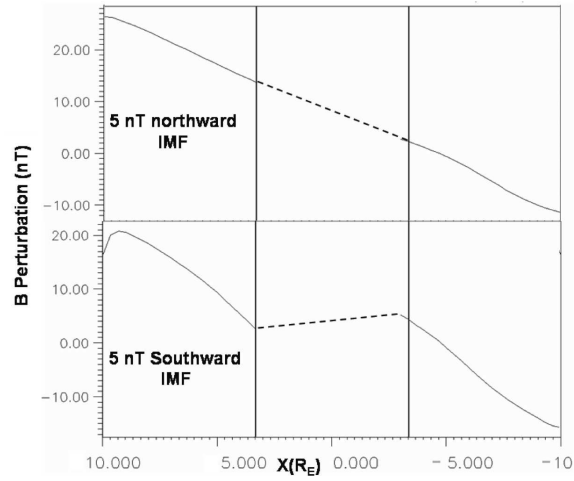
Fig. 11.8. Perturbation magnetic field along the x-axis for northward IMF (top) and southward IMF (bottom). Dashed lines connect computed values across the no-compute zone from $3.5\,R_{\mathrm{E}}$. Solar wind speed: 400 km/s, density: $5\,\mathrm{cm}^{-3}$; temperature $232100\,\mathrm{K}$. (BATSRUS)
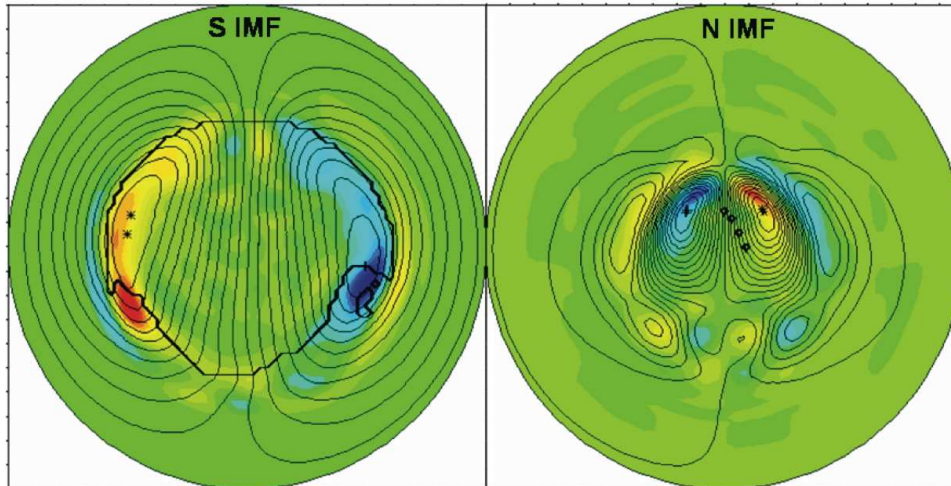
Fig. 11.9. Contours of electrical potential from the OpenGGCM model on northern-hemisphere polar plots (noon towards the top). The background color images show parallel (region-1) current for 5 nT southward IMF (left) and 5 nT northward IMF (right). Other solar wind parameters are as before. The trans-polar voltages are 150 kV (left) and 26 kV (right). The range on the color contour scales is the same in both figures (minus (red) to plus (blue) $1.6 \, \mu A/m^2$). The latitude range extends from $50°$ (outer edge) to $90°$ (center). The black closed contour in the left panel marks the border between open and closed field lines. Compare with the schematic diagram in Fig. 10.5 that shows the corresponding plasma flow (right) and electric field lines (left; the corresponding perspective in this figure is from the upper-left corner) for the case with southward IMF.
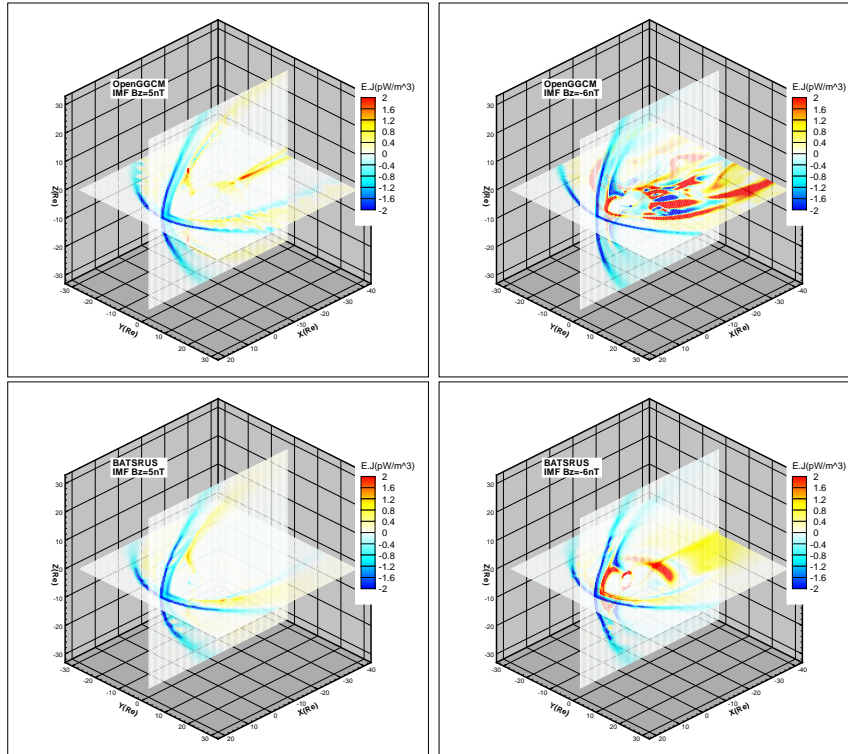
Fig. 11.10. Values of $\vec{j} \cdot \vec{E}$ in the noon-midnight meridian and equatorial planes computed by the OPENGGCM (top) and BATS-R-US (bottom) MHD codes

12

On the ionosphere and chromosphere

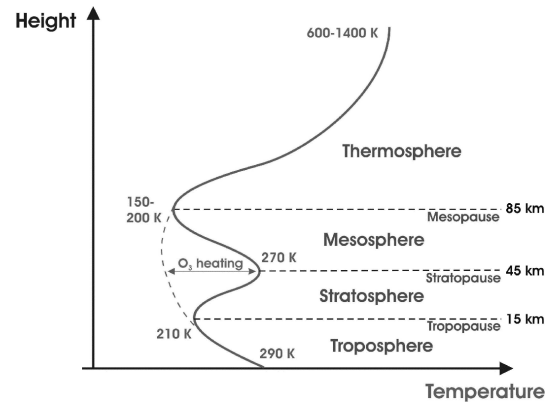*by Tim Fuller-Rowell and Carolus J. Schrijver*

Fig. 12.1. Average vertical temperature profile through Earth's atmosphere. The general shape of the temperature profile is reasonably consistent to the point where it can be used to define the four main neutral atmosphere "layers", from the troposphere to the thermosphere. The temperature of the upper most layer, the thermosphere, increases steeply with altitude due to absorption of solar extreme ultraviolet (EUV) and far ultraviolet (FUV) radiation. The thermosphere and upper mesosphere are partially ionized by the same EUV radiation, which varies by a factor of three over the solar cycle, and by auroral particle precipitation.
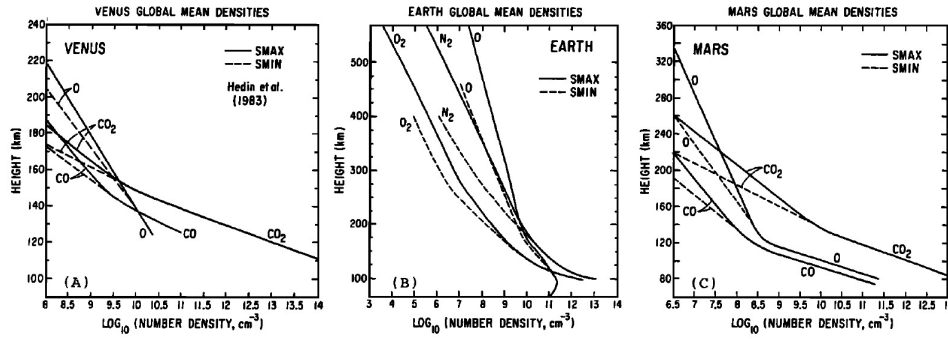
Fig. 12.2. Comparison of the global mean vertical profiles of the major species in the neutral upper atmospheres of a) Venus, b) Earth, and c) Mars for low and high solar activity (from Bougher and Roble, 1991). SMIN and SMAX indicate solar minimum and maximum conditions. Note that the turbopause heights (where turbulent mixing and diffusive separation are comparable) are 135, 110, and 125 km for Venus, Earth, and Mars, respectively.
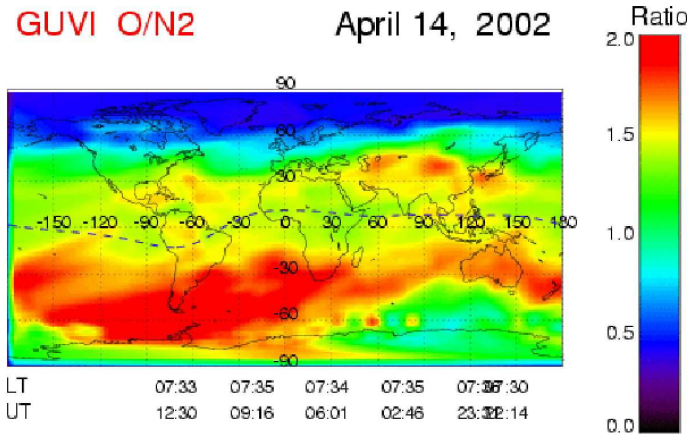
Fig. 12.3. Global distribution of the column integrated ratio of atomic oxygen and molecular nitrogen across the middle and upper thermosphere from observations of the GUVI instrument on the TIMED satellite (Paxton et al., 1999). For this April season the global circulation is already more solstice like, which produces the low values in the northern "summer" high latitudes and a maximum in the southern "winter" hemisphere. The shift of the peak in the southern hemisphere from polar to winter mid-latitudes is due to the competition in the between the solar driven circulation and that driven by the high latitude magnetospheric source of heat.
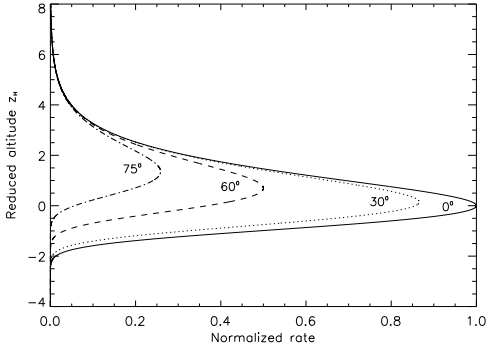
Fig. 12.4. Shape of the vertical profile of the classical Chapman profile appropriate for heating, ionization, and dissociation in a stratified hydrostatic atmosphere.
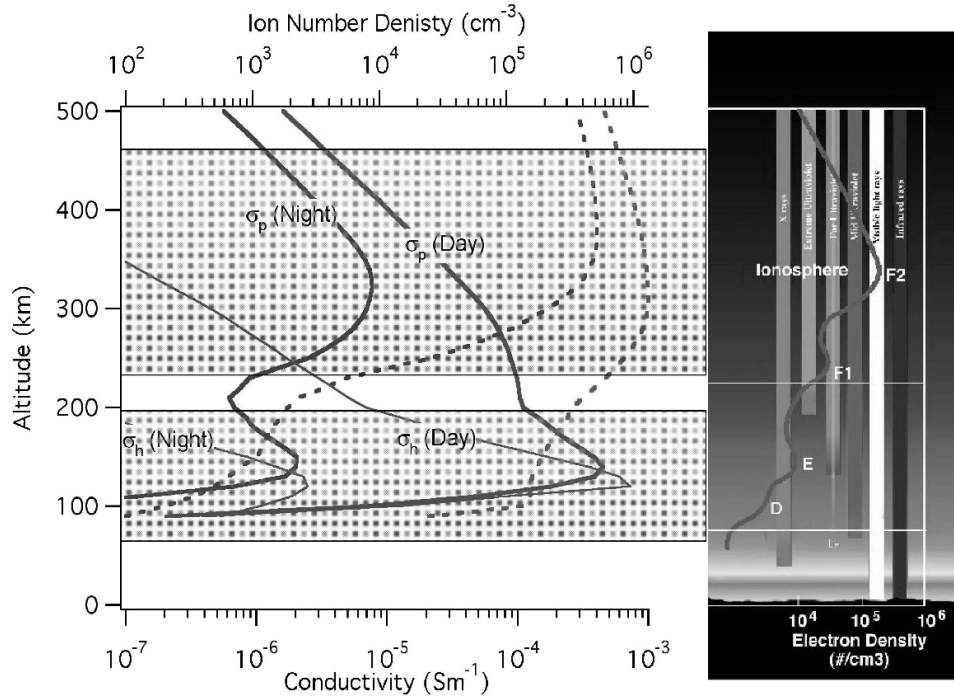
Fig. 12.5. Typical vertical profiles of the ion number density and Pedersen and Hall conductivities for day and night conditions. Peak plasma densities, in the F2 layer, are around 300 km altitude (from Heelis, 2004). Also shown are the atmospheric penetration depths of various wavelengths of solar radiation from X-rays to infrared.
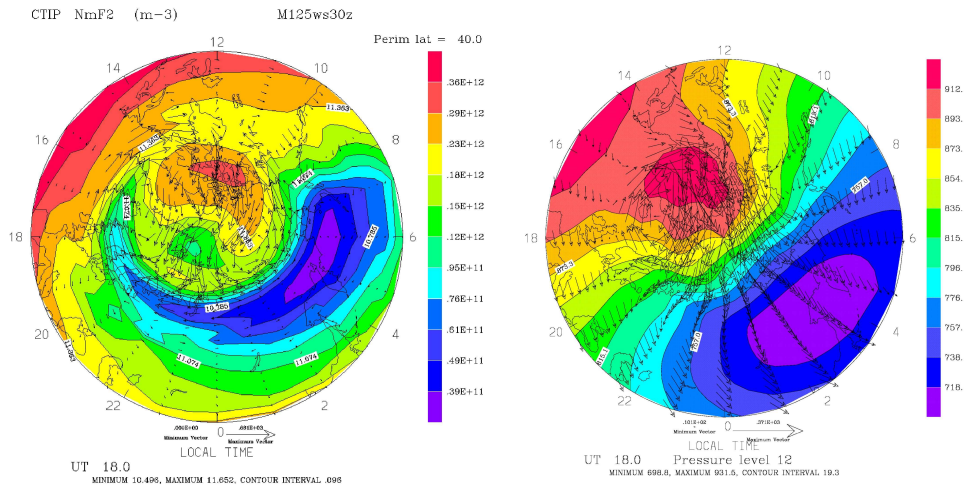
Fig. 12.6. Left panel: Simulation of plasma drift and electron density at the altitude of the F-region peak in the upper thermosphere for moderate geomagnetic activity (Kp∼ 3). The region poleward of 40 latitude is shown at 18 UT. Right panel: Neutral wind and temperature over the same region at 300 km altitude in response to the to plasma drift. The maximum plasma drift velocity is ∼700 m/s, and the peak wind speed is ∼380 m/s.
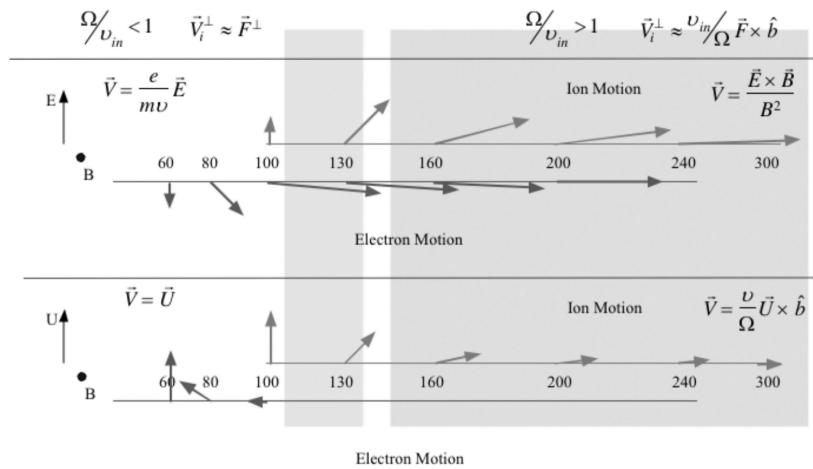
Fig. 12.7. Approximate values of the magnitude and direction of the ion and electron drifts produced by the direct action of neutral winds and electric fields. The approximate locations of the E- and F-regions are shaded (from Heelis, 2004).
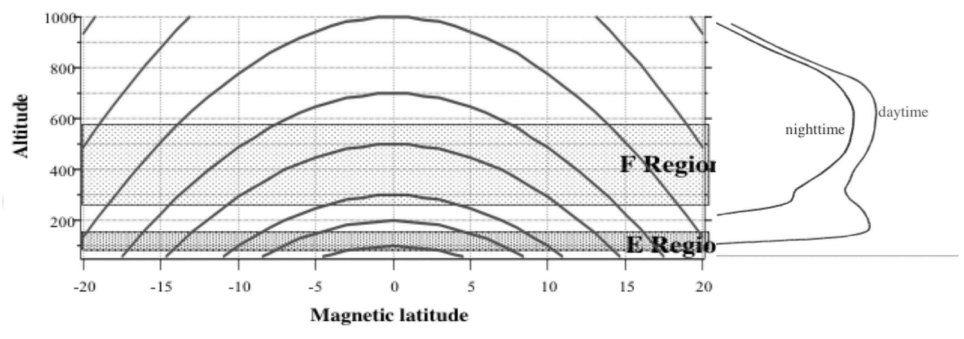
Fig. 12.8. Shape of the magnetic field at mid and low latitudes in Earth's atmosphere, which gives rise to its unique electrodynamic properties (from Heelis, 2004).
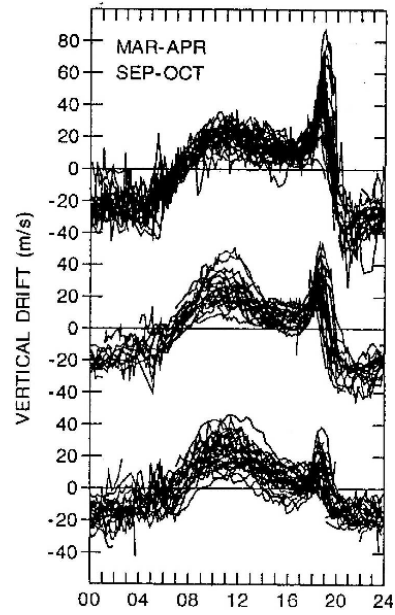
Fig. 12.9. Diurnal variation and day-to-day variability of the vertical plasma drift at Jicamarca, Peru on the magnetic equator at equinox at low, mid, and high solar activity (from bottom to top). The drift is upward by day downward by night, and punctuated by a strong post-sunset pre-reversal enhancement in the upward drift (from Fejer and Scherliess, 1997).
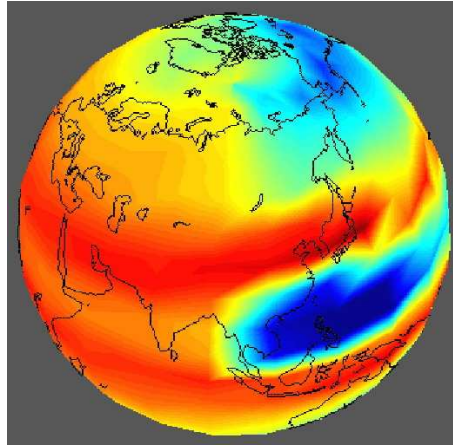
Fig. 12.10. Global structure of the F-region plasma density showing the equatorial ionization (or Appleton) anomaly about 15° latitude on either side of the magnetic equator. From a numerical simulation using a coupled thermosphere, ionosphere, plasmasphere model with self consistent mid and low latitude electrodynamics.
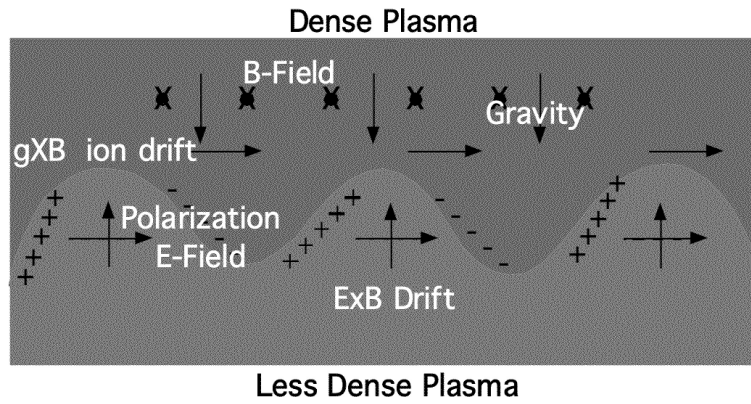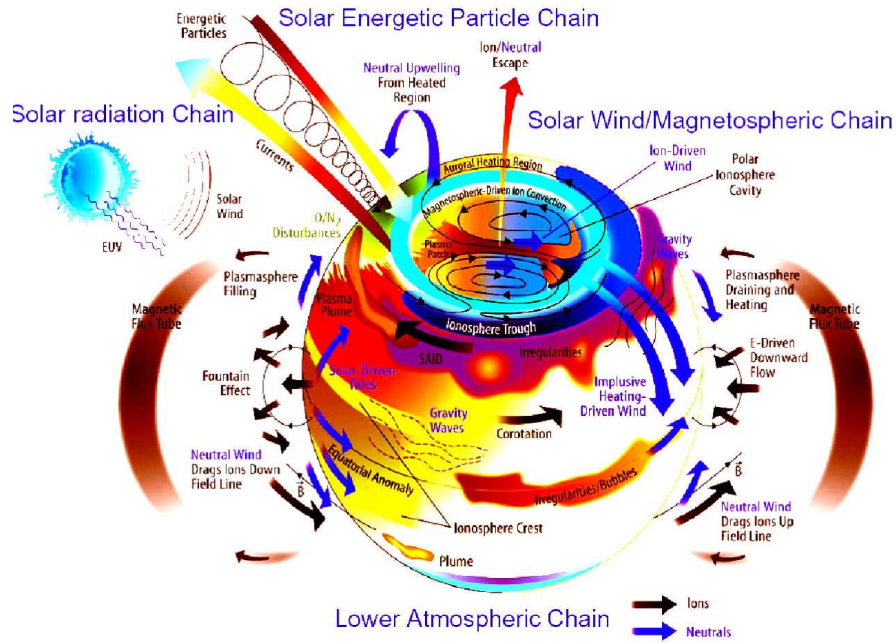
Fig. 12.11. Polarization fields and associated $\mathbf{E} \times \mathbf{B}$ drifts in the F-region resulting from perturbations in the conductivity in the presence of the gravitationally driven ion current (from Heelis, 2004).

Fig. 12.12. Indication of the complexity of the ionosphere-thermosphere-mesosphere (ITM) system and the range of physical processes operating. This chapter has touched briefly on just a few of the physical profiles behind this complexity.
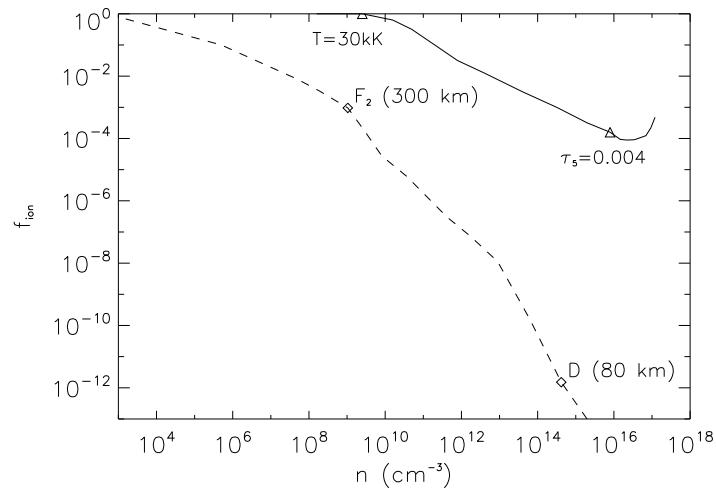
Fig. 12.13. Comparison of densities, n (cm^{-3}), and ionization fractions, $f_{\rm ion}$, for a characteristic dayside ionosphere (dashed) and mean chromosphere solid. The diamonds mark the mean values for the ionospheric D and F$_2$ regions, centered on about 80 km and 300 km, respectively. The triangles denote the base of the chromosphere (defined here as at a continuum optical depth of $\tau_5 = 0.004$) and the top of the chromosphere (where the temperature exceeds 30 000 K). Data from Allen's *Astrophysical Quantities* (1972).

13

Comparative planetary environments

by Fran Bagenal
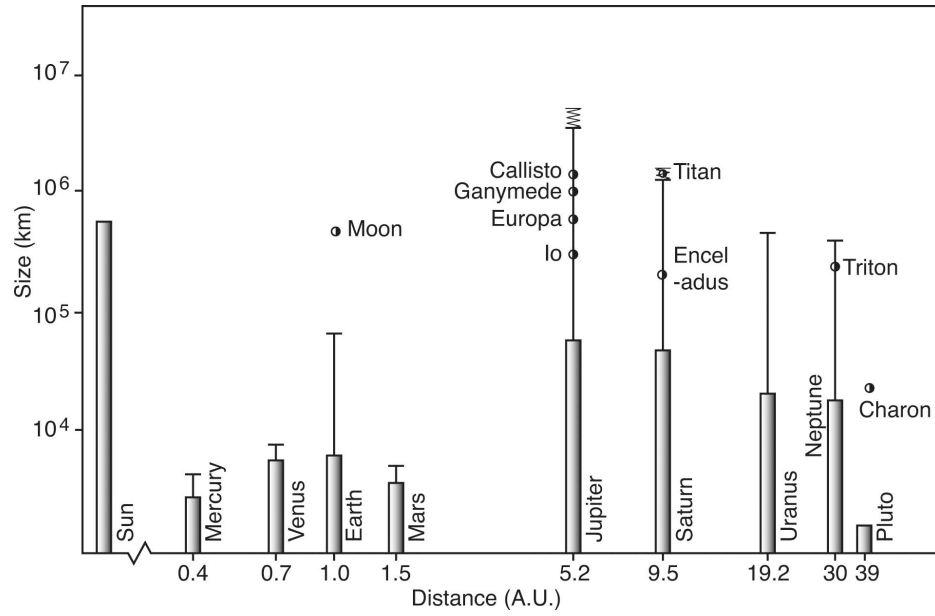
Fig. 13.1. A logarithmic plot of size of object vs. distance from the Sun for the planets (solid bars), their magnetospheres (thin bars) and the orbital radii of their primary moons. The range in sizes of the magnetospheres of Jupiter and Saturn are shown by the zig-zag lines.
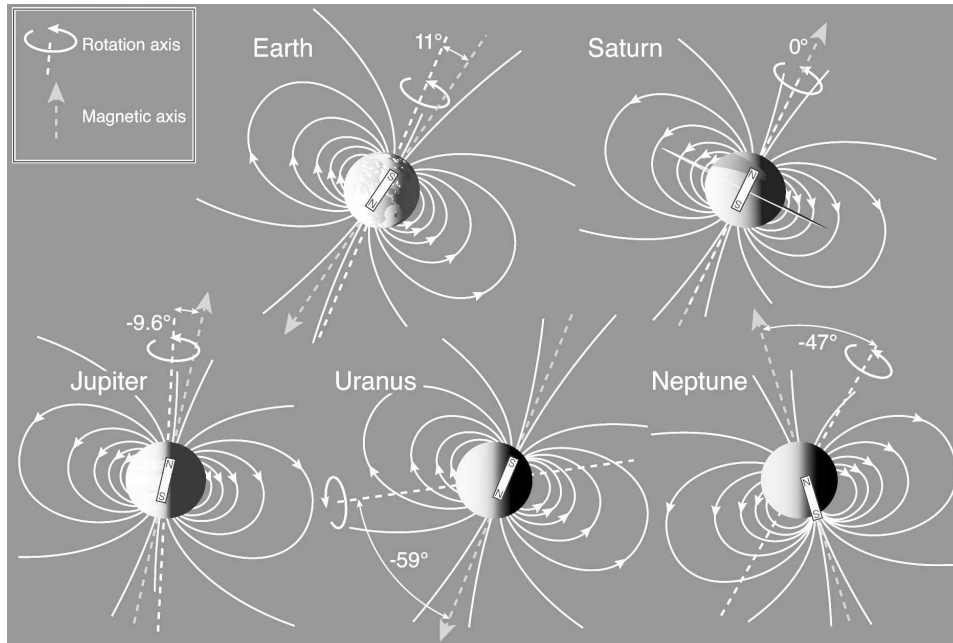
Fig. 13.2. The tilt angles between the spin and magnetic axes are shown for the five main magnetized planets. Considering the horizontal direction of the diagram to be parallel to the ecliptic plane and the vertical direction the ecliptic normal, then the spin axis is shown for conditions of maximum angle from the ecliptic normal (*i.e.*, at solstice). Each planet's magnetic field can be approximated as a dipole where the orientation and any offset from the center of the planet is illustrated by a bar magnet located at the center of the dipole.
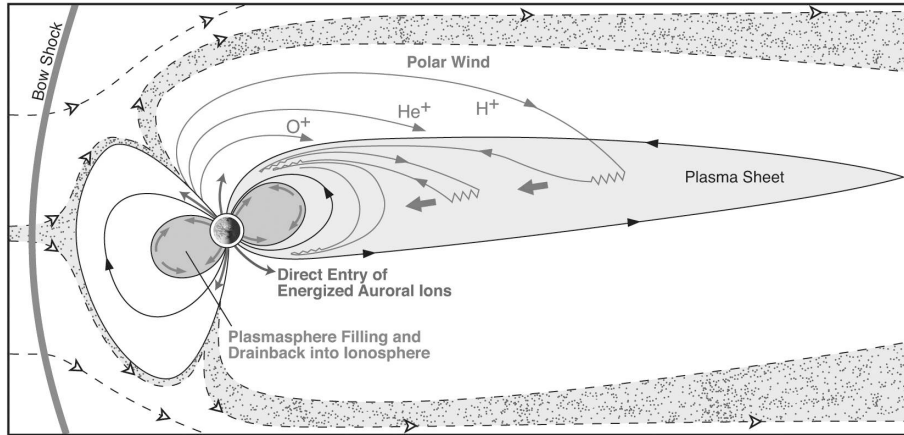
Fig. 13.3. Sources of plasma for the Earth's magnetosphere (after Chappell, 1988). The shaded, dotted area illustrates the boundary layer through which solar wind plasma enters the magnetosphere.
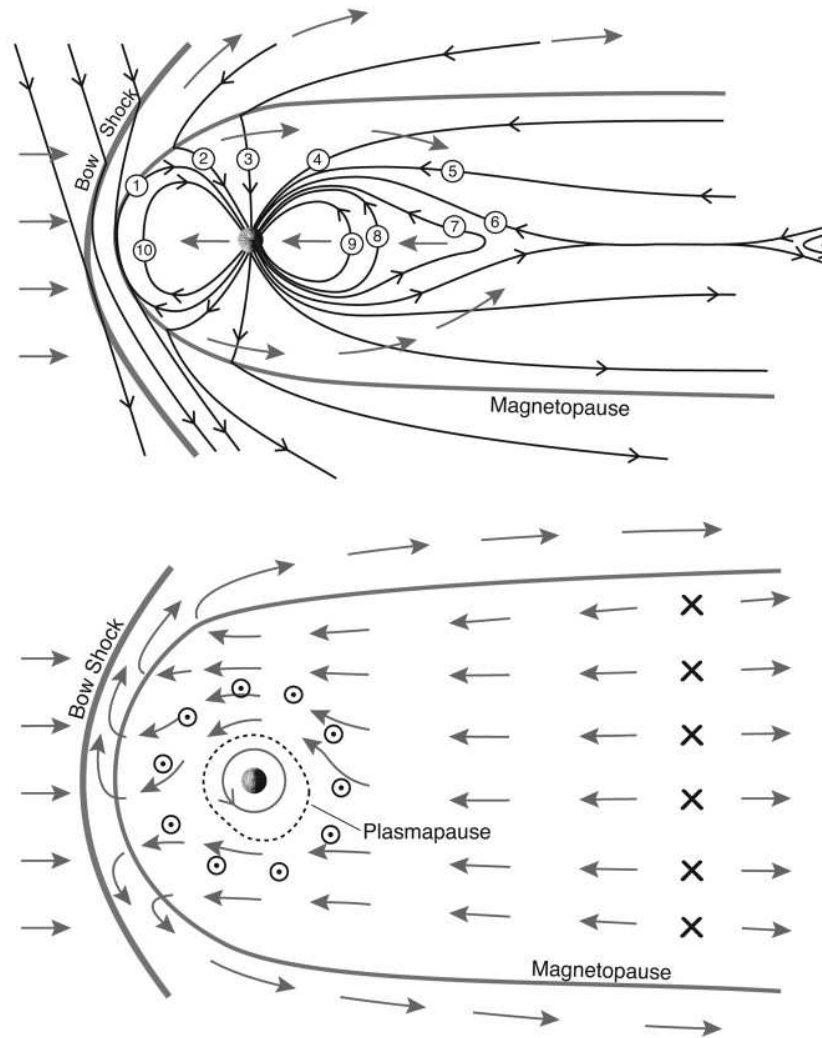
Fig. 13.4. Magnetospheric dynamics associated with the Dungey cycle driven by the solar wind. Top: view in the noon-midnight meridian plane. The numbers show the time sequence for a flux tube being reconnected at the dayside magnetopause and convected through the magnetosphere. Bottom: view in the equatorial plane. After Dungey (1961).
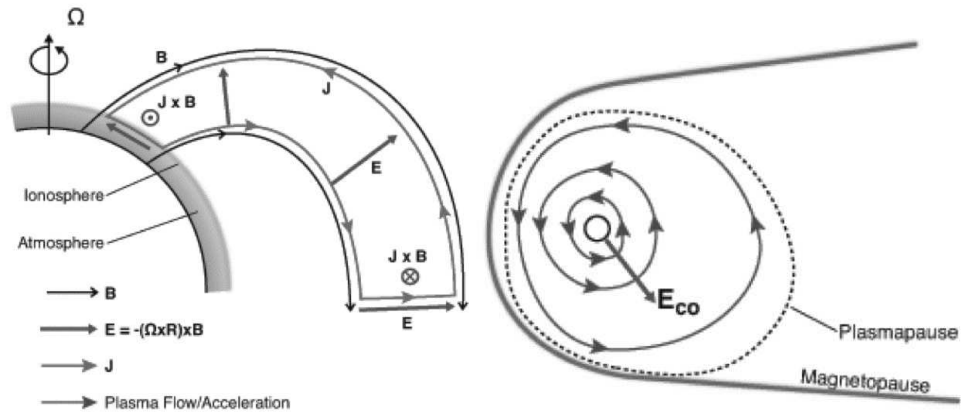
Fig. 13.5. Dynamics of a magnetosphere dominated by rotation viewed from the side (left) and in the equatorial plane (right). Compare with Fig. 10.6.
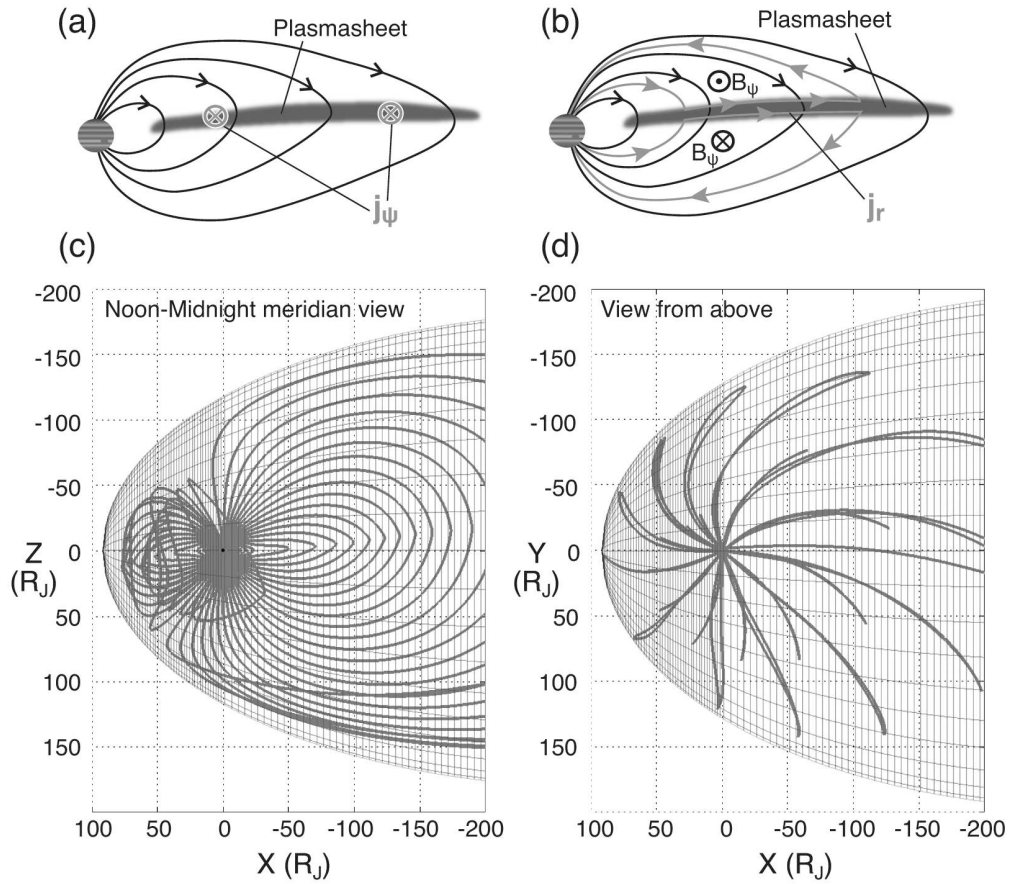
Fig. 13.6. Magnetic field configuration and current systems in Jupiter's magneto-sphere. The top diagrams show the (a) azimuthal and (b) radial current systems. The lower diagrams show the magnetic field configuration (c) in the noon-midnight meridian plane and (d) in the equatorial plane derived from in situ magnetic field measurements (**?**, **?**). Compare with the schematic representation in Fig. 10.6 discussed in Sect. 10.4.4.
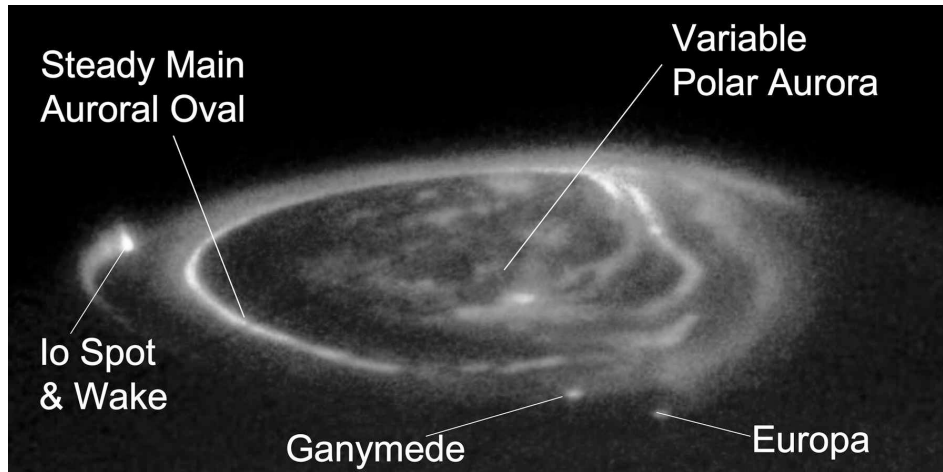
Fig. 13.7. The three main types of auroral emissions at Jupiter: the main aurora, satellite footprint emissions and polar aurora (Clarke, 2004).
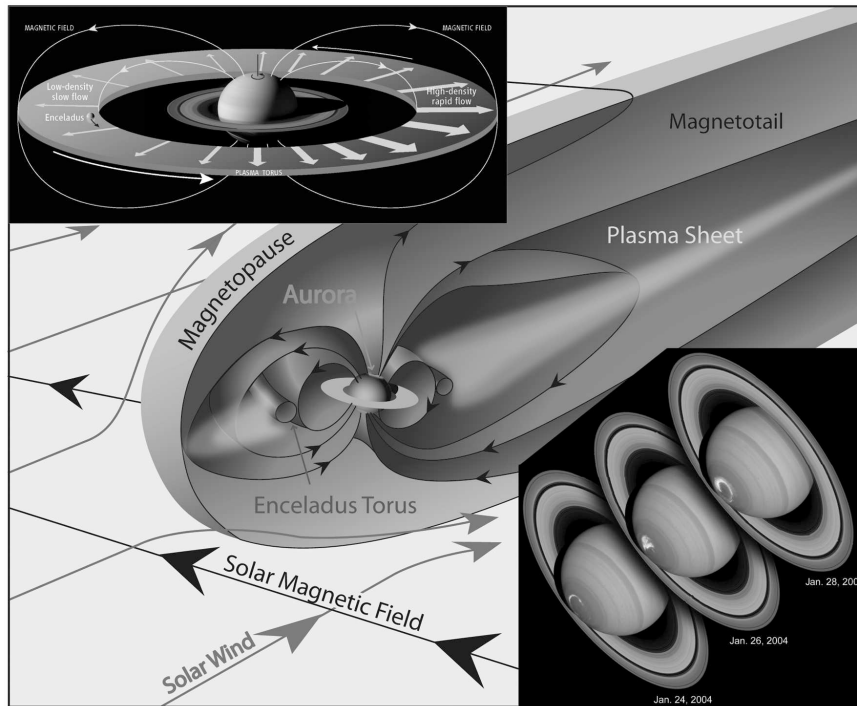
Fig. 13.8. Center: Three-dimensional schematic representation of the magneto-sphere of Saturn. Top left: Sketch of asymmetric plasma disk where Gurnett (2007) propose that the observed density variations are caused by a pattern of asymmetric radial outflows. Bottom right: Hubble Space Telescope observations of Saturn's auroral emissions (Clarke, 2005).
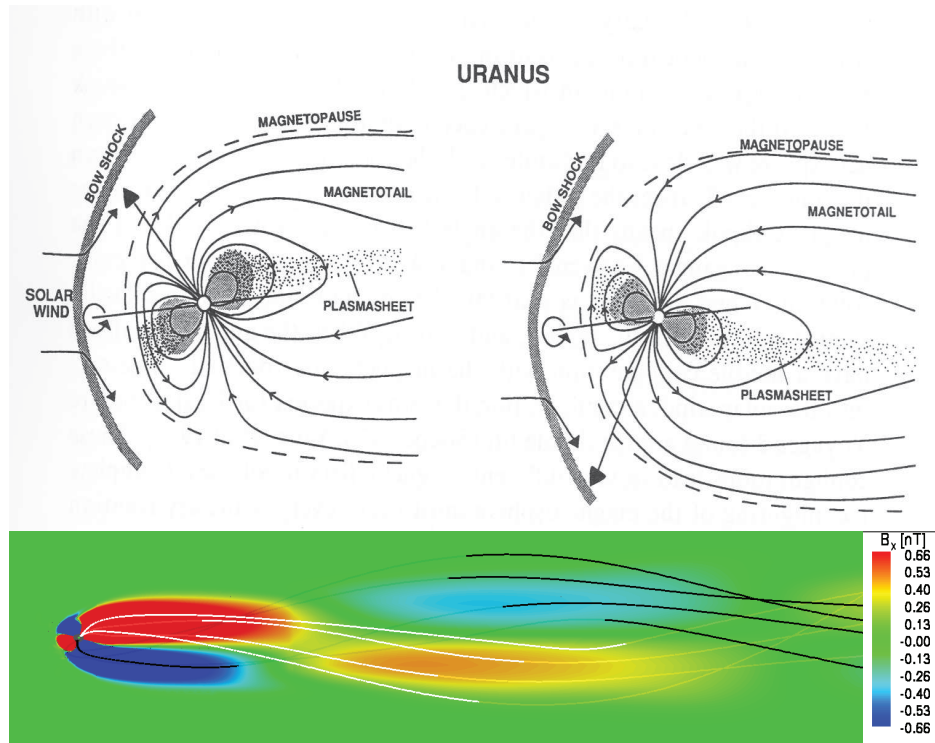
Fig. 13.9. The magnetosphere of Uranus at solstice (time of Voyager 2 flyby). The top left and right sketches show the configuration at different phases of the planet's 18-hour spin period (**?**, **?**). The bottom panel shows a numerical simulation of the helical magnetotail (**?**, **?**).
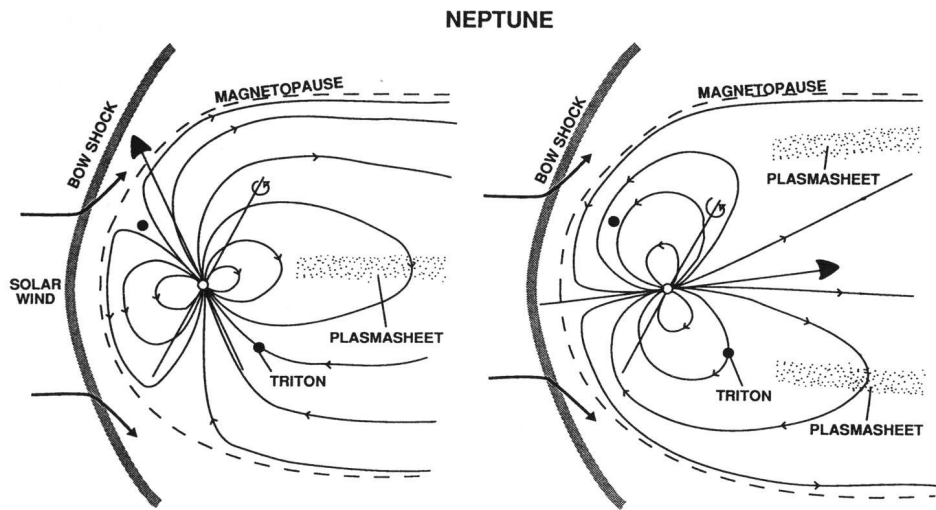
NEPTUNE

Fig. 13.10. The magnetosphere of Neptune in the configuration corresponding to the time of the Voyager 2 fly-by (**?**, **?**). Over the 19-hour spin period the magnetospheric plasma sheet in the tail changes from having a roughly planar to a cylindrical.
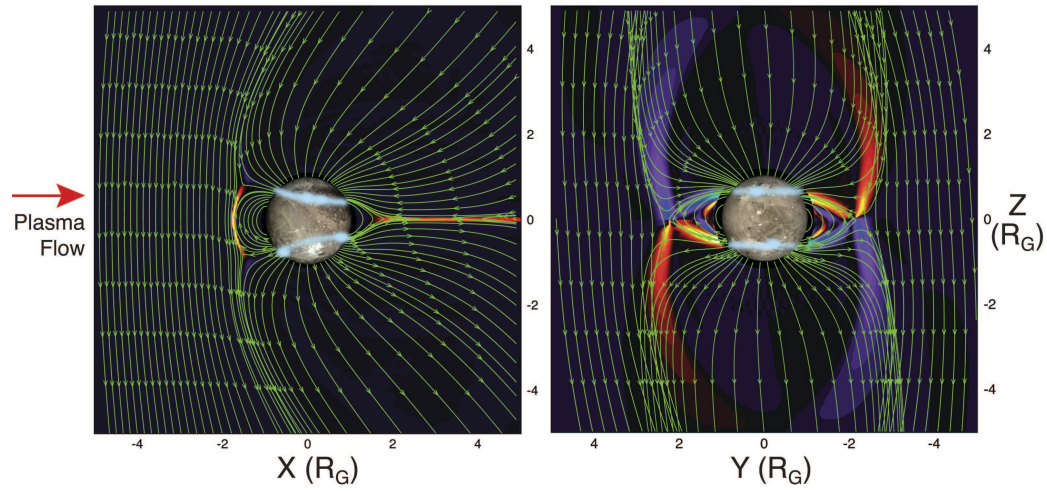
Fig. 13.11. Numerical model of the magnetosphere of Ganymede with the satellite and the location of auroral emissions superimposed (based on **?** (**?**)). Left: view looking at the anti-Jupiter side of Ganymede. Right: View looking in the direction of the plasma flow at the upstream side (orbital trailing side) of Ganymede with Jupiter to the left. The shaded areas show the regions of currents parallel to the magnetic field.
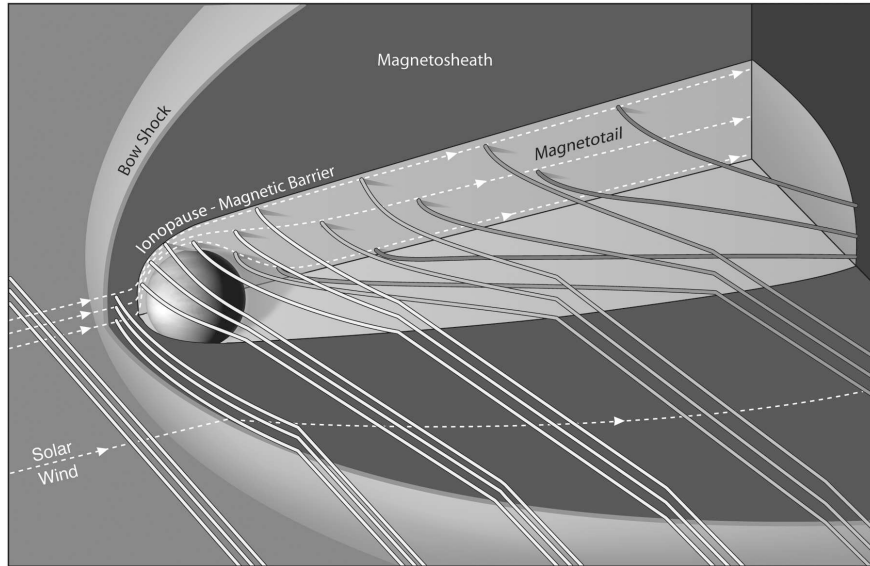
Fig. 13.12. Sketch of the draping of tubes of solar magnetic flux around a conduct-
ing ionosphere such as that of Venus. The flux tubes are slowed down and sink into
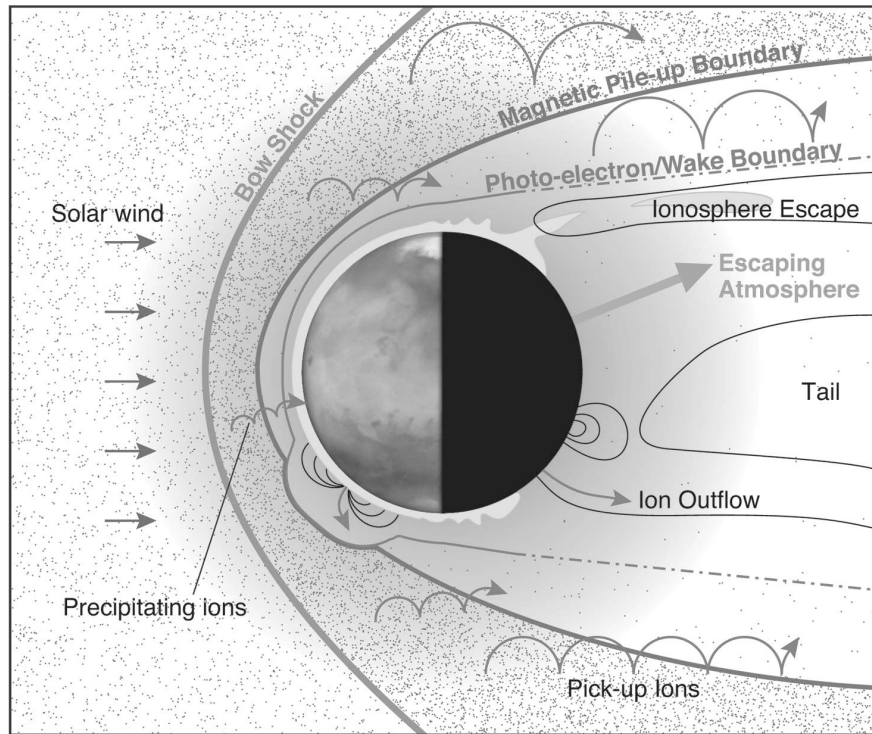the wake to form a tail (after **?** (**?**)).

Fig. 13.13. Interaction of the solar wind with the atmosphere, ionosphere and magnetized crust of Mars illustrating the several processes whereby the planet may have lost much of its atmosphere.
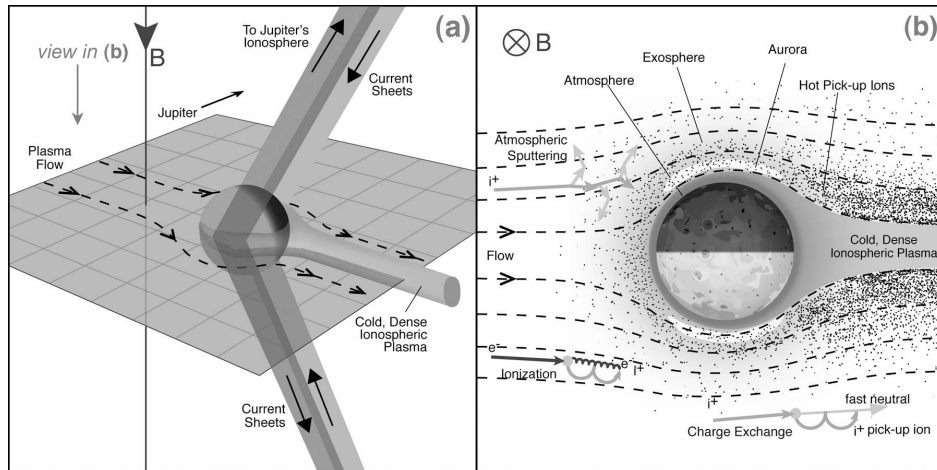
Fig. 13.14. Two views of the interaction between Io and the plasma torus. Panel (a) is a 3-D view showing the current sheets that couple Io and the surrounding plasma to Jupiter's ionosphere. Panel (b) is a cross-section of the interaction looking down on the north pole of Io, in the plane of Io's equator, when Io is located between the Sun and Jupiter (orbital phase 180°, local noon in magnetospheric coordinates).